Structure and Dynamics of Polymers in Melt, Solution, and Biological Membrane: Multiscale Simulation

Thesis Submitted to AcSIR For the Award of
the Degree of
DOCTOR OF PHILOSOPHY
In the
Chemical Sciences

ACADEMY OF SCIENTIFIC AND INNOVATIVE RESEARCH

By

Chandan Kumar Choudhury
Registration Number: 10CC11J26042

Under the guidance of

Dr. Sudip Roy

Dr. Guruswamy Kumaraswamy

CSIR-National Chemical Laboratory

July 2015

Certificate

This is to certify that the work incorporated in the Ph.D. thesis entitled **"Structure and Dynamics of Polymers in Melt, Solution, and Biological Membrane: Multi-scale Simulation"** submitted by Mr. Chandan Kumar Choudhury to Academy of Scientific and Innovative Research (AcSIR) in fulfillment of the requirements for the award of the Degree of **DOCTOR OF PHILOSOPHY**, embodies original research work under my guidance. We further certify that this work has not been submitted to any other University or Institutions on part or full for the award of any degree or diploma. Research material obtained from other sources has been duly acknowledged in the thesis. Any text, illustration, table, etc., used in the thesis from other sources, have been cited and acknowledged.

Signed:	Signed:	Signed:
Chandan Kumar Choudhury	Dr. Sudip Roy	Dr. Guruswamy Kumaraswamy
(Research Fellow)	(Research Supervisor)	(Research Co-Supervisor)
Date:	Date:	Date:

Physical and Materials Chemistry Division Polymer Science and Engineering Division

CSIR-National Chemical Laboratory

Pune-411008.

". . . everything that is living can be understood in terms of the jiggling and wiggling of atoms."

Richard Feynman

ACADEMY OF SCIENTIFIC AND INNOVATIVE RESEARCH

Abstract

Chemical Sciences
CSIR-National Chemical Laboratory

Doctor of Philosophy

by Chandan Kumar Choudhury

This thesis presents an account of the theoretical research on a small domain of soft materials. The interaction of various soft matter e.g., surfactants, lipid bilayers with polymer are exploited. The polymers in its melt state are also explored. Overall, this thesis demonstrates the structural and dynamical properties of polymer–surfactant, polymer–lipid membrane, polymer solvation and polymer in melt systems using molecular simulations. The investigations were carried on the atomic and coarse-grained level. All atomic molecular dynamics simulations were perform to investigate the polymer–surfactant, polymer–lipid membrane and polymer solvation interactions, while the polymer melts were studied using the coarse-grained (CG) molecular dynamics simulations.

In the first three of the working chapters, we have explored solvation dynamics of Polyethylenimine (PEI) and its interactions with surfactants and lipid bilayers. PEI is known to be an potent non-viral gene delivery vector. It complexes with DNA to form polyplexes. This polyplexes are then transported inside the cell by the process called endocytosis. The low pH in the endosomes expands the polymer matrix which frees the genetic content to make its way to the cell nucleus. In this thesis, we have exploited the effect of pH on the PEI–surfactant, PEI–lipid membrane and PEI solvation interactions. The protonation state of PEI – unprotonated PEI (high pH) and protonated PEI (low pH) reflects the pH. At high pH, PEI stabilizes in a coiled conformation, with non-ionic surfactants it aggregates and when embedded in the lipid bilayer it settles at the lipid-water interface. While at low pH, PEI expands resulting an elongated conformation and its forms a small hydrophilic pore in the lipid bilayer which facilitates the transport of water and ions. This disruption of bilayer may also account for the toxicity associated with PEI.

In the penultimate and the last working chapters, we have explored how we can coarse-grain polymer melt and study its properties using the information from the smaller length scales. In addition, the importance of inclusion of torsion potential and the extend of

scalability of CG potentials are highlighted on Polycarbonate melts. We underlined that for polycarbonates the CG potentials developed from 5-mer chain length can be used to obtain the properties (in consistent with the polymer scaling law) of the larger molecular weights.

Acknowledgements

I owe my gratitude to all those people who have made this thesis possible. I express my deepest gratitude to my advisors – Dr. Sudip Roy and Dr. Guruswamy Kumaraswamy for excellent guidance, caring, patience, and providing the room to work in my own way. Their patience and support helped me overcome many crisis situations and finish this thesis. I am also thankful to Sudip for encouraging the use of correct grammar and consistent notation in my writings and for carefully reading and commenting on countless revisions of manuscripts. He also provided insightful comments and constructive criticisms at different stages of my research which were thought-provoking and they helped me to focus on my ideas. I am thankful to Guru for providing be an experience to interact with experimentalists and offering me financial support towards the end of Ph. D. One simply can not wish for a better or friendlier supervisors.

I am deeply grateful to Dr. Paola Carbone, Senior Lecturer, School of Chemical Engineering and Analytical Science, The University of Manchester for providing me an opportunity to work in her group. I am thankful to her encouragement and advices.

I thank members of my doctoral advisory committee Dr. Viruthiamparambath Ravikumar, Dr. Sarika Maitra Bhattacharyya (CSIR-NCL, Pune), and Dr. Prasenjit Ghosh (Indian Institute of Science Education and Research, Pune) for their constructive comments during the process of evaluation. It helped me develop approach towards presenting and defending my research work.

I am greatly benefited from the classes by Dr. Bhattacharyya and Dr. Pal. I also thank Dr. Rajnish Kumar (CSIR-NCL, Pune) for discussions. I also thank Dr. B. L. V. Prasad for his patience in communicating with AcSIR and obtaining the thesis submission approval.

I am thankful in receiving generous support from our High Performance Computing and Network Administrator team – Mr. K. D. Deshpande, Mr. Avinash Deotale, Mr. Javed, and Mr. Sanjay Aksar.

I am also grateful to Dr. Kamendra Sharma, and Mr. Manoj Kumar for discussions on experiments and its connection with computational investigations. Thanks are due to my colleagues Dr. Prithvi Raj Pandey, Mr. Souvik Chakraborty, Mr. Anil Ranu Mhashal, Mr. Subhadip Das, and Mr. Sujit Sarkar for useful sessions of discussions. Their advice, comments and criticism helped me to evolve my scientific understandings and improve my knowledge in the area. I thank Mr. Abhinaw, Mr. Santu Biswas, Mr. Nilesh Choudhary, Mr. Bappa Ghosh, and Ms. Pragati Sharma for their encouragement. I appreciate the feedback offered from Dr. Sheelan Sengupta in preparing this thesis. A special thanks

to Ms. Swagata Pahari for many scientific and non-scientific discussions and providing constructive comments and warm encouragement.

I gratefully acknowledge UGC and CSIR-NCL for providing the fellowship and infrastructure to carry the computational investigations.

I have greatly benefited from the sessions on Badminton at CSIR-NCL community center and heartfeltly appreciate the efforts by Mr. Suman Chandra and Mr. Anil Ranu Mhashal. Friends at Scientist Apartments – Mr. Shashi Kant Shukla, Dr. Raja Das, and Mr. Manjunath B. Udinur helped to overcome the setbacks, stay focused, and creating lively environment. I greatly value their friendship and I deeply appreciate their belief in me. I also thank Dr. Tanay Kundu, Dr. Subhadeep Saha, and Dr. Arijit Mallick for providing unconditional help in putting together official documents relating to the thesis submission and making it a flawless process.

I also appreciate Dr. Sunil Patel's (http://www.sunilpatel.co.uk/thesis) effort in publishing the backbone of this thesis template in open source fraternity. Thesis writing with the template was enjoyable. I also acknowledges the help obtained from www.google.com on countless occasions and helping to evolve my understanding throughout my Ph. D. career.

Last but not the least, I would like to thank my family: my parents Jagarnath Choudhury and Sulekha Devi, my brothers Nandan and Kundan and my sister Bandana for believing in me.

Contents

[1] This chapter is adapted from the publication C. K. Choudhury and S. Roy, Structural and dynamical properties of Polyethylenimine in explicit water at different protonation states: a Molecular Dynamics Study, Soft Matter, 2013, 9 (7), 2269 – 2281.

[2] Part of the chapter (the structural and pair distributions) were adapted from the publication K. P. Sharma, C. K. Choudhury, S. Srivastava, H. Davis, P. R. Rajamohanan, S. Roy and G. Kumaraswamy, Assembly of Polyethyleneimine in the Hexagonal Mesophase of Nonionic Surfactant: Effect of pH and Temperature , J. Phys. Chem. B 2011, 115, 9059–9069.

[3]This chapter is adapted from the publication C. K. Choudhury, A. Kumar and S. Roy, Characterization of Conformation and Interaction of Gene Delivery Vector Polyethylenimine with Phospholipid Bilayer at Different Protonation State, Biomacromolecules, 2013, 14 (10), 3759 – 3768.

List of Figures

List of Tables

Symbols

C_N	characteristic ratio
$C(t)$	correlation function at time t
D	diffusion coefficient
E	total energy
E_a	activation energy
F	free energy
$\boldsymbol{F}_i$	force on particle i
G	Gibbs free energy
k_B	Boltzmann's constant
k	force constant
K	kinetic energy
m_i	mass of particle i
M	molecular weight
N	number of particles
N_f	degrees of freedom
P	linear momentum
$\mathcal{P}$	instantaneous or microscopic pressure
P	macroscopic pressure
$P(q)$	Boltzmann distribution
$\boldsymbol{r}_i$	position vector of particle i
r	bond length
R	hydrodynamic radius
R	end-to-end distance
R_g	radius of gyration
S	entropy

T	temperature
$T(t)$	instantaneous temperature
T_g	glass transition temperature
T_m	melting temperature
t	time
δt	Molecular Dynamics time step
U	internal energy
$V(r)$	pair potential
V	volume
$\boldsymbol{v}$	velocity
Z	partition function
β	$\frac{1}{k_B T}$
γ	surface tension
η	viscosity
θ	angle
κ	isothermal compressibility
λ	velocity scaling factor
ν	polymer scaling coefficient
ρ	density
$\sigma^2_{\mathcal{A}}$	variance in dynamical variable $\mathcal{A}$
τ	temperature coupling parameter
τ_s	slow relaxation time
τ_f	fast relaxation time
ϕ	torsional angle
Ω	states available to the system
$\langle \cdots \rangle$	ensemble average
$\mathcal{O}(x^n)$	terms of order x^n or smaller

Dedicated to my parents...

Chapter 1

Introduction

Soft matter is ubiquitous! It includes polymers, emulsions, surfactants, liquid crystals, gels, biological systems etc. All living organisms are soft matter. They are used in many aspects of our daily necessities and modern technologies (viz., in displays, biomedical applications, device manufacturing). Soft matter often self-assembles into microscopic structures which determines the macroscopic properties of the materials. It is vital to understand such structures and the interactions and forces prompting such assemblies. These assemblies are driven by the various conformations of soft matter. The understanding of structural arrangement of the self-assembling constituents are, thus, very important. Furthermore, the dynamics of the soft matter particles are also interesting which can provide a clear picture and mechanism of the self-assembly. In light to these structural and dynamical properties, we have used molecular simulation techniques (both at the atomistic and microscopic level) to investigate the microscopic level interactions polymer in different soft matter systems.

Polymers are macromolecular substance with repeating subunits. In this thesis, we describe the behavior of polymers in melt and its interaction with lipid membranes. We also investigate the solvation behavior of polymer in water. We used polycarbonate to study the polymer melt and polyethylenimine to explore the other interactions. Since these materials belongs to soft matter, in this chapter, we introduce the soft matter *in general* and provide some thermodynamics basis of it. We then describe the solvation dynamics of polymer and its interaction with surfactants and lipid bilayer membranes. And finally outline the motivation for our work, and the objectives of this thesis.

1.1 Soft matter

Soft matters are structured fluids i.e., condensed matter in which the atoms are adjacent but freely mobile on a local scale. [1] They can be squeezed, sheared, and deformed with small amount of energy because their conformations are determined by the weak forces like van der Waals' and hydrogen bondings. The order of this energy is close to the thermal energy k_BT which is available to the system at temperature T and thus fluctuations in the temperature can lead to conformational change. Thermal energy decides the partitioning of molecules among different energy levels of a system. The magnitude of k_BT often indicates the strength of interaction. The origin of this intermolecular interaction can be explained in terms of van der Waals attraction resulting from the dipole-dipole interactions. If the interaction energy is greater than k_BT, it suppresses the opposing, disorganizing, and randomizing effect of thermal motion. [2] The delicate balance between the two (attractive interaction and the disordering effects of the thermal motion), dictates the structure of a system at a particular temperature. At high temperature, thermal motion prevents particles from condensing into a regular structure, while at low temperature, thermal motions are not large enough to overcome the attractive interactions and thus leading the particles to condense. [3] Thus, the properties of the soft matter systems are entropic in nature. [4] Soft materials fall in-between solid and liquidic state. In liquid state molecules are free to move and they occupy new positions depending upon the previous position. While in solids, the molecules are fixed in a position. Soft condensed matter (or soft matter) is a fluid where large groups of the elementary molecules are constrained so that the freedom of movement of these groups are restricted. For example, many small molecules may be fastened together to form a rigid rod or flexible chain. The new fastened-together groups which are significant in number gives rise to a new behavior to soft matter. This new behavior becomes apparent because the constrained large groups are composed of various small molecules, which has fluid like motion dominated by thermal fluctuations. [5] A classic example is a protein molecule where the constituent amino acids possess larger degrees of freedom, while the proteins itself (considering the whole molecule or domains) have limited motion.

In these types of matter, the structural ordering is intermediate between crystalline solids and liquids. This lack of crystalline order contributes to the "soft" character of the materials. [6] Soft matters are often viscoelastic which distinguishes it from conventional liquids. The typical soft materials are polymers, membranes, liquid crystals, colloids, biological systems, and surfactants. All these materials are industrially of great importance. The length scale of ordering of these materials are in the range of 1-1000 nm, which corresponds to nanoscale or mesoscopic ordering. This length scale is intermediate between microscopic (atomic) and macroscopic scales. [6] For example,

colloidal particles and polymers are typically less than a micrometer in size, liquid crystals and self-assembled amphiphilic molecules are of the order of tens of nanometers while biomolecules are nanometers in size.

Soft matter is characterized by complexities not only in structural arrangements but also in dynamical properties. They undergo Brownian motion, which leads to the random zig-zag motions described as random walk. [6] Though the typical sizes of the structures in soft matter are larger than atomic sizes, they are small enough for Brownian motion. [1] The energies associated with these structures and with the distortion of these structures are comparable in size to thermal energies. The diffusion of these particles (structures) in solution can be estimated by the Stokes-Einstein equation,

$$D \;=\; \frac{k_B\, T}{6\pi\eta R}$$

where D is the diffusion coefficient, η is the viscosity of the medium, R is the effective radius of the particle or molecule (hydrodynamic radius) and $k_B\, T$ is an estimate of the translational kinetic energy per particle. Typical diffusion coefficients for molecules in liquids (and thermotropic liquid crystal) are of the order of 10^{-9} m^2 s^{-1}, for polymers because of larger hydrodynamic radius, it can be as low as 10^{-18} m^2 s^{-1}. While micelles diffusing in water at room temperature with hydrodynamic radius ≈ 10 nm have $D \approx\; 2 \times 10^{-11}$ m^2 s^{-1}. [6]

Another intriguing feature of soft matters are to self-assemble in mesoscopic and macroscopic structure. The origin of these organized assemblies can be understood in terms of hydrophobic interactions. These interactions are also responsible of low solubility of hydrocarbons in water and eventually they arrange themselves and forms highly ordered supramolecular assemblies, even though the constituent units are non-crystalline with dimensions larger than the atomic scale. [7] One of the common example of such assemblies is the formation of miceller arrangement by the mixing of oil and water. [8] Thermodynamically, self-assembly is driven by the molecular ordering resulting from the balance of the entropic and intermolecular forces in a material. The interplay between the attractive and repulsive force drives the self-assembly of various soft materials. In a self-assembly process, when the system reaches equilibrium, its free energy is minimized. Free energy, F, is the maximum amount of energy available in the system that can be converted to work.

$$F \;=\; U -\; TS$$

$$S \;=\; k_B \ln \Omega$$

Entropy, S, is a macroscopic variable that represents the disorder of the system. Ω is the total number of states (configurations) accessible to the system. This is the measure of

the 'disorder' in that system. The larger the disorder, the larger the entropy. Thus it follows that a system will evolve till its entropy is maximized.

Entropy is also related to the temperature of the system. An increase in the temperature, increases the thermal motion, and the entropy of the system. Internal energy, U, is the energy stored in the interatomic bonds and molecular motions. TS refers to the energy given to the system by the environment. At constant volume, temperature, and number of particles, the change in entropy is related to the change in free energy as:

$$dS = -\frac{1}{T}dF$$

Therefore, an increase in the entropy corresponds to the decrease in the free energy, and thus when entropy is maximized, free energy is minimized. Entropy is indeed a intriguing quantity because without it the self-assembly does not occur and its large number of accessible states (configurations) prohibit its analytical prediction. The entropy of soft materials are high because the interactions between the building blocks are weak and isotropic (mainly van der Waals interactions).

In chemistry, the Gibbs free energy G is generally used instead of Helmholtz free energy F.

$$G = H - TS = U + PV - TS$$

where P is the absolute pressure, and V is the system volume. Gibbs free energy is equivalent to the Helmholtz free energy F with an addition term of PV which takes into account the volume changes on the system. Thus the available free energy of the system is composed of the internal energy of the atoms or bonds (or potential energy associated with the molecular interactions) and the work done on the environment to place the system there (these two equals enthalpy H) minus an energy term that represents the effect of thermal motion on the system. The particles at room temperature posseses Brownian motion fluctuating constantly and moving. They also attract each other. The competition between them (attraction and thermal motion) drives the self-assembly of an enormous range of soft matters, few of them are discussed in this thesis. Depending upon the chemical structure of the molecule as well as solution properties such as ionic strength, temperature, and composition in mixed systems, they may self-assemble to form different structures with respect to size, shape, flexibility, polydispersity etc. Thus, soft matter is pervasive. In the next section, we present the classification of soft matters.[1]

[1] These classification are by no means distinct and many soft matter can be fitting in more than one class.

1.2 Examples of soft matter

1.2.1 Polymer

Polymers – an essential entity of our lives, are long chained macromolecules. They have been replacing our natural materials and traditional technologies in many daily applications. Traditional glues, fabrics, paints, wooden chairs are replaced with polymers. It is difficult to classify them in any of the three states of matter – solid, liquid or gas. They do not exist in the gas phase, are viscous in liquid state (even in solution) and in solid state, they never completely crystallize. [9] Crystallization in polymers is accompanied by 'straightening' of the polymer chains. All the polymer chains having stretched conformation is entropically too expensive, thus few chains remains in coiled conformation, giving rise to amorphocity. Thus, it is difficult to classify the phase behavior of polymers in the usual states of matter. Solid polymers are either glassy (amorphous) or semicrystalline. When they melt, chains interpenetrate and entangle strongly. Every chain interacts with thousand other chains. These chains possess relatively low energy barrier to the rotation about the single bond. This energy can be easily gained from the thermal energy which gives rise to the different conformations of the polymer chains. The shapes and the conformations of polymer chains have a direct impact upon their physical properties. The rigid rod polymers generally have more stretched (or extended) conformations than the polymers with flexible backbone. Rigid rod polymers are generally stiffer and has a higher glass transition temperature. Polymer chains have viscoelastic behavior in the melt state, both viscous and elastic flow, depending upon the time scale of observation. The solution behavior of polymers is fascinating and it depends upon the nature of the solvent either good or bad for the particular polymer. Solvation behavior is also dependent upon the polymer concentration and the temperature of operation.

1.2.2 Colloids

Colloids are heterogenous suspensions of solid particles in a fluid. Inks, paints, clays, smoke falls in the category of colloids. The particle size ranges form nanometer to microns. The colloidal particles are small enough to exhibit thermal motions and dominate the gravitational energy and large enough to approach its bulk properties in the atomic length and time scales. [10] Colloidal particles in a dispersion undergo Brownian motion. When they encounter one another, the attractive and repulsive interaction between the particles decides the stability of colloids. If these interaction balance each other, the stable suspension is formed. If the attractive interaction (at the shorter distance) dominates

the overall interaction, then an instability is caused which leads to the aggregation of colloidal particles. [11]

1.2.3 Amphiphiles

Amphiphiles are molecules which has two sides to their behavior. One part likes the solvent (i.e., soluble in it) and the other part does not. The insoluble part has favorable free energy when they are away from the solvent, and thus tend to concentrate at the solvent boundary. As they influence the properties of surfaces and other boundaries, these molecules are called 'surfactants'. In aqueous solution or in oil-water mixture, these molecule aggregates such that the tails (hydrophobic) are away from the aqueous medium. Beyond its solubility limit and at a certain concentration, called critical micelle concentration, the surfactants self-assembles into micelles. This tendency of the hydrophobic region to avoid contact with water is termed as 'hydrophobic effect'. This 'hydrophobic effect' leads to the formation of micelle which are entropically driven. Thermodynamically, the change in free energy of micellization is given as

$$\Delta G_{mic} = \Delta H_{mic} - T\Delta S_{mic},$$

thus the hydrophobic effect is also affected by the enthalpy contribution (ΔH_{mic}) along with its entropy term (ΔS_{mic}). And each term is a function of temperature and pressure. A negative value of ΔG_{mic} means that the formation of micelles is spontaneous. ΔH_{mic} can be either negative or positive, which means that micellization can be either favorable or unfavorable enthalpy-wise. But, the ΔS_{mic} usually shows a positive value at the temperature range of $\sim$ 10 to $\sim$ 40°C, which means the micellization is entropically favorable at this condition. [12] For a positive ΔH_{mic} value, the entropy contribution to micellization is always greater than the contribution from enthalpy: $\Delta H_{mic} < T\Delta S_{mic}$. This entropy-dominant contribution to micellization is called the hydrophobic effect for micellization. The entropy contribution to process of micellization comes from the following sources:

1. The organization of tails groups ($\Delta S_{surfactant}$).
2. The nature of water molecules around the tail moieties (ΔS_{water}).
3. The molecular arrangement of the head groups (ΔS_{head}).

Thus,

$$\Delta S_{mic} = \Delta S_{surfactant} + \Delta S_{water} + \Delta S_{hydrocarbon}.$$

The magnitude of ΔS_{head} is typically smaller and can be neglected. This yields

$$\Delta S_{mic} \cong \Delta S_{surfactant} + \Delta S_{water}.$$

During micellization hundreds and thousands of surfactant molecules comes close to one another such that a hydrophobic inner core is formed which is shielded from water by the surrounding corona formed from the hydrophilic ends of the molecules. This tends to decrease the entropy of the surfactant molecules, i.e., $\Delta S_{surfactant}$ is always negative. However, when the surfactant molecules comes in contact with the water the tetrahedral bonding sites of water molecules are disrupted around the surfactant (solute)–water interface or at the surface of solute. The most favorable way to re-organize energetically for water molecules is giving up one bonding site and forming a network of water molecules around the solute molecules. This is called *iceberg cluster* or *iceberg formation*. [13, 14] The water molecules in the proximity of hydrocarbon tails form entropically unfavorable ordered structures. [15] Water molecules in the immediate vicinity of the tails are believed to be oriented such that they hydrogen bond with each other and not the methylenes in the tails. [16] These water molecules are assumed to be more ordered than nearby water molecules in the bulk aqueous pseudophase. [16] The iceberg formation itself is not an entropic effect. The molecular motion (both translational and reorientational motions) of the water molecules at this iceberg structure is measured at $\sim 10^{-3}$ times slower than those in bulk water. [17] This is actually a loss of entropy of the system, and it is compensated and overcome by the enthalpy term. When the solute molecules with water clusters come close together, this iceberg structure starts to break into individual water molecules. As they go back into the bulk water, they regain their original molecular motion. Now, the solute molecules that come close together obviously lose their entropy, but the overall system gains a significant amount of entropy that overcomes the entropy loss from the aggregation of solute molecules. This is why hydrophobic substances often show an unusually stronger interaction in water than in a gas state, that is, mainly van der Waals interaction. Thus as the the release of structured water around the hydrocarbon chains (iceberg structure) during micellization is an increase of the entropy, which always is positive, $\Delta S_{water} > 0$. [12] This leads to the association of molecules into micelles. Lipids assemble in water to form membranes (monolayer or bilayer). These amphiphilic molecules in biological systems are ordered and also fluidic to allow the transport small molecules (ions, water) across them.

For most of the typical surfactants, $|\Delta S_{surfactant}| < |\Delta S_{water}|$ is fulfilled usually at the temperature range of $\sim$ 10 to $\sim$ 40°C. So, ΔS_{mic} is always > 0, and as stated above, its contribution is always dominant over the enthalpy contribution. But, as the temperature is increased, $|\Delta S_{surfactant}| > |\Delta S_{water}|$, thus $\Delta S_{mic} < 0$ often becomes the

reality, possibly because of the lack of enough structured water. This is the situation where micellization becomes entropically unfavorable. The micellization can occur only when the enthalpy contribution in the system is enough to overcome this negative entropy contribution. [12]

1.2.4 Liquid crystal

Liquid crystal is a phase intermediate between solid and liquid. The ordering is in-between that of the regular structure of a crystal and the molecular disorder of a liquid. This phase is also described as mesophase and the molecules capable of forming such phase are called mesogens. They do not exhibit any positional order but they do possess a certain degree of orientational and/or translational order because of the formation of mesophase. This gives rise to the anisotropicity which led to the formation of rod-like or plate-like shapes of the mesogenic particles. Liquid crystal phases formed by pure mesogens at a particular temperature are termed as thermotropic liquid crystals. While those forming in solution, where concentration of the mesogens controls the liquid crystallinity are referred as lyotropic liquid crystals. Lyotropic liquid crystals are formed by amphiphiles in solution. The molecular organization of the mesogen dictates the phase behavior of the mesophase. The long range order of the mesogenic molecules in certain direction called director within the mesophase, gives rise to the nematic phase. In addition to the orientational order, if the positional order are also present the phase formed is called sematic phase. In this phase, molecules arrange to form sheets or layered structure. Both the thermotropic and lyotropic liquid crystals may exhibit nematic and sematic phases.

1.2.5 Biological materials

Biological materials are rather complex which comprises the self-assembly of proteins, lipids, nucleic acids or polysaccharides. They perform specific biological function they are destined to. Biological materials are very sensitive to weak stimuli like change in temperature, pH, exposure to radiation, or addition of solvents. They sometime gets denatured in response to these stimuli. Their intermolecular interaction energy is small compared to the thermal energy. [18] Thus this gives the fragile characteristic to biomaterials. These materials are mainly composed of 'living soft matter' – globular proteins are colloids, DNA is a stiff polymer, and the lipids forming cell membranes are essentially surfactants. The aggregation of proteins is of fundamental relevance to a number of daily phenomena, such blood coagulation, medical diseases, or cooking an egg in the kitchen. The aggregation and self-assembly of proteins in foods have important implications in our daily life.

1.2.6 Lipid membrane

The lipid bilayer is a universal component of all cell membranes. It is a thin polar membrane made of two layers of lipid molecules. These membranes are flat sheets that form a continuous barrier around all cells. Its role is critical because its structural components provide the barrier that marks the boundaries of a cell. The structure is called a "lipid bilayer" because it is composed of two layers of fat cells organized in two sheets. The lipid bilayer is typically about five nanometers thick and surrounds all cells providing the cell membrane structure. The phospholipids organize themselves in a bilayer to hide their hydrophobic tail regions and expose the hydrophilic regions to water. This organization is spontaneous, meaning it is a natural process and does not require energy. This structure forms the layer that is the wall between the inside and outside of the cell.

1.3 Motivation and objective of the present thesis

Polymers are everywhere and they play an important role in our day-to-day work. Polymer has supersede almost every materials. Think of a material, we will find a polymer as its substitute! A polymer is nomenclatured after the constituent monomer units. Polyethylene is made up of ethylene monomer, polystyrene is composed of styrene units, polyisoprene is a polymerization of isoprene units, ethylenimine units are polymerized to form polyethylenimine (PEI) and so on. Apart from the synthetic polymer, natural polymers also exist. Silk, wool, deoxyribonuclease acid (DNA), and proteins are naturally occurring polymers. The polymer serves our daily need because of its useful properties. Some polymers are hard, some are flexible and some are elastic. Some changes their properties with temperature, some gets hardened when cooled. Some possess low density, while some are dense. These properties are mostly governed by the arrangement of polymer chains. The arrangement and chain conformations also play a crucial role in dictating the polymer properties. High density polyethylenes are dominated by linear chains, while low density polyethylene is highly branched. A single flexible polymer chain can adopt different conformations. The nature of conformation depends upon the flexibility of polymer chains, interaction with-in the chains (intra-chain interaction), and external conditions like interactions with the surrounding chains (inter-chain interaction), and solvent at different temperatures and pHs. [19] Polymer finds its applications in various fields. It is difficult to find as aspect of our lives that is not affected by polymers. Polymer has had a major impact on the way we live. Every now and then new applications are being researched, and there is hardly any reason to

believe that this revolution will stop any time soon. This thesis presents some of the investigations on the applications of polymers, in particular PEI in gene delivery.

One of the applications where polymers are also used, is for the therapeutic purposes. Polyethylenimine (PEI) has recently gained attention on being uses for the therapeutic delivery. [20, 21] It is a polycationic polymer with high ionic charge density. It is also used for the gene delivery applications. [22] PEI exists both in linear and branched form. The secondary nitrogen forms linear chain while the branched chain consists of primary, secondary and tertiary nitrogen. It was first synthesised by alkaline hydrolysis of poly-N-formylethylenimine. [23] PEI has been reported as a versatile vector, both *in vivo* and *in vitro* for gene transfer into the cells. [24] Its transfection efficiency has been extensively studied, both *in vivo* and *in vitro*. [22, 24–30] It is also reported that the linear PEI is very efficient non-viral gene antifection agent when compared with the branched PEI. [22, 27] PEI is effective at neutral and higher pH to undergo complexation with DNA and at low pH it releases the DNA inside the cell. Therefore, structure of PEI and the competition between interactions of PEI with DNA and solvent molecules plays the crucial role in the mechanism to deliver DNA inside the cell. Linear chain PEI is an organic macromolecule with its alternate hydrophobic (-CH_2-CH_2- groups) and hydrophilic (NH- groups) units. Hydrophilic units are less in number but can effectively act as the proton acceptor in acidic conditions. However, due to the presence of hydrophobic units in between the hydrophilic units, polyelectrolyte character of PEI remains mild and can give rise to interesting properties. Thus, the effect of environment of PEI, in this case pH, plays a crucial role of the PEI-DNA interaction. Thus, in this thesis, we have explored the behavior of PEI in different protonation states (which represents the pH, lower pH protonates the amines of PEI, while at high pH the amines are unprotonated) in dilute aqueous solution. We have studied the conformation changes in PEI as a result of the change in pH (chapter 3). We have also studied the interaction of PEI (at different protonation states) with surfactants (chapter 4) and lipid membranes (chapter 5). The interaction of PEI with the non-ionic surfactant were also explored and how PEI disrupts the formation of hexagonal mesophase at high pH was also investigated.

In addition to the study of single polymer chain, we have also investigated the structural and dynamical properties of polymer melts (chapters 6 and 7). The polymer melts in their amorphous state have wide range of time scales for conformational relaxation. [31] Such times are difficult to be accessed by the present day supercomputers using the all atomistic MD. Thus, we employed coarse-grained (CG) strategies where the degrees of freedom were reduced by treating polymer chains in form of beads. These beads comprises a group of atoms which are bonded by the bead-bead potential derived from the atomistic trajectories. The polymer equilibration and its relaxation can be achieved by using the CG methods. In the structure based CG methods, bead-bead inter and

intra potentials are developed from the atomistic trajectories. Does these CG potentials are able to *scale* the structural properties as a function of chain length or molecular weight? How are the dynamical properties affected? These inquisitive questions propelled us to investigate the polymer melts of different molecular weights ranging from 3-mer to 100-mer with the CG potentials derived from the oligomers. In this thesis, we have explored the possibilities of scaling the length scale of polymer melt using the bead-bead potentials derived from the oligomers (say of melt of chain length of 3-mer or 5-mer).

1.3.1 Polymer solvation

Solvation is a process where solute molecule interacts with the solvent leading to its stabilization. Solvent molecules diffuse into the porous structure of the polymer when it is exposed to the solvent. If the polymer is soluble in solvent, there is an attractive interaction between them while for the polymer segments the net interactions are repulsive. So, at this stage if the polymer is coiled it starts swelling and attains an equilibrium structure. [32] When polymer interacts with the solvent, thermodynamically, it produces a structural state. Statistically, there are many interaction configurations in the solvation shell. [33] Each of these configurations is solvation structure. Upon solvation, there is a change in the overall size of the polymer chain. Thus, understanding the polymer chain dynamics, its equilibrium structure in the presence of solvent and the solvation structure are important. Also, the polymer conformations are governed by the nature of solvent – either good, or bad, or theta solvent. At theta solvent condition the polymer at dilute conditions behaves as ideal chains. At this point, the repulsive forces due to excluded volume are exactly balanced by the compressive forces exerted by the surface tension of the solvent. In a good solvent, the solvent interacts favorably with the polymer which expands the chain configurations. And in poor solvent, the polymer collapses. The importance of solvent for the biological systems are very critical. For example, the conformational stability of the human polyclonal IgG in solution decreases with decreasing pH. [34] These studies are also utmost importance for the biological functions as proteins are always nearly solvated in the physiological conditions. [35, 36] In fact the importance of solvent being treated explicitly for the protein folding studies also have been confirmed. [37, 38]

1.3.2 Polymer – surfactant interactions

Surfactant molecules (ionic, non-ionic, and zwitterionic) self-assembles to form spherical aggregates in dilute aqueous solutions. The hydrophobic core are formed by the surfactant tails and the head groups protrude towards the water. The formation of

self-assembled structure (or phases) of the surfactant molecules are dependent upon the relative concentration of water and/or oil, and surfactant. When the concentration of surfactant is above the critical micelle concentration, the spherical micelles are formed. Further increase in the surfactant concentration gives rise to infinite cylinder like phase which gets converted to hexagonal mesophase. The long cylindrical micelles get arranged in the hexagonal pattern with typical hydrophobic core. The spherical micelle sometimes self-assembles in the face-centered or body centered cubic lattice forming cubic phase. A lamellar phase is also formed where a layer of water is sandwiched between the layers of surfactant molecules. Also there are other phases like bicontinuous and inverted micelles.

Surfactants are widely used in cosmetics, pharmaceuticals products and in the food industry. Often, the polymers or surfactants are added into one another to fine tune the properties of either surfactant or polymer solution. For example, to impart high viscosity (a polymer property) to a surfactant solution polymers are mixed or to introduce the capacity to solubilize the hydrophobic molecules (a surfactant property) to a polymer solution surfactants are mixed. [39] The addition of a component also affects the phase behavior of the other. The presence of polymer and surfactant initiates an interaction between them, which contributes towards the change in the properties/phase behavior.

1.3.3 Polymer – lipid membrane interactions

Polycationic polymers, recently, are used to disrupt the cell membranes, which facilitate the transport of materials from the external environment to the cell. [40–45] These membranes act as selective barrier that regulates the flow or transport of materials from the external to the internal environment of the cell, thus protecting against foreign substances. [46] In addition to many vital functions of membranes, one of the most indispensable functions is its stability against external perturbations. In the past it has been shown that the membranes get ruptured by introducing external forces like stress similar to electroporation technique. [47–50] The membrane rupture occurs due to the formation of pores. It is assumed that initially short-lived small hydrophobic pores are formed and then lipid molecules reorient to form hydrophilic (head groups) pore walls. [49] Under mechanical stress, hydrophilic pores are formed in peptide free lipid bilayers. [48] It is also well known that the proteins and peptides can create channels and regulate the permeability of ions and protons through it. A number of studies has revealed that the cytolytic and antimicrobial agents and some polyelectrolyte oligomers are able to disrupt the lipid bilayers by forming stabilized pores. [51–56] The study of stabilized pores are biologically very important as it can assist the transport of polar molecules and ions across the membranes and it could also lead to the initiation of cell lysis or fusion. [57, 58] In addition to the small molecules, pores formed by the

electroporation technique can also facilitate DNA uptake by the cells. [59] Small pores formed by antimicrobial peptides destroy transmembrane ion gradients and electrical potential which can lead to cell death. [54] Most of these peptides are either cationic or amphipathic.

1.3.4 Polymer in melt

Polymer melts are bulk polymeric liquids above the glass transition and melting temperatures. If the polymer melt is cooled below its melting temperature T_m, it forms semi-crystalline solid or if cooled below its glass transition temperature T_g, it forms polymeric glass. A polymer chain in melt or in solution has many different conformations. In the scenario of ideal chains, the polymer chains do not interact with the monomers that are far apart along the chain, even if they appear spatially close. Such interactions are present in real chains and they affect the polymer conformations. Real chains interact with both the solvent and with themselves. The relative strength of these interactions decides the conformation of real polymer chains. At high temperature monomer-monomer interaction is dominated by repulsive interactions and the chains swell, while at low temperatures the attractive interaction between the monomers dominates, and the real chains are in the collapsed conformations. At a special intermediate temperature called θ-temperature, the attractive and repulsive monomer interactions cancels each other, and the chains are in nearly ideal conformations. For example, the θ-temperature for polystyrene in cyclohexane is 34.5°. Linear polymer melts and concentrated solutions have ideal chain conformations because the interactions between monomers are almost completely screened by surrounding chains. [19]

CG simulations are an efficient technique to access molecular properties at longer length and time scales compared to atomistic simulations. [60] In case of polymer simulations, particularly for polymer melts, the CG simulations are an effective means to obtain the equilibrium properties such as chain conformation, bulk thermodynamic data and chain dynamics. [61–64] During the last two decades attempts in develop multiscale models of polymeric systems have been explored. The aim is to able to access the experimental length and time scales which are normally much larger than those accessible to standard atomistic models. [65] There are numerous reports where scientists try to link the atomistic to mesoscopic scales and then back to the atomistic scale by reverse mapping [66–81] or even to merge atoms and coarse-grained beads in a single model. [82, 83] A common and widely used way to address this issue is to develop CG models from atomistic systems by merging groups of chemically connected atoms into beads (or superatoms). The lost degrees of freedom are considered unimportant for the properties which can be described in the CG scale. Apart from the reduction in the total number of particles, the interaction

potentials get simplified because the potential energy surface becomes smoother leading to the acceleration of the system dynamics. [84] CG methods have been effectively used in the past to study biological systems [78, 85, 86], polymer dynamics [72, 75, 76, 87], ionic liquids [88], and liquid crystalline compounds [89]. There are various CG methods proposed in the literature depending upon the accuracy, level of CG and simplification of the potential energy surface, and one determines the method of coarse-graining depending upon the properties which they aim to reproduce. Based on the desired system properties one can chose the degree of coarse-graining and decide on a method for deriving inter bead potentials. In the structure-based methods (e.g., iterative Boltzmann inversion (IBI), [69, 78, 90–93] inverse Monte Carlo, [94] Newton inversion methods [95]), the link between the atoms and CG beads are through the effective bonded and non-bonded potentials. In the force matching methods by Voth et al. [96, 97] the forces in the CG systems are determined such that they are mapped to the corresponding sum of the forces in the corresponding atomistic system.

1.4 Why molecular simulations?

Computer simulations provide detail insight of the interactions of macromolecules and helps us to understand the properties of materials in terms of structure and dynamics. This serves as a complement to experiments, and also provides them with information which are not available otherwise. Molecular simulations connects molecular level interaction to macroscopic properties. In some cases, interaction or properties can also be obtained from simulations where experiments are not possible or expensive or sometime dangerous. For instance, the experiment at high temperature and high pressure are expensive. In our group, we have demonstrated the high pressure molecular dynamics (MD) simulation of methane gas hydrates and also varied temperatures and studied the interactions of methane as guest molecules inside the hydrate cages. [98, 99] MD simulation technique now-a-days are frequently applied to understand the ligand docking, protein folding, lipid membranes, polymer dynamics and many more. We have also shown what drives the disruption of hexagonal mesophase formed by the non-ionic surfactants at high pH in presence of polyethylenimine. [100] MD simulations are also used to study the structural and dynamical properties of carbon nanotubes in the matrix of polycarbonates [101], effect of phosphoric acid as dopents in polybenzimidazole matrix [102, 103] from the fuel cell point of view. In addition to these, lipid membranes [104, 105] and biological inspired materials [106–108] are also investigated.

All atomistic MD simulations are limited by the length and time scales. The time scale ranges from nanoseconds to just a few microseconds. Microsecond simulations have

recently been possible because of the increase in the computing capabilities. There has been a simultaneous increase in the processing power of the computer nodes and the number of processors (or threads) such nodes can hold. Apart from these advancements, graphics processing units (GPUs) are recent addition which facilitates the computing world to crunch the numbers very fast. Thus, using GPUs both larger length and time scale simulation can be achieved. Another way to scale up the length and time, is to consider a simpler system or model which represents the complex system or model when all the atoms were considered. One way to achieve such simpler model is to use the technique of coarse graining. In this method, some atoms linked by chemical bonds are clubbed in a single blob called as 'bead'. This generates simpler model with the reduced degrees of freedom. People also uses phenomenological modeling to access the macromolecular properties at much higher length and time scale. One such method is dissipative particle dynamics (DPD) simulation. DPD technique has found large applications in various fields of soft material. In our group DPD has been used to study the morphology and dynamics of carbon nanotubes in polycarbonate matrix [80], fuel cell membrane [109].

1.5 Organization of thesis

In the present thesis, we have used all atomistic and coarse-grained MD simulations to investigate the behavior of soft matter in different chemical environment. We have used coarse-grained (CG) MD to study the polymer melt properties. Thus, the layout of the thesis is as follows: The first three chapters comprises all atomistic simulations of PEI – water, PEI – surfactant – water and PEI – bilayer – water. chapters 6 and 7 deals with the coarse-grained simulations of polycarbonate melt.

In chapter 2, computational methodologies are discussed in brief.

In chapter 3, conformational and dynamical study of PEI in protonated and unprotonated states are discussed.

In chapter 4, interaction of PEI with non-ionic surfactant is discussed.

In chapter 5, interaction of PEI with lipid bilayer is discussed.

In chapters 6 and 7, we had used the coarse-grained simulation technique to investigate the structural and dynamical properties in polymer melt. Thus,

In chapter 6, importance of torsions in the CG simulations of polymer melts is discussed.

In chapter 7, *scalability* of coarse-grained potentials for polymers is discussed.

In chapter 8, conclusions from above studies are discussed.

Chapter 2

Methodology

In this thesis we have used MD simulations to understand and predict the behavior of soft molecular systems. The investigation at the nanosecond time and nanometer length scales were studied using classical all atom molecular dynamics, while coarse-grained molecular dynamics were used for the microsecond time and/or micrometer (or nanometer) length scales. We have briefly outlined these two method in the following sections.

2.1 Classical all atom molecular dynamics

We have primarily used molecular dynamics (MD) simulation technique to understand the molecular level interactions. Such interactions govern the macroscopic properties of the system. In MD simulations, we consider the movement of atoms occurring at the nanoscale time. This movement of atoms in terms of positions (coordinates) and velocities with time are stored in the computer and are referred as *trajectory*. The position and velocities of each and every particles in the system are determined by solving the Newton's equation of motion given as Equation (2.1).

$$m_i \frac{\partial^2 \boldsymbol{r}_i}{\partial t^2} = \boldsymbol{F}_i, \ i = 1...N \tag{2.1}$$

where $m_i, \boldsymbol{r}_i$, and $\boldsymbol{F}_i$ respectively, are the mass, positions, and forces of the particle i in the system of N particles. The force on the particle i is calculated as the negative gradient of the potential energy, $V(\boldsymbol{r}_1, \boldsymbol{r}_2, ..., \boldsymbol{r}_N)$ (see Equation (2.2)).

$$\boldsymbol{F}_i = -\frac{\partial V(\boldsymbol{r}_1, \boldsymbol{r}_2, ..., \boldsymbol{r}_N)}{\partial \boldsymbol{r}_i} \tag{2.2}$$

The potentials energy is computed from the contributions of bonded and non-bonded interactions. The bonded interactions include the bonds, angles and dihedrals, while

non-bonded interactions comprises of Lennard-Jones and Coulomb terms. These terms are defined as *force field*.

2.1.1 Force field

A potential form is chosen such that it represents the chemistry and physics of the system of interest. The functional form of the potentials are empirical in nature, which has adjustable parameters. These parameters defined as the *force field* are chosen such that the empirical potential represents a good-fit to the experimental data or to the relevant regions of the *ab initio* Born-Oppenheimer surface. In a conventional MD simulation, the total potential energy of the system is described by the bonded and non-bonded components. It is computed as the sum of these components (Equation (2.3)).

$$\begin{aligned} V(\boldsymbol{r}_1, \boldsymbol{r}_2, ..., \boldsymbol{r}_N) = & \frac{1}{2} \sum_{\text{bonds}} k_{ij}^{bond} (b_0 - b_{ij})^2 \\ & + \frac{1}{2} \sum_{\text{angles}} k_{ijk}^{angle} (\theta_0 - \theta_{ijk})^2 \\ & + \sum_{\text{dihedrals}} k_{ijkl}^{dihedral} [1 + cos(n\phi - \phi_s)] \\ & + \sum_{\text{atom pairs}} 4\epsilon_{ij} \left[\left(\frac{\sigma_{ij}}{r_{ij}} \right)^{12} - \left(\frac{\sigma_{ij}}{r_{ij}} \right)^{6} \right] \\ & + \sum_{\text{atom pairs}} \frac{q_i q_j}{4\pi\epsilon_0 \epsilon_r r_{ij}} \end{aligned} \tag{2.3}$$

The first three terms summation runs over all the bonds, angles, and torsions defined in the system, whereas the last two terms the summations are over the pairs of the atoms, separated by distance $r_{ij} = |r_i - r_j|$ and not chemically bonded. The dummy indices (i, j, k, l) are the individual atom in the system of N atoms. Physically, the first two terms represents the energies of deformations of the bond lengths b_{ij} and angles θ_{ikj} from their respective equilibrium values b_0 and θ_0. The harmonic form of these terms (with force constants k_{ij}^{bond} for bonds, and k_{ijk}^{angle} for angles) ensures the correct chemical structure. It also prevents the chemical changes such as bond breaking. Force constants are an indication of the strength of energy required to stretch a bond, or to distort an angle for their equilibrium position. The energy required to stretch a bond (thus the force constants) are higher than to distort an angle from equilibrium. The third term describes rotations around the chemical bond, which are characterized by periodic energy terms (with periodicity determined by n and heights of rotational barriers defined by $k_{ijkl}^{dihedral}$). Molecules might adopt different conformations because of the low rotational energy barrier about chemical bonds. Thus, torsions play a crucial role and is fundamental to understand the structural properties of molecules and its conformational analysis. The

fourth term describes the van der Waals repulsive and attractive (dispersion) interatomic forces in the form of the Lennard-Jones (LJ) 12-6 potential, and the last term is the Coulomb electrostatic potential. In the LJ expression (Equation (2.3)) ϵ_{ij} is the strength of the potential energy. It is the depth of the potential wall. It measures how strongly two atoms i and j attract each other. The lower the value of ϵ_{ij}, the deeper is the well depth, the stronger is the interaction between two atoms. While σ_{ij} is the distance at which the inter-atomic potential between atoms i and j is zero. It measures how close two non-bonding atoms can get and is thus referred as van der Waals radius. It is equal to the one-half of the inter-nuclear distance between two non-bonding atoms. In the Coulombic potential, q_i and q_j are the partial charges on atoms i and j. ϵ_0 and ϵ_r are the dielectric constant in vacuum and relative dielectric constant. Once the potential energy is evaluated, the force acting on particle i by other particles is evaluated as the derivative of the potential energy (see Equation (2.2)).

2.1.2 Force calculation and long-range interactions

In MD, the forces between the molecules are explicitly calculated. Once the forces have been calculated, the equations of motions can be integrated forward in time. The calculation of force acting on every particle is the most time consuming part of the molecular dynamics simulations. If we consider a model system with pairwise additive interactions, the force on particle i is due to all its $N-1$ neighbors in a system of N atoms. Thus, there are $N(N-1)$ unique pairs for which force needs to be calculated. The time needed for the evaluation of such force scales as N^2. However, a cut-off is generally applied at a certain interatomic separation, beyond which the force is assumed to be zero. This reduces the number of pairs (as, atoms within the cutoff are only considered, and rest are discarded) increasing the efficiency in computing the forces. Short ranged interactions are commonly dealt with by imposing a cut-off to the potential $V(r)$, beyond which $V(r)$ is set to 0. By short ranged interactions, we mean that the total potential energy of a particle i is dominated by interactions with neighboring particles within the cut-off distance. These interactions decay rapidly (beyond cut-off) with distance. The contribution of LJ potential at 2.5 σ is just 1% of its value at σ. The contributions to the pressure and energy arising from the ignored interactions can be added using the correction formulae. [110] The forces have to be recomputed at every step. Therefore the repeated calculation of the forces defines the overall complexity of the MD algorithm. The introduction of cell list in the force calculation reduces the computational cost and speed up the simulation. In 1967, Verlet suggested a technique in which a list of neighbors for every particle was recorded and this list was only updated at intervals. [111] Now, between the updates, neighbors for particles were not searched and instead force were

computed (as the positions changed) by considering the neighbors those appearing on the list. This saved the time and thus improved the speed of the simulation. Apart from short-ranged interactions, clever techniques are developed to take care of the long ranged forces. The long ranged interactions decay no faster than r^{-n}, where n is the dimensionality of the system, can be problem as their range can often be greater than half of the box length. [112] The charge-charge electrostatic interactions decay as r^{-1}. As they are infinite ranged, the simulation cell and all its periodic images must be considered. Which implies that the contribution to the total potential energy is from the interaction of the central box (simulation box) and all image boxes. Thus the summation also runs over the *periodic images*. Now, the electrostatic term of Equation (2.3) looks like Equation (2.4).

$$\mathcal{V}_{Coul} = \frac{1}{4\pi\epsilon_0\epsilon_r}\frac{1}{2}\sum_{|\boldsymbol{n}|=0}{}'\sum_{i=1}^{N}\sum_{j=1}^{N}\frac{q_i q_j}{|\boldsymbol{r}_{ij}+\boldsymbol{n}|} \tag{2.4}$$

where $\mathcal{V}_{Coul}$ is the total electrostatic energy, the sum over $\boldsymbol{n}$ is the sum over all simple cubic lattice points $\boldsymbol{n} = (\boldsymbol{n}_x L, \boldsymbol{n}_y L, \boldsymbol{n}_z L)$ with $\boldsymbol{n}_x,\ \boldsymbol{n}_y,\ \boldsymbol{n}_z$ being integers. These vectors reflects the shape of the basic box. The prime indicates that we omit $i = j$ for $\boldsymbol{n} = 0$. To handle such interactions, Ewald converted the summation (Equation (2.4)) into two series, each of one converges very rapidly. One in real space and the other in Fourier or reciprocal space. [113] The introduction of fast Fourier transformation reduced the scaling from N^2 to $N\log N$. [114] An popular technique to handle to electrostatics is the reaction field method where it is assumed that the molecules beyond the cut-off can be modelled as continuous dielectric. [115] This is a reasonable assumption for the homogenous fluids such as polymer melts. Reaction field method is conceptually simple, relatively easy to implement and computationally efficient, while Ewald summation method is computational expensive to implement. Particle meshed Ewald method are now-a-days popular with highly charged or polar systems such as ionic melts. It is also applied to the systems electrostatic effects are important such as lipid bilayers, DNA and proteins.

Periodic boundary conditions Periodic boundary condition (PBC) enable a simulation to be performed in a relatively small number of particles, in such a way that the particles experience forces as if they were in bulk fluid. The correct treatment of boundaries and its effect are important as the macroscopic properties are determined using relatively small number of particles. In periodic boundary conditions, the cubical simulation box is replicated throughout space to form an infinite lattice. In the course of the simulation, when a molecule moves in the central box, its periodic image in every one of the other boxes moves with exactly the same orientation in exactly the same

way. Thus, as a molecule leaves the central box, one of its images will enter through the opposite face. This phenomena is illustrated in Figure 2.1. There are no walls at the boundary of the central box, and the system has no surface. It is not necessary to store the coordinates of all images in a simulation (this would be an infinite number), just those of the molecules in the central box. When a molecule leaves the box by crossing a boundary, attention may be switched to the identical molecule just entering from the opposite side. This removes any influence of the walls on the system. As a result the surface effects are eliminated. Other shapes than the simple cube are also possible.

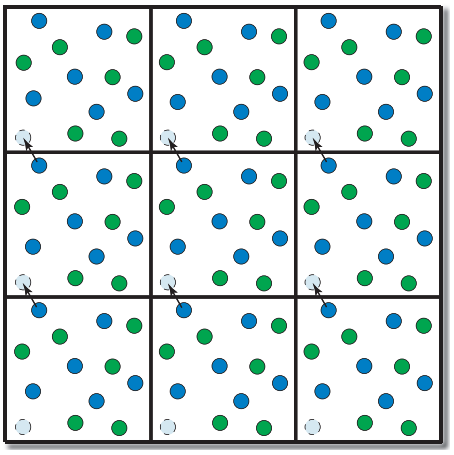

FIGURE 2.1: Illustration of the periodic boundary condition. As a particle crosses the simulation cell boundary, its mirror image can be seen to enter the simulation cell at the opposite boundary.

Minimum image conventions As a result of applying PBC the number of interacting pairs increases enormously. This is because of each particle in the simulation box not only interacts with other particles in the box but also with their images. This problem can be handled by choosing a finite range potential within the criteria of minimum image convention. The essence of the minimum image criteria is that it allows only the nearest neighbors of particle images to interact. The simulation cell is thought to be centered on to a particle, and a simulation cell is drawn with same shape and size (dashed cube Figure 2.2(a)). All other particles fall in this cell. For a system with N particles, $\frac{1}{2}N(N-1)$ terms are involved in the computation of forces and energy. This task is enormous and to reduce it, a spherical truncation cut-off (see Figure 2.2(b)) is imposed which is less than the half of box length (to comply with minimum image convention). This truncation is justified as the potential are short ranged. The maximum length can be equal to the half of the box length used in the simulation.

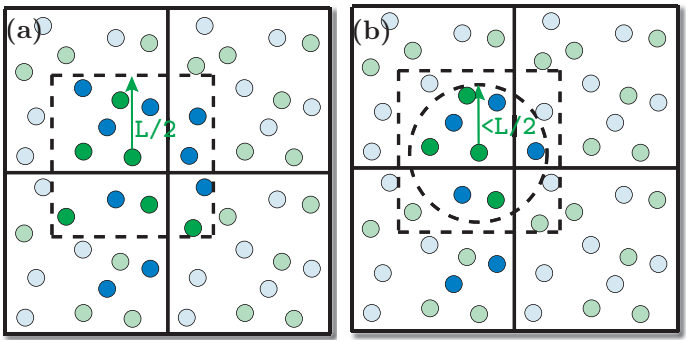

FIGURE 2.2: Illustration of minimum image convention (a) where a simulation cell is re-drawn with the center of a particle, (b) where the particles lying within the spherical truncation is considered.

2.1.3 Equation of motion integrator

Once the forces of all the particles are computed, we can now integrate the Newton's equations of motion. The Equation (2.1) can be integrated using a finite difference approximations. The finite difference method can generate MD trajectories with continuous potential models. The essential idea is that the integration is divided into many small steps, each separated by a fixed time interval δt. The total interactions on each particle at time t can be calculated from the sum of interactions from other particles. The force is assumed to be constant during the time step t and $t + \delta t$. The forces and accelerations of the particles in new positions can be determined, and so on.

There are many algorithms for integrating the equations of motion using finite difference methods in MD simulations. All algorithms assume that the positions and dynamics properties (velocities, accelerations, etc.) can be approximated in Taylor series expansions about positions, velocities, accelerations etc. Verlet algorithm [111], leap-frog algorithm [116], velocity Verlet algorithm [117], and Beeman's algorithm [118] are the commonly used integrators. We have used the leap-frog integrator algorithm [116] to carry out the simulations.

Leap-Frog integrator This algorithm evaluates the velocities at the half-integer time steps and uses these velocities to compute the new positions. Leap-Frog algorithm can be derived using Taylor's expansion. Taylor expanding $\boldsymbol{r}(t + \delta t)$ about $\boldsymbol{r}(t)$ gives:

$$\boldsymbol{r}(t + \delta t) = \boldsymbol{r}(t) + \boldsymbol{v}(t)\delta t + \frac{1}{2}\frac{\boldsymbol{F}(t)}{m}\delta t^2 \tag{2.5}$$

Here, $\boldsymbol{v}(t) = \dot{\boldsymbol{r}}(t)$, $\frac{\boldsymbol{F}(t)}{m} = \boldsymbol{a}(t) = \dot{\boldsymbol{v}}(t) = \ddot{\boldsymbol{r}}(t)$ and δt is the simulation time step. The velocity at half-integer time step can be defined as:

$$\boldsymbol{v}(t + \frac{1}{2}\delta t) = \boldsymbol{v}(t) + \frac{1}{2}\frac{\boldsymbol{F}(t)}{m}\delta t \tag{2.6a}$$

$$\text{Also, } \boldsymbol{v}(t + \frac{1}{2}\delta t) = \boldsymbol{v}(t - \frac{1}{2}\delta t) + \frac{\boldsymbol{F}(t)}{m}\delta t \tag{2.6b}$$

Using this expression (Equation (2.6a)), Equation (2.5) becomes:

$$\boldsymbol{r}(t + \delta t) = \boldsymbol{r}(t) + \boldsymbol{v}(t + \frac{1}{2}\delta t)\delta t \tag{2.7}$$

Also, the velocities at time t can be calculated as $\boldsymbol{v}(t) = \frac{1}{2}[\boldsymbol{v}(t + \frac{1}{2}\delta t) + \boldsymbol{v}(t - \frac{1}{2}\delta t)]$.

The stored quantities for the leap-frog algorithm is the current positions $\boldsymbol{r}(t)$, force or accelerations $\frac{\boldsymbol{F}(t)}{m}$ and the velocities at the half-step $\boldsymbol{v}(t - \frac{1}{2}\delta t)$. At first the velocities $\boldsymbol{v}(t + \frac{1}{2}\delta t)$ are calculated from the velocities at $(t - \frac{1}{2}\delta t)$ and acceleration $(\frac{\boldsymbol{F}(t)}{m})$ at time t (Equation (2.6b))(Figure 2.3(c)). Then the positions $\boldsymbol{r}(t + \delta t)$ are determined from the just calculated velocities and the position at time t (Figure 2.3(d)). The positions and velocities 'leap over' each other. Only at the beginning of the integration we have to set the value of the velocities at half integer time step. Using the given coordinates as $\boldsymbol{r}_0$ (an input to the simulations) and an initial velocities $\boldsymbol{v}_0$ (can be generated according to Maxwell distribution at temperature T), $\boldsymbol{v}(\frac{1}{2}\delta t)$ can be computed by considering the first term of the Taylor series expansion, thus:

$$\boldsymbol{v}(\frac{1}{2}\delta t) = \boldsymbol{v}(0) + \frac{1}{2}\frac{\boldsymbol{F}(t)}{m}\delta t \tag{2.8}$$

The position of each particles in the system varies with time. We solve Newton's equations of motion until the system is equilibrated i.e., the properties of the system does not change with the time. After the equilibration is reached, we compute macroscopic properties from the equilibrium trajectory. In practice δt is determined by fast motions in the system. Bonds involving light atoms (e.g. the O–H bond) vibrate with periods of several femtoseconds, implying that δt should be on a subfemtosecond scale to ensure stability of the integration. Although the fastest and not crucial vibrations can be eliminated by imposing constraints on the bond length in the integration algorithm, a time step of 2 fs are generally used with constraints.

Initial velocities To carry out the MD simulations, generally we need the initial positions and velocities of all the atoms. The initial coordinates can correspond to the Cartesian coordinates of the initial geometry of the system, which can be created with

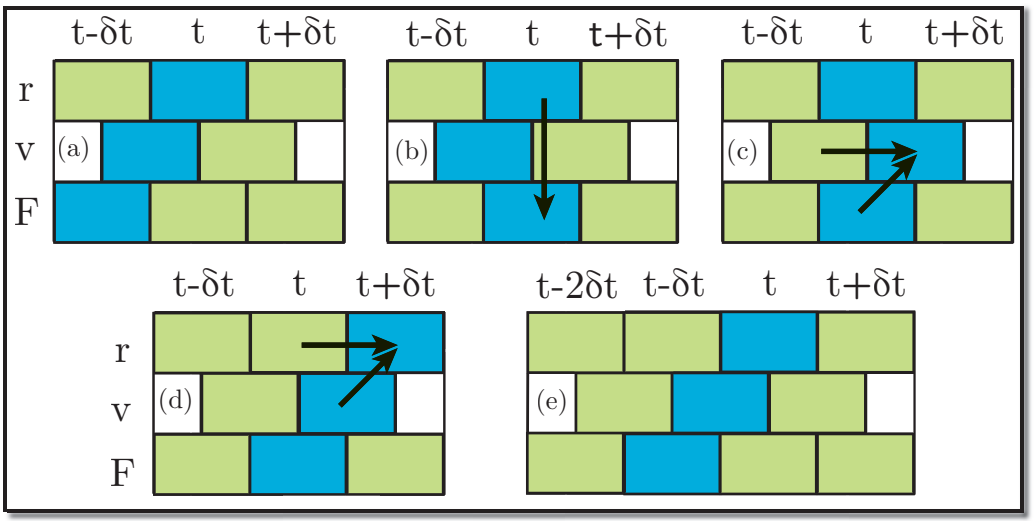

FIGURE 2.3: Illustration of the leap-frog algorithm. (a) Current position, and velocity and 'half-step', (b) Computation of current force, (c) Computation of velocity at half-step, (d) Computation of next position, (e) Advance to next time and repeat.

a software package of choice. The initial velocities are, however, randomly drawn from Maxwell-Boltzmann distribution at the desired temperature:

$$P(v_{x,i}) = \left(\frac{m_i}{2\pi k_B T}\right)^{1/2} \exp\left(-\frac{m_i v_{x,i}^2}{2\pi k_B T}\right) \tag{2.9}$$

The above equation provides us the probability that an atom i of mass m_i has a velocity $v_{x,i}$ in the x-direction at a temperature T. A Maxwell-Boltzmann distribution is a Gaussian distribution, which can be obtained using a random number generator. The form of this distribution is gaussian with zero mean:

$$\begin{aligned} P(v_{x,i}) &= (2\pi\sigma_v^2)^{-1/2} \exp\left(\frac{-v_{x,i}^2}{2\pi\sigma_v^2}\right) \\ \sigma_v^2 &= \frac{k_B T}{m_i} \end{aligned} \tag{2.10}$$

The velocities are random for each of the $3N$ components with positive and negative signs. However, the randomly picking the velocities leads to a non-zero net momentum of the system which would create systematic translational drift in the system. To set the total linear momentum of the system to zero, the sum of the components of the atomic momenta along the x, y, and z axes is calculated. This gives the total momentum of the system in each direction which when divided by the total mass, is subtracted from the random atomic velocities to give an overall momentum of zero. For systems without boundaries or fields, we typically also remove the net angular momentum, which prevents our system from rotating. [112]

Choice of time step The time step (δt) is used by the integrator algorithm to advance the positions and velocities of all the atoms in a MD simulations. Too small time step results the trajectory to scan a limited portion of phase space, while too large causes instabilities in the integration algorithm due to high energy overlaps between atoms. Such instabilities will definitely lead to a violation of energy and linear momentum conservation and the trajectories 'blow up'.

When simulating an atomic fluid the time step should be small compared to the mean time between collisions. However, when simulating flexible molecules the time step is generally taken as one-tenth time of the shortest period of motion. It represents the fastest motion in the system which is generally the bond stretching. One of the fastest bond stretching motions corresponds to the C-H bonds, whose typical bond stretching frequency are about $3000\,\mathrm{cm}^{-1}$ corresponds to a period of vibration of $\sim$10 fs. Thus, to ensure sufficient data point per C-H vibration, the time step is generally set to 1 fs. These high frequency vibrations are sometimes of very little interest as they have minimal effect on the global behavior of system. In this case, it is safer to neglect these motions by 'freezing out' such vibrations. We constrain these vibrations especially the bond vibrations at the equilibrium value while pertaining the rest of the degrees of freedom to vary under the intra- and inter molecular forces. This enables a longer time step to be used. Such bond constraints are incorporated in MD simulation using LINCS [119, 120] or SHAKE [121] algorithms. Some typical motion together with appropriate time steps are shown in Table 2.1. [112]

Table 2.1: Different types of motion and suggested time steps.

System	Types of motion present	Time steps (fs)
Atoms	Translation	10
Rigid molecules	Translation and rotation	0.5
Flexible molecules, rigid bonds	Translation, rotation and torsion	2.0
Flexible molecules, flexible bonds	Translation, rotation, torsion, vibration	1.0

2.1.4 Molecular dynamics in different ensemble

In the conventional MD technique, the total energy E and total linear momentum P are the constants of motion. Such systems are referred as microcanonical ensemble (NVE). To measure any observables we compute its time averages. This time average also corresponds to the ensemble average as laid down by Ergodic hypothesis. The basic idea of this hypothesis is to allow the system to evolve in time, and in doing so, it passes or scans all the possible states. Most of the experiments are performed at constant N, V, T (canonical ensemble) or constant N, P, T (isothermal-isobaric ensemble) ensembles as the temperature and pressure can be easily controlled. Constant N, V, E (microcanonical

ensemble) are very rare. To perform constant NVT and constant NPT various schemes are prescribed. Here, we outline the methods we have used for our study.

2.1.4.1 Constant temperature molecular dynamics

The temperature of the system can be monitored from the average kinetic energy of the system. For an unconstrained system, it is given as:

$$\frac{1}{2}\sum_{i=1}^{N} m_i v_i^2 = \frac{3}{2} N k_B T \tag{2.11}$$

This definition can be used to compute the temperature. As the total kinetic energy of the system fluctuates, so does the instantaneous temperature $T(t)$. $T(t)$ varies with t. Thus,

$$T(t) = \frac{1}{2}\sum_{i=1}^{N} \frac{2 m_i v_i^2(t)}{3 N k_B} \tag{2.12}$$

$T(t)$ can be scaled to the desired T by scaling the velocities such that the total kinetic energy is constant. The scaling factor λ can be determined as $(T/T(t))^{1/2}$ and can be multiplied to the velocities at each time step. This method does not allow the fluctuations in the temperature which is inherent to canonical (NVT) ensemble. The fluctuations in kinetic energy σ_k according to statistical mechanics of the canonical ensemble is $\sigma_k^2 = \frac{3}{2} N k_B^2 T^2$. As we rescale the velocities at every time step, the kinetic energy remains constant with zero fluctuations. Thus, it does not capture the correct energy fluctuations in the system. Hence, the correct thermodynamic properties of the canonical ensemble are not generated.

Berendsen thermostat An another popular velocity scaling method is given by Berendsen. [122] The basic idea is to add a frictional term to the equations of motion. In this method the system is weakly coupled to the external heat bath which is kept at a desired temperature T. The bath acts as a source of the thermal energy, pumping or extracting heat from the system as needed. The velocities are scaled at each step such that the rate of change in the temperature is proportional to the difference in temperature of the bath (T) and system:

$$\frac{dT(t)}{dt} = \frac{1}{\tau}(T - T(t)) \tag{2.13}$$

where τ is the coupling parameter. It determines how tightly the bath and the system are coupled together. Solving Equation (2.13) gives us an exponential decay of $T(t)$

towards the desired temperature T:

$$T(t) = T - Ce^{-t/\tau}, \text{where } C \text{ is an integration constant.} \tag{2.14}$$

Equation (2.13) can also be written as Equation (2.15), which gives us the change in temperature between successive time steps.

$$\delta T = \frac{\delta t}{\tau}(T - T(t)) \tag{2.15}$$

The scaling factor λ used (in practice) to scale the velocities is:

$$\lambda^2 = 1 + \frac{\delta t}{\tau}\left\{\frac{T}{T(t - \frac{1}{2}\delta t)} - 1\right\} \tag{2.16}$$

The $T(t - \frac{1}{2}\delta t)$ is from the fact that the leap-frog integrator is used for solving the Newton's equation of motion. In the limit $\tau \to \infty$, the Berendsen thermostat becomes inactive and the simulation runs in microcanonical ensemble. The very small value of τ will result in unrealistic low temperature fluctuations. If $\tau = \delta t$, then the Berendsen thermostat transforms to simple velocity scaling. Typically, $\tau = 0.1 - 0.4\,\text{ps}$ for $\delta t = 1\,\text{fs}$. Berendsen thermostat also suffers with the same problem as that of velocity scaling, the energy fluctuations are not captured correctly. Thus, the ensemble generated is not a canonical ensemble!

Velocity-rescaling Berendsen thermostat was modified as Equation (2.17) by adding an additional stochastic term which ensures the correct kinetic energy distribution. [123]

$$dK = (K_0 - K)\frac{dt}{\tau} + 2\sqrt{\frac{KK_0}{N_f}}\frac{dW}{\sqrt{\tau}}, \tag{2.17}$$

where K is the kinetic energy, N_f the degrees of freedom, and dW a Wiener process. This thermostat produces correct canonical ensemble.

2.1.4.2 Constant pressure molecular dynamics

We have seen in the previous section that the temperature can be specified or fixed in a MD simulation. In the same spirit, the pressure can also be controlled. In this case the system's volume becomes the dynamic quantity and it changes during the simulation. In simulation, pressure is defined as the ensemble average of the instantaneous or microscopic pressure, $\mathcal{P}$. For a system of N particles in a volume V, microscopic pressure is defined

as [124]:

$$\mathcal{P} = \frac{1}{V}\left(\frac{1}{3}\sum_i m_i \boldsymbol{v}_i \cdot \boldsymbol{v}_i + \frac{1}{3}\sum_i \boldsymbol{r}_i \cdot \boldsymbol{F}_i\right) \tag{2.18}$$

In the absence of external fields, the only contribution to the forces ($\boldsymbol{F}_i$) arises from the intermolecular interactions. The macroscopic pressure P is simply obtained as $P = \langle \mathcal{P} \rangle$, where the angular brackets indicate either a time or statistical average over the appropriate ensemble. In the case of a system with pairwise interactions $V(r_{ij})$, the pressure can be written explicitly in the usual virial form as:

$$P = \langle \rho k_B T \rangle + \left\langle \frac{1}{3V} \sum_i \sum_{j<i} \boldsymbol{r}_{ij} \cdot \frac{dV(r_{ij})}{dr_{ij}} \right\rangle \tag{2.19}$$

where $\rho = N/V$ is the number density, $\boldsymbol{r}_{ij}$ is the intermolecular vector between a molecular pair, and $\boldsymbol{F}_{ij}$ is the corresponding intermolecular force. The first term on the right-hand side of Equation (2.19) is the kinetic (ideal gas) contribution and the second term represents the residual contribution arising from the interparticle interactions. This mechanical route to the calculation of the pressure in a simulation is particularly well suited when molecular dynamics is the technique of choice, as the evaluation of the forces is required to determine the molecular trajectories. [124] Also, this expression has the additional advantage to be naturally suited to be used when periodic boundary conditions are present: it is sufficient to take them into account in the definition of $\boldsymbol{r}_{ij}$.

Berendsen barostat In the constant pressure simulations, the pressure is maintained by changing the volume of the simulation cell. The volume fluctuation is related to isothermal compressibility κ:

$$\kappa = -\frac{1}{V}\left(\frac{\partial V}{\partial P}\right)_T \tag{2.20}$$

An easily compressible substance has larger κ, so at a given pressure large fluctuation in volume occurs. The pressure can be controlled in a MD simulation in the similar way as the temperature is controlled. Volume can be scaled to maintain the pressure. An alternative to this scaling is the introduction of 'pressure bath' analogous to temperature bath. This method was proposed by Berendsen. [122] The rate in change in the pressure is given as:

$$\frac{dP(t)}{dt} = \frac{1}{\tau_p}(P - \mathcal{P}) \tag{2.21}$$

where τ_p is the coupling constant, and P the 'bath' pressure or desired pressure. The volume of the simulation box is scaled by a factor λ, which is similar to scaling the atomic coordinates by a factor of $\lambda^{1/3}$. Thus,

$$\lambda = 1 - \kappa\frac{\delta t}{\tau_p}(\mathcal{P} - P) \tag{2.22}$$

The all atomistic simulations provide detailed insight on the atomic length scales. It also explains the phenomena at the nanosecond time scale. Sometime, it becomes necessary to understand the molecular insights at the larger length and time scales. The study of polymer melts is such an example where we have used the coarse-grained MD simulations to investigate its structural and dynamical properties.

2.2 Coarse-grained molecular dynamics

The coarse-grained molecular dynamics (CGMD) simulation technique is an efficient way to access the longer time and larger length scales, which are not accessible by the atomistic or united atom model simulations. [125, 126] CG simulation is accomplished by grouping the atoms into fewer interaction sites (forming super atoms). Such CG model does reduce the degrees of freedom and they must preserve the interaction details necessary to reproduce the chemical features of the system. [66] CG method can be broadly divided into two classes based on the procedure used to parameterize the force field acting among the super atoms. Structure based techniques like Boltzmann inversion [90], Iterative Boltzmann inversion (IBI) [69], and Inverse Monte Carlo [94] are employed in CG simulations to obtain the CG potentials. Apart from structure based approaches, force matching method where the CG potentials are generated such that the average force on the super atoms in the CG system matches to that of the fine grain system. [94, 127] Once the effective potential between the coarse-grained beads are obtained, a coarse-grained trajectory can be generated by solving Newton's law of motion using the integrator discussed in section 2.1.3.

2.2.1 Boltzmann inversion

Boltzmann inversion has become a popular method to derive CG potentials due to its straightforward nature and general applicability. It is a structure based method which method optimizes a potential to match target properties from an atomistic simulation mapped to the CG level. It is mostly used for bonds, angles, and torsions. The idea of Boltzmann inversion is that in a canonical ensemble *independent* degrees of freedom q obey the Boltzmann distribution (Equation (2.23)), i.e., [128]

$$P(q) = Z^{-1} \exp[-\beta V(q)]], \tag{2.23}$$

where $Z = \int \exp(-\beta V(q))dq$ is a partition function, $\beta = 1/k_B T$. Once the probability distribution $P(q)$ is known, one can obtain the potential $V(q)$ (Equation (2.24)) by inverting the $P(q)$ of a variable q. For a coarse-grained simulations, q represents either

bond length r, bond angle θ, or torsions angle ϕ.

$$V(q) = k_B T \ln P(q) \tag{2.24}$$

In practice $P(q)$ is computed from the trajectory of the reference system generated either molecular dynamics or Monte Carlo simulations.

Boltzmann inversion is simple to implement, however one has to be careful with the rescaling of probability P due to the orientation entropy and computational issues. The coarse-grained potential V, for example for a polymer beads, depends upon r, θ, and ϕ. Assuming the independence of coarse-grained degrees of freedom, we can write the probability distribution as a factor of the distribution of the bond length $P_r(r)$, bond angle $P_\theta(\theta)$ and torsional angle $P_\phi(\phi)$ (Equation (2.25)). In other words, we assume that the distributions of these degrees of freedom are decoupled.

$$P(r, \theta, \phi) = P_r(r) P_\theta(\theta) P_\phi(\phi) \tag{2.25}$$

The histograms for the bonds $H_r(r)$, angles $H_\theta(\theta)$, and torsions $H_\phi(\phi)$ must be rescaled in order to obtain volume normalized distributions $P_r(r), P_\theta(\theta),$ and $P_\phi(\phi)$ (Equation (2.26)).

$$P_r(r) = \frac{H_r(r)}{4\pi r^2}, P_\theta(\theta) = \frac{H_\theta(\theta)}{\sin\theta}, P_\phi(\phi) = H_\phi(\phi) \tag{2.26}$$

The coarse-grained potential can then be calculated by Boltzmann inversion of the distribution functions (Equation (2.27)).

$$\begin{gathered} V(r, \theta, \phi) = V_r(r) + V_\theta(\theta) + V_\phi(\phi), \\ \text{with, } V_q(q) = -k_B T \ln P_q(q), \ q = r, \theta, \phi \end{gathered} \tag{2.27}$$

On the technical side, the implementation of the Boltzmann inversion method requires smoothing of $V(q)$ to provide a continuous force. Splines can be used for this purpose. Poorly and unsampled regions, namely regions with high $V(q)$, shall be extrapolated. Since the contribution of these regions to the canonical density of states is small the exact shape of the extrapolation is less important.

2.2.2 Iterative Boltzmann inversion

Iterative Boltzmann inversion (IBI) is a extension of the Boltzmann inversion method. The IBI methodology is based on the uniqueness theorem by Henderson. [92] This theorem states that for a given radial distribution function (RDF), there is a unique pair potential that will produce it. In IBI technique, we search for the inter-particle potential coarse-grained that reproduces a given radial distribution function (target function). The

coarse-grained potential is defined according to the following scheme [128]:

$$\begin{aligned} V^{(n+1)} &= V^{(n)} + \Delta V^{(n)} \\ \text{with, } \Delta V^{(n)} &= k_B T \ln \frac{P^{(n)}}{P_{ref}} = V^{ref}_{\text{PMF}} - V^{(n)}_{\text{PMF}} \end{aligned} \tag{2.28}$$

One can easily see that convergence is reached as soon as the distribution function $P^{(n)}$ matches the reference distribution function P_{ref}, or, in other words, the potential of mean force (PMF), $V^{(n)}_{\text{PMF}}$ converges to the reference potential of mean force. IBI can be used to refine both bonded and non-bonded potentials. It is primarily used for simple fluids with the aim of reproducing the radial distribution function of the reference system in order to obtain non-bonded interactions. [69] On the implementation side, IBI has the same issues as the inverse Boltzmann method, i. e. smoothing and extrapolation of the potential must be implemented. Generally, the radial distribution of the reference or target system ($g^{target}(r)$) is inverted using the Equation (2.29) to obtain the guess potential $V_0(r)$.

$$V_0(r) = -k_B\ T\ \ln\ [g^{target}(r)] \tag{2.29}$$

These potential samples the coarse-grained beads and the obtained distribution $g_i(r)$ are compared with the target system $g^{target}(r)$ using the Equation (2.30). If the $g_i(r)$ is within 0.3% of $g^{target}(r)$ (i.e., $f_{merit} \leqslant 0.003$), we stop the refinement of potential, if not the potential is update according to the Equation (2.31) and proceed for next iteration $i+1$.

$$f_{merit} = \frac{\int_0^r\ [g_i(r) - g^{target}(r)]^2\ dr}{\int_0^r\ [g^{target}(r)]^2\ dr} \tag{2.30}$$

$$V_{i+1}(r) = V_i(r)\ \ +\ \ k_B\ T\ \ln\ [\frac{g_i(r)}{g^{target}(r)}] \tag{2.31}$$

The process of IBI methodology is shown as a flowchart in Figure 2.4.

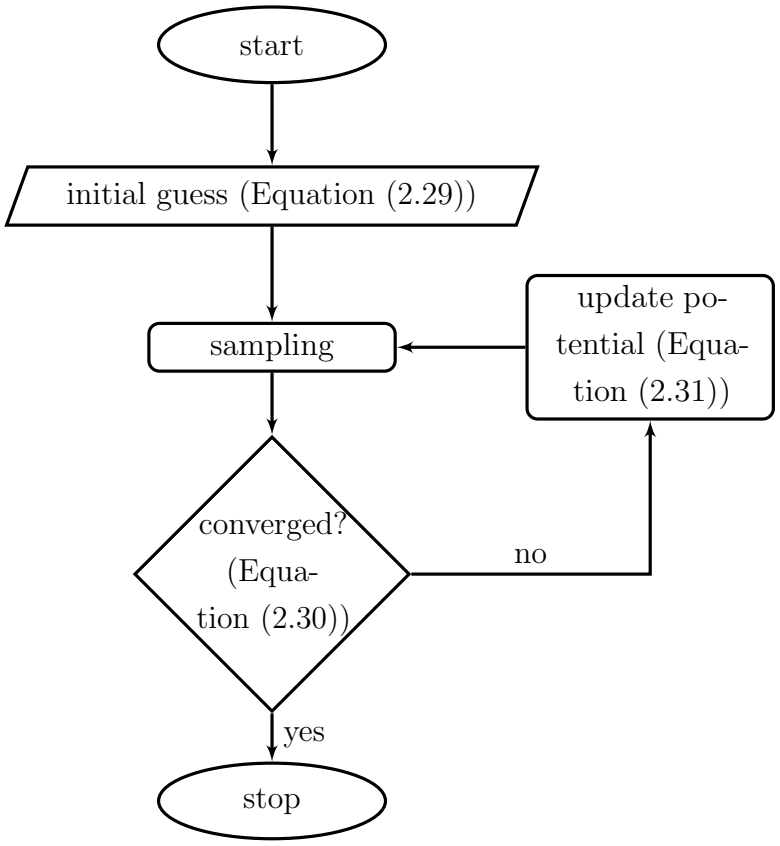

FIGURE 2.4: The flow chart for the refinement of CG potentials using IBI methodology is depicted.

In this way, all the bonded and non-bonded interaction potentials are refined.

Pressure correction Another issue of coarse-graining is that coarse-grained models can not reproduce all the statistical or thermodynamic properties of the reference system. Pressure, or compressibility are often very different from those of the reference system, which is in general not a problem. But in some cases, one needs to correct some of these. The pressure can be corrected iteratively by adding a linear term to the non-bonded potential.

$$\Delta V(r) = A\left(1 - \frac{r}{r_{cut}}\right) \tag{2.32}$$

where A is a prefactor. Its value used by Reith et al. was [69] 0.1 $k_B T$. Usually one can not reach the target pressure in one step of the pressure-correction due to stabilization issues. Therefore, the pressure-correction has to be applied in a different way depending on the coarse-grained system, e. g. every second step of iterative Boltzmann inversion or even after the inversion already converged. The pressure-correction leads to a potential, where the isothermal compressibility deviates significantly from that of the reference system.

In the present thesis, all the simulation are performed using Gromacs simulation suit [129–131]. Gromacs is a fast and flexible parallel code to perform MD simulations. In addition, the all effective coarse-grained potentials for coarse-grained simulations were generated using the VOTCA package. [132] VOTCA stands for Versatile Object-oriented Toolkit for Coarse-graining Applications. VOTCA is a software package which focuses on the analysis of molecular dynamics data, the development of systematic coarse-graining techniques as well as methods used for simulating microscopic charge transport in disordered semiconductors. Some results reported in the present thesis are obtained using the Gromacs analysis tools. All other results are computed using self written codes. Details of such analysis codes are provided as they appear in the different chapters.

Chapter 3

Structural and dynamical properties of Polyethylenimine in explicit water at different protonation states[1]

3.1 Introduction

Solvation of polymers is an physiochemical phenomena where solute interacts with the solvent and one evenly distributes into the other. The solute adopt different conformations depending upon the strength of the solvent-solvent, solute-solute and solvent-solute interactions which results in a solvation structure. The solvation of polymers generates large number of interaction configurations. These solvation structures are very important in the field of life-science and pharmacy. The conformation of polymer in solvent depends upon the nature of solvent. Experimental and theoretical studies have been broadly used to study the conformation of polymers in solution. These methods, though successful, cannot provide light to the detailed solvation structures like monitoring the conformations of every backbone atoms of the polymer chain. Molecular simulations, on the other hand, can produce most of the detailed information about the solvation process. In this thesis we have investigated the solvated structure of polyethylenimine (PEI) chain in explicit water and dynamics of solvation shells around the PEI chain using molecular dynamic simulation (MD). PEI because of its pH buffering capacity is one of the potent cationic

[1]This chapter is adapted from the publication C. K. Choudhury and S. Roy, Structural and dynamical properties of Polyethylenimine in explicit water at different protonation states: a Molecular Dynamics Study, Soft Matter, 2013, 9 (7), 2269 – 2281.

nonviral gene vectors. This unique property of PEI helps the gene carriers to escape the endosomal barrier avoiding lysosomal degradation which is an essential step to achieve high gene transfection. In the process of releasing the genetic cargo, it encounters change in the pH – from basic (outside endosome) to acidic in endosomes. [21, 133] Therefore, a systematic understanding of PEI chains at different protonation state is important to address more complex mechanism of gene delivery.

Very few computational studies have been performed on PEI. Herlem et al. [134] had studied the structural and electronic properties of anhydrate double-stranded linear PEI using the *ab initio* density functional theory (DFT). They have studied the band structures and the corresponding electronic density of states (DOS). Ziebarth et al. [135] used all atomistic MD to simulate 20-mer linear PEI chain. From the MD simulation trajectories, they have evaluated the potentials for the coarse grained PEI chains and used it for Monte Carlo simulations. They obtained the titration curve for the linear PEI and concluded that almost half of the amine groups in linear PEI are protonated, which are arranged in alternate fashion.

Till date the detailed understanding of structure and dynamics of PEI in water is unexplored. Therefore, this work will serve as bridge between the atomistic level structure of PEI and the understanding of more complex phenomena of PEI e.g., gene delivery, diffusion through membrane and endocytosis of PEI-DNA complex that happen at different pH conditions. In this chapter, we have performed MD simulation of linear PEI chain in water at different protonation states. Its detailed structural properties and solvation dynamics have been investigated. The study of solvation dynamics of the polymer chain would also elucidate the behavior of PEI-surfactant system at different protonation states in water. Two different PEI chain lengths (50-mer and 20-mer) are considered here. The structural properties of PEI chains are studied as a function of protonation level. The end-to-end distance and the radius of gyration are calculated and analyzed. We have analyzed the ratio of *syn* to *anti* of the torsional angle to get insight of the favorable polymer conformations. The ordering of water molecules along the polymer chain for different solvation shells are identified. The dynamical properties of water molecules around the polymer chain at different protonation levels are computed to relate mechanism of diffusion of water molecules around the chain with the structure of the polymer chain. The residence time and self-diffusion of water at different temperatures are studied. Also the activation energy is computed for the water molecules of each solvation shells.

3.2 Methods

3.2.1 Computational details

We have performed all atomistic MD simulations of a 20-mer and a 50-mer linear PEI (see Figure 3.1) in water separately by using Gromacs-4.0.7. [130, 131] Nitrogen atoms of NH-group can get protonated at acidic pH and again get deprotonated at basic pH. Therefore, the systems considered here were classified on the basis of level of protonation of the PEI chain viz., all protonated (all the nitrogen atoms were protonated, resembles highly acidic condition), alternate protonated (alternate nitrogen atoms were protonated, acidic condition) and unprotonated (none of the nitrogen atoms were protonated, neutral chain, basic pH condition). The MD simulations were performed using amber forcefield [136, 137] and the results from the 20-mer were compared with the work of Ziebarth et al. [135] TIP3P water model [138] was used to solvate PEI chains for all the systems. Chloride ions were added as counter ion to neutralize the protonated PEI systems.

The total potential energy of the system is the sum of bonded and non-bonded components (see Equation (2.3)). The bonded component is represented by harmonic potential energy functions for bond and angle. Additionally it has dihedral potentials that are either harmonic cosine function or Ryckaert-Bellemans function as given in Equation (3.1). The potential for the dihedral C - C - N - C has cosine function with two-fold components [139] as incorporated in Ziebarth et al. 's work. [135] The other backbone dihedral angle, N - C - C - N, is represented by Ryckaert-Bellemans function.

$$V_{ij}^{dihedral} = \sum_{dihedrals} k_{ijkl}^{dihedral}[1 + cos(n\phi - \phi_s)] \; or \sum_{n=0}^{5} C_n \; (cos(\phi - 180))^n \tag{3.1}$$

The complete list of parameters for the entire bond stretching (Table 3.1), bond bending (Table 3.2), dihedral angle (Table 3.3), van der Waals' (Table 3.4) and Coulombic potentials (Tables 3.5 to 3.7) for unprotonated, alternate protonated and all protonated are tabulated in Tables 3.1 to 3.7.

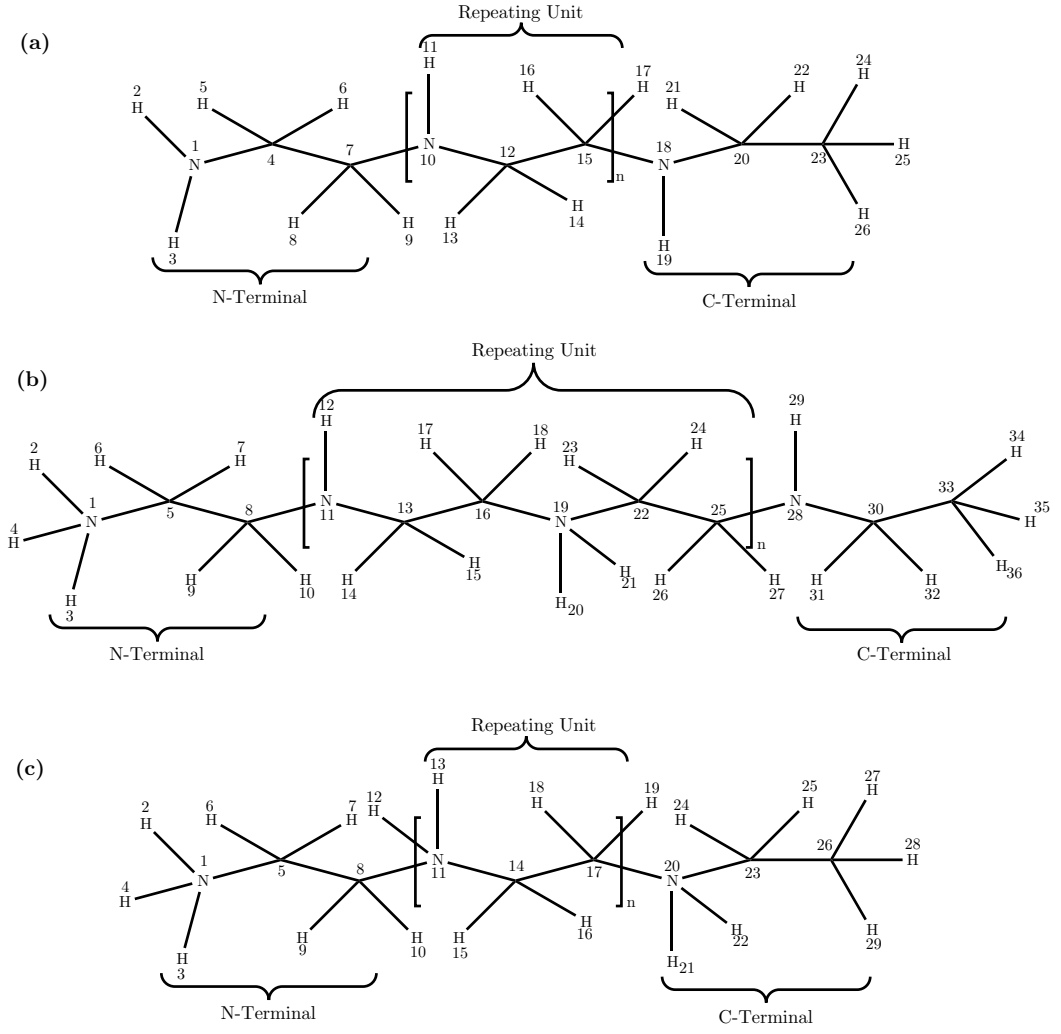

FIGURE 3.1: Structure of PEI with atom number. (a) Unprotonated chain, (b) Alternate protonated and (c) All protonated chain. For unprotonated and all protonated chain n = 18 for 20-mer and 48 for 50-mer, while for alternated protonated chain, n = 9 and 24 for 20 and 50-mer, respectively.

TABLE 3.1: Bond parameters (b_0 and k_{ij}^{bond}, see Equation (2.3)) for the bond between the atom types (ij) in Tables 3.5 to 3.7.

Bond (**Atom types**, ij)	b_0, nm	k_{ij}^{bond}, kJ mol^{-1} nm^2
H - N2	0.10100	363171.2
N2 - CT	0.14630	282001.6
CT - H1	0.10900	284512.0
CT - CT	0.15260	259408.0
CT - NT	0.14710	307105.6
NT - H	0.10100	363171.2
CT - HC	0.10900	284512.0

TABLE 3.2: Bonded angle parameters (θ_0 and k_{ijk}^{angle}) (see Equation (2.3)) for angles formed by the atom types (ijk) mentioned in Tables 3.5 to 3.7.

Angles (**Atom types**, ijk)	θ_0°,	k_{ijk}^{angle}, kJ mol^{-1} rad^2
H - N2 - H	120.0	292.880
H - N2 - CT	118.4	418.400
N2 - CT - H1	109.5	418.400
N2 - CT - CT	111.2	669.400
CT - CT - H1	109.5	418.400
H1 - CT - H1	109.5	292.800
CT - CT - NT	111.2	669.400
CT - NT - H	109.5	418.400
NT - CT - H1	109.5	418.400
CT - NT - CT	109.5	418.400
CT - CT - HC	109.5	418.400
HC - CT - HC	109.5	292.800
H - NT - H	109.5	292.880

TABLE 3.3: Dihedral parameters (ϕ_s and $k_{ijkl}^{dihedral}$, see Equation (3.1)) for Harmonic functions and the values of C_n for Ryckaert-Bellemans functions. X denotes any undefined atom types in the harmonic functions in Tables 3.5 to 3.7

Dihedral (**Atom types**), $ijkl$	ϕ_s	$k_{ijkl}^{dihedral}$ (kJ mol^{-1})	n
H - N2 - CT - CT	0.0	3.7656	3
H - NT - CT - CT	0.0	3.7656	3
H - NT - CT - H1	0.0	3.7656	3
CT - CT - NT - CT	0.0	0.6276	3
CT - CT - NT - CT	180.0	1.004	2

Dihedral (**Atom types**), $ijkl$, kJ mol $^{-1}$	C_0	C_1	C_2	C_3	C_4	C_5
X - N2 - CT - X	0.0	0.0	0.0	0.0	0.0	0.0
X - CT - CT - X	0.65084	1.95253	0.0	-2.60338	0.0	0.0

TABLE 3.4: Lennard Jones parameters (σ and ϵ, see Equation (2.3)) for the atom types mentioned in Tables 3.5 to 3.7.

Atom type	σ, nm	ϵ, kJ mol^{-1}
amber99_11 (CT)	0.339967	0.4577300
amber99_17 (H)	0.106908	0.0656888
amber99_18 (HC)	0.264953	0.0656888
amber99_19 (H1)	0.247135	0.0656888
amber99_38 (N2)	0.325000	0.7112800
amber99_81 (NT)	0.325000	0.7112800

TABLE 3.5: Coulombic parameters (q_i, see Equation (2.3)) for unprotonated PEI chain. See Figure 3.1(a) for atom numbers.

Atom No.	**Atom name**	**Atom type**	**Charge, q_i**
1	N	amber99_38 (N2)	- 0.740
2, 3	H1, H2	amber99_17 (H)	0.250
4	CA	amber99_11 (CT)	- 0.140
5, 6, 8, 9	HA1, HA2, HB1, HB2	amber99_19 (H1)	0.115
7	CB	amber99_11 (CT)	-0.080
10	N	amber99_81 (NT)	-0.593
11,	H	amber99_17 (H)	0.269
12, 15	CA, CB	amber99_11 (CT)	- 0.086
13, 14, 16, 17	HA1, HA2, HB1, HB2	amber99_19 (H1)	0.124
18	N	amber99_81 (NT)	-0.500
19,	H	amber99_17 (H)	0.280
20	CA	amber99_11 (CT)	- 0.081
21, 22	HA1, HA2	amber99_19 (H1)	0.125
23	CB	amber99_11 (CT)	- 0.300
24, 25, 26	HB1, HB2, HB3	amber99_18 (HC)	0.117

TABLE 3.6: Coulombic parameters (q_i, see Equation (2.3)) for alternate protonated PEI chain. See Figure 3.1(b) for atom numbers.

Atom No.	**Atom name**	**Atom type**	**Charge, q_i**
1	N	amber99_81 (NT)	- 0.417
2, 3, 4	H1, H2, H3	amber99_17 (H)	0.360
5	CA	amber99_11 (CT)	0.056
6, 7	HA1, HA2	amber99_19 (H1)	0.087
8	CB	amber99_11 (CT)	-0.147
9, 10	HB1, HB2	amber99_19 (H1)	0.127
11	N	amber99_81 (NT)	-0.593
12	H	amber99_17 (H)	0.269
13, 16	CA, CB	amber99_11 (CT)	- 0.086
14, 15, 17, 18	HA1, HA2, HB1, HB2	amber99_19 (H1)	0.124
19	N	amber99_81 (NT)	-0.150
20, 21	H1, H2	amber99_17 (H)	0.340
22, 25	CA , CB	amber99_11 (CT)	- 0.023
23, 24, 26, 27	HA1, HA2, HB1, HB2	amber99_19 (H1)	0.129
28	N	amber99_81 (NT)	-0.500
29	H	amber99_17 (H)	0.280
30	CA	amber99_11 (CT)	- 0.081
31, 32	HA1, HA2	amber99_19 (H1)	0.125
33	CB	amber99_11 (CT)	- 0.300
34, 35, 36	HB1, HB2, HB3	amber99_18 (HC)	0.117

TABLE 3.7: Coulombic parameters (q_i, see Equation (2.3)) for completely protonated PEI chain. See Figure 3.1(c) for atom numbers.

Atom No.	**Atom name**	**Atom type**	**Charge,** q_i
1	N	amber99_81 (NT)	- 0.417
2, 3, 4	H1, H2, H3	amber99_17 (H)	0.36
5	CA	amber99_11 (CT)	0.056
6, 7	HA1, HA2	amber99_19 (H1)	0.087
8	CB	amber99_11 (CT)	-0.147
9, 10	HB1, HB2	amber99_19 (H1)	0.127
11	N	amber99_81 (NT)	-0.150
12, 13	H1, H2	amber99_17 (H)	0.340
14, 17	CA, CB	amber99_11 (CT)	- 0.023
15, 16, 18, 19	HA1, HA2, HB1, HB2	amber99_19 (H1)	0.129
20	N	amber99_81 (NT)	-0.135
21, 22	H1, H2	amber99_17 (H)	0.331
23	CA	amber99_11 (CT)	- 0.067
24, 25	HA1, HA2	amber99_19 (H1)	0.120
26	CB	amber99_11 (CT)	- 0.314
27, 28, 29	HB1, HB2, HB3	amber99_18 (HC)	0.160

MD simulations were performed with time step of 1 fs for integrating equation of motion. Particle mesh Ewald [114] method was used for long range electrostatic interactions. The non-bonded potential energy cut-off was 1.2 nm. The simulations were carried out in NPT ensemble using velocity rescale algorithm [123] for thermostat with coupling constant of 0.1 ps and Berendsen barostat [122] for isotropic pressure control with coupling constant of 1 ps. The systems were simulated for 50 ns. The trajectories were recorded at every 2 ps. Last 40 ns of the production run was used for analysis. From the 50 ns trajectories of the un and all protonated PEI systems, frame near 47 ns was extracted in such a way so that the PEI chain was sufficiently inside the simulation box. These extracted frames further served as the input structures for the higher temperature (i.e., for 310 K, 320 K and 330 K) simulations for the un and all protonated systems. The higher temperature simulations were performed for 4 ns with NVT ensemble and the trajectories were recorded at 10 fs intervals. These trajectories were used for the calculation of dynamical properties of water molecules along the PEI backbone.

In addition to above systems, simulations of bulk amorphous polymeric systems of 80 chains of 20-mer and 25 chains of 50-mer PEI at 300 K were performed for 80 ns. The systems were prepared by using amorphous cell construction module of Material Studio [140] to guarantee conformationally lower energy chains in the simulation box. Though, the force field parameters were adopted from Ziebarth et al. [135] and the next neighbor nitrogen atoms (NN) and next to next neighbor nitrogen atoms (NNN) distributions for 20-mer single chain PEI in water were in agreement with their distributions, we have

also calculated the density of the bulk amorphous system from the long simulation. The variation of density as function of time (last 10 ns of the total 80 ns run) is reported in Figure 3.2. The density from the simulation for 20-mer and 50-mer PEI systems was 1.025 (± 0.002) g/cc and 1.031 (± 0.002) g/cc, respectively (Figure 3.2). The experimental density reported for the crystalline linear PEI is 1.14 g/cc. [141] The simulated densities are less than the experimental (for crystalline PEI) density, which is obvious because of the amorphous nature of the simulated PEI. However, the experimental density is close to the simulated amorphous PEI density.

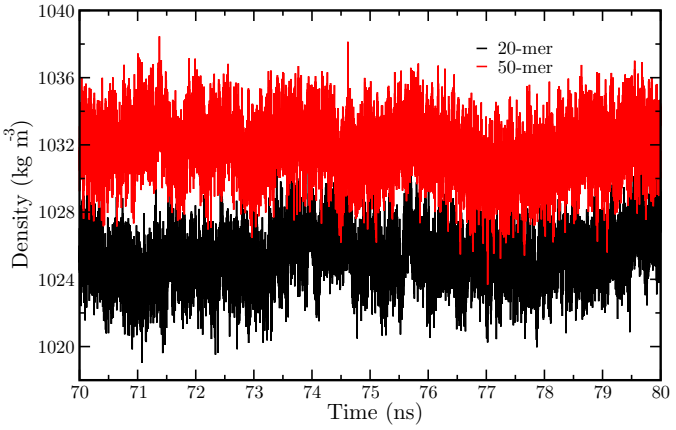

FIGURE 3.2: The variation of density of 20 and 50-mer PEI with time.

3.3 Results and discussions

3.3.1 Structural properties of polymer

3.3.1.1 NN and NNN distributions

The distance distributions of nearest neighbor (NN) and next-nearest neighbor (NNN) amine groups for the three different protonation states of 50-mer PEI are plotted in Figure 3.3. For the NN distribution, distance distribution was calculated from all NN (e.g., first - second, second - third, third - fourth and so on) distances between nitrogen atoms. Individual distributions for systems with three different protonation states were averaged and plotted in Figure 3.3(a). Similar individual distributions were computed for all NNN (first - third, second - fourth, third - fifth and so on) nitrogen atoms and are plotted in Figure 3.3(b). The maxima of the peaks for NN and NNN distributions of 50-mer were reproduced in agreement with the Ziebarth et al.'s study. [135] The peak maxima of NN distributions at $\sim$ 0.29 nm and $\sim$ 0.38 nm represent the *syn* and the *anti* conformations, respectively while the peaks at $\sim$ 0.57, $\sim$ 0.65 and $\sim$ 0.73 nm of

NNN plot corresponds to *syn-syn*, *syn-anti* and *anti-anti* conformations, respectively. These possible conformations are summarized and depicted in Table 3.8. In addition, 50-mer PEI has some extra peaks with fewer occurrences, which are representative of the intermediate conformations. All protonated chain mainly shows *anti* conformation for NN nitrogen atoms but for alternate and unprotonated chains both the *syn* and *anti* conformations are favorable (slightly favoring the *syn* conformation). NNN distributions are more complex for unprotonated system because of degeneracies between different conformations. However, all protonated system shows distinct conformational states. The conformations of the charged chains are such that they minimize the electrostatic repulsion. We have further investigated the conformation of the chains in detail later in this chapter.

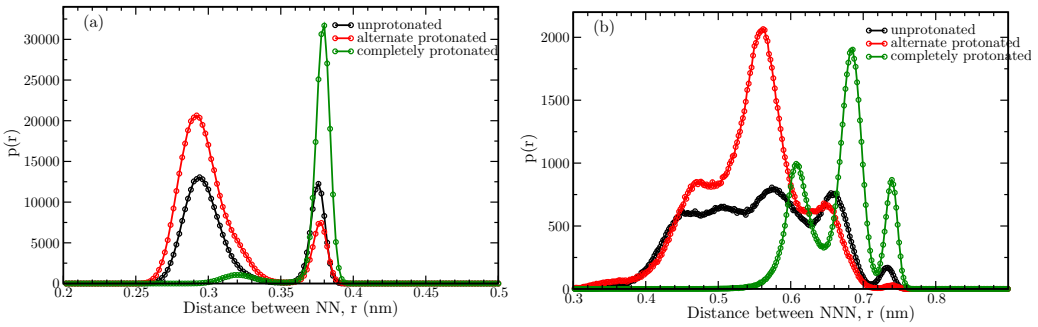

FIGURE 3.3: (a) NN and (b) NNN distributions of the nitrogen atoms for 50-mer PEI.

TABLE 3.8: Possible nearest neighbor (a, b) and next nearest neighbor (c, d and e) conformations for the PEI chain

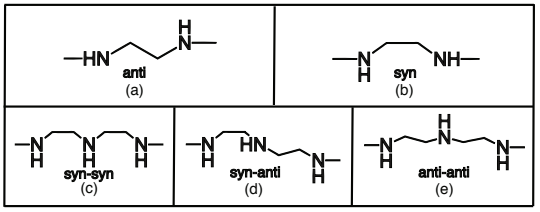

3.3.1.2 End-to-end distance and radius of gyration

The conformation and compactness of a polymer can be represented by end-to-end distance and radius of gyration (R_g). The end-to-end distance was calculated as the root mean square distance of the two ends of the polymer chain. R_g^2 was calculated as the average squared distance of every atom from the center of mass of the chain. The variation of end-to-end distance and its distribution for the un, alternate and all protonation states of 50-mer PEI are depicted in the Figures 3.4(a) and 3.4(b), respectively, while

Figures 3.4(c) and 3.4(d) shows R_g as a function of time and its distribution. The distributions were normalized by total number of frames. The end-to-end distances of the unprotonated chain stays almost below 3 nm up to 30 ns, then it increases to 7 nm and gets back to the smaller value at 40 ns, thereafter stays around 3 nm. Similarly, R_g stays around 1 nm for 30 ns and then it increases to 2 nm and further decreases to 1 nm after 40 ns. The distribution plots (Figures 3.4(b) and 3.4(d)) for the unprotonated system shows that the most probable end-to-end distance is $\sim$ 2 nm and R_g is $\sim$ 1 nm. Thus the smaller end-to-end distance and R_g indicates that the unprotonated polymer chain prefers to stay in the coiled form. This coiling of unprotonated systems is also reflected from the NN and NNN plots (Figure 3.3). For the all protonated system, end-to-end distance and R_g of PEI fluctuates around 7 nm and 2.75 nm, respectively. The distributions show that 8 nm and 2.6 nm are the most likely end-to-end distance and R_g. This suggests that the all protonated PEI is extended. The same is also observed by the NN and NNN plots (Figure 3.3) of the all protonated system. The end-to-end distance and R_g for all protonated system shows wider distributions around 5 nm and 7.5 to 8.5 nm for the end-to-end distance while 2.2 nm and 2.7 nm for the R_g. The average end-to-end distances and R_gs are tabulated in Table 3.9. It is clearly evident from Table 3.9 that the chain size increases with the increase in protonation level. As the level of protonation increases, polymer chain becomes more charged on the secondary amine sites. This leads to the repulsion between the monomeric units within the polymer chain that results into elongated structure. The polymer conformations at different protonation states, representing the averaged R_g (Table 3.9) are depicted in Figure 3.5.

TABLE 3.9: Average end-to-end distance (nm) and radius of gyration (R_g) (nm) for 50-mer PEI chain at different protonation states.

	unprotonated	alternate protonated	all protonated
end-to-end distance	3.25 ± 0.77	6.77 ± 1.34	8.45 ± 1.23
radius of gyration (R_g)	1.23 ± 0.12	2.41 ± 0.25	2.76 ± 0.18

3.3.1.3 Dihedral angle distribution

Dihedrals are more flexible than the other bonded interactions (bonds and angles). Therefore, dihedral orientations play a key role for a particular shape and size of the polymer chain. There are two dihedrals, N - C - C - N and C - C - N - C present in the backbone of linear PEI. These are responsible for different conformations of the polymer chain. We have calculated and plotted in Figure 3.6(b) the distribution of these dihedral angles for every protonation states of 50-mer PEI. The dihedral angle from +90° to -90° is represented as the *syn* conformation while -90° to -180° or 90° to 180° are represented as *anti* conformations. The N - C - C - N dihedral for the unprotonated chain, equally

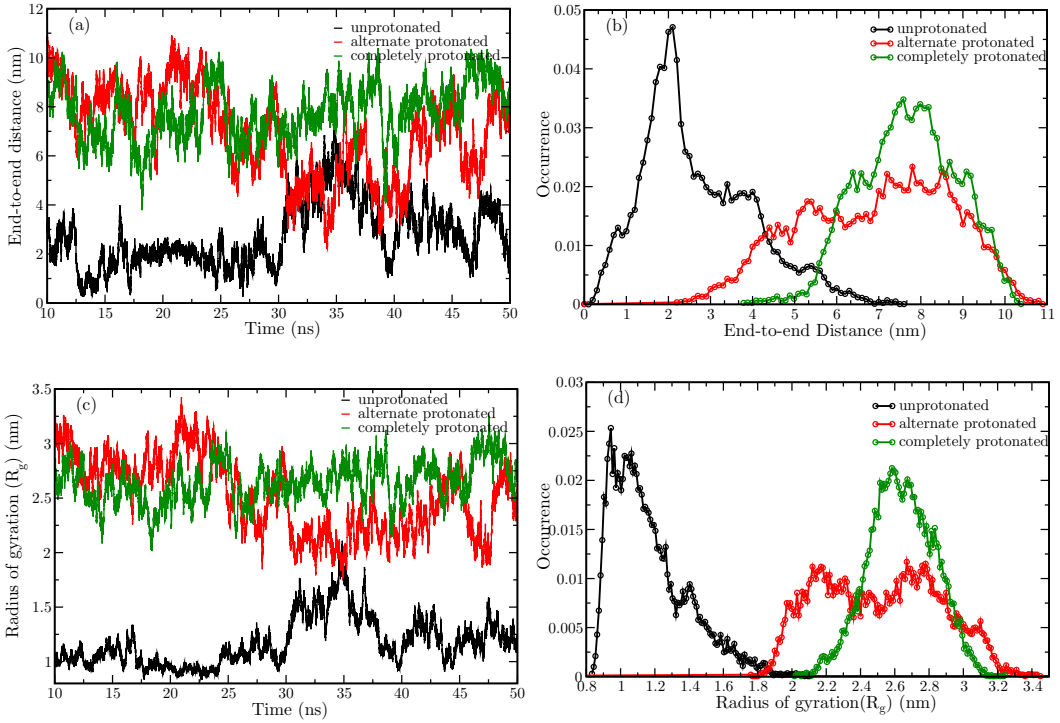

FIGURE 3.4: The (a) variation of end-to-end distance with time and (b) its distribution, (c) variation of radius of gyration, R_g, with time and (d) its distribution for 50-mer PEI chains.

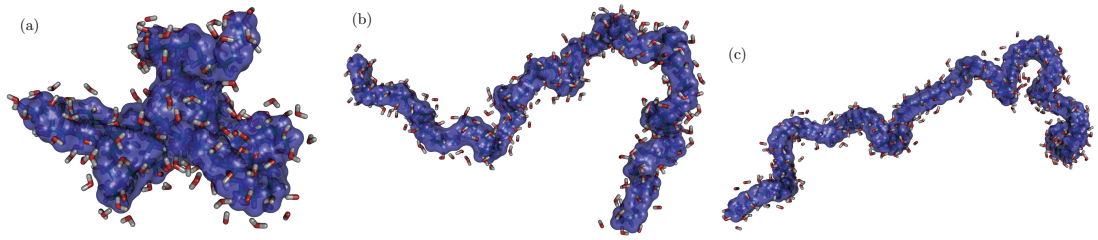

FIGURE 3.5: Shows the snapshots of 50-mer PEI chain which are representatives of R_g's tabulated in Table 3.9 for (a) Unprotonated state, (b) alternate protonated state and (c) all protonated state. The unprotonated chain is highly coiled. The blue region is the surface area of the polymer chain. Water molecules in the 1^{st} solvation shell are also shown for each protonation state.

scans both the *syn* and *anti* conformations while the C - C - N - C dihedral primarily scans the *anti* conformations.

The alternate protonated system's N - C - C - N dihedral of PEI mostly scans *syn* conformations while C - C - N - C dihedral scans *anti* conformations. The all protonated N - C - C - N dihedrals largely scans the *anti* conformation and the C - C - N - C dihedral samples both *syn* and *anti* conformations with a slight higher dominance for *anti* . Thus, the C - C - N - C dihedrals of un, alternate and all protonated systems, predominantly samples the *anti* conformation with less probability for the *syn* conformations. From

the dihedral distribution plot (Figure 3.6(b)) for all protonated system it is evident that both dihedrals (N - C - C - N and C - C - N - C), prominently have higher probability to stay at the *anti* conformation and this leads to the elongation of the chain, resulting in higher end-to-end distance and R_g, (see Figure 3.5(c)). The dihedrals of un and alternate protonated system sample both the conformations, giving rise to the wide distribution for end-to-end distance and R_g (Figure 3.4). For the 20-mer PEI systems, we have observed similar behavior and the plots are shown in Figure 3.6(a). These observations are further quantified and explained by calculating the ratio of *syn* to *anti* conformations.

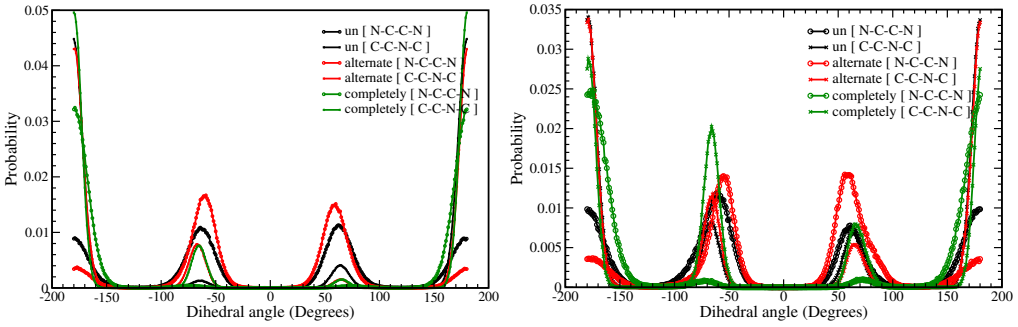

FIGURE 3.6: The distributions of N - C - C - N and C - C - N - C dihedrals for different protonation states are shown. Dihedral distribution for (a) 20-mer and (b) 50-mer PEI.

***Syn-anti* ratio** The torsional angle between 0° to ±90° represents the *syn* conformations while -90° to -180° or 90° to 180° represents *anti*. Using this condition for each frame of the production run trajectories, the total number of *syn* and *anti* conformations were recorded and then their ratios (*syn*/*anti*) were computed for 50-mer and 20-mer PEI systems. For 50-mer systems, Figure 3.7(a) shows the distribution of ratios for all three systems when all dihedrals were considered. Figure 3.7(b) shows the distribution of ratios where only N - C - C - N dihedrals were considered and Figure 3.7(c) shows the distribution of ratios only for C - C - N - C dihedrals. The distributions were normalized by the total number of frames. Ratio greater than 1 implies *syn* predominance while less than 1 favors *anti* conformations.

For the unprotonated system, *syn* to *anti* ratio for N - C - C - N dihedral (Figure 3.7(b)) is mostly greater than 1 (peak at ~ 1.7), which shows there is a slight dominance of *syn* conformations. NN is the distance between the neighboring N of the amine groups while dihedral N - C - C - N is the dihedral angle between these groups. Thus the trend in the distribution of N - C - C - N dihedral angles should also be reflected on NN distribution. NN distribution plot for unprotonated chain (Figure 3.3(a)) has higher peak height at ~ 0.29 nm which is the outcome of predominance of *syn* conformations and smaller peak height at ~ 0.38 nm due to less occurring *anti* conformations. The similar observation is also revealed from the *syn* to *anti* ratio. For C - C - N - C dihedrals (Figure 3.7(c)),

the distribution of ratios has peak around 0.6 that suggests the dominance of *anti* conformations. However, when we consider all the dihedrals (Figure 3.7(a)) the peak maxima spans over 0.75 to 0.9. The distribution of all dihedrals shows the dominance of *anti* conformations. Therefore, overall the unprotonated PEI structure is dominated by *anti* conformations.

The *anti* conformation is favored for all protonated PEI chain, as the distribution of *syn* to *anti* ratio for N - C - C - N (Figure 3.7(b)) and N - C - C - N and C - C - N - C dihedrals (Figure 3.7(a)) is less than 0.9. The favorable *anti* conformation of N - C - C - N dihedral can also be inferred from the NN distance distribution (Figure 3.3(a)) which shows a prominent peak at $\sim$ 0.38 nm, related to *anti* conformation. However, the C - C - N - C dihedrals for all protonated PEI shows (Figure 3.7(c)) almost equal frequency of both *anti* and *syn* (peak at $\sim$ 1 to 1.15) but with slightly higher dominance of *syn* conformations (ratio distribution peaks at 1.1). On comparing the distributions of ratio for the un and all protonated system, we note that when N - C - C - N (Figure 3.7(b)) and all (Figure 3.7(a)) dihedrals are considered, the all protonated system has higher *anti* conformations which leads to greater end-to-end distances and R_g than unprotonated system.

From NN distance distribution (Figure 3.3(a)) of the alternate protonated system, it is clearly evident that the *syn* conformations dominate over the *anti*. The distribution of ratio for *syn*/*anti* for N - C - C - N and all dihedrals depicted in Figure 3.7(b) and Figure 3.7(a), respectively shows the overall *syn* dominance. The peak of N - C - C - N distribution of ratios at 4 implies that 79.6 % (i.e., 39 of 49 dihedrals) of dihedrals are *syn* while 20.4 % (i.e., 10 of 49 dihedrals) are *anti* . However, C - C - N - C dihedral shows preference for *anti* conformation for alternate protonated system (Figure 3.7(c)). Overall, the alternate protonated system has higher *syn* conformations than the unprotonated. But, still the unprotonated system is more coiled when we compare the end-to-end and R_g (Table 3.9). So, to address this issue we have calculated the alternate *syn* and *anti* dihedral occurrences along the polymer chain.

Alternate *syn-anti* dihedral occurrence There are 147 dihedral angles (when all dihedral angles are considered) along the backbone for a 50-mer PEI chain. We searched for the neighboring dihedrals having a mismatch in the conformations (i.e., *syn-anti* or *anti-syn* pairs). Such pairs were calculated and plotted in Figure 3.7(d). The plot was normalized by the total number of frames. The greater the number of mismatches in the neighboring dihedrals, more coiled is the polymer chain. We see that the unprotonated chain has higher number of mismatch (with less occurrence). The all protonated PEI has less number of mismatches. Interestingly the alternate protonated chain has the

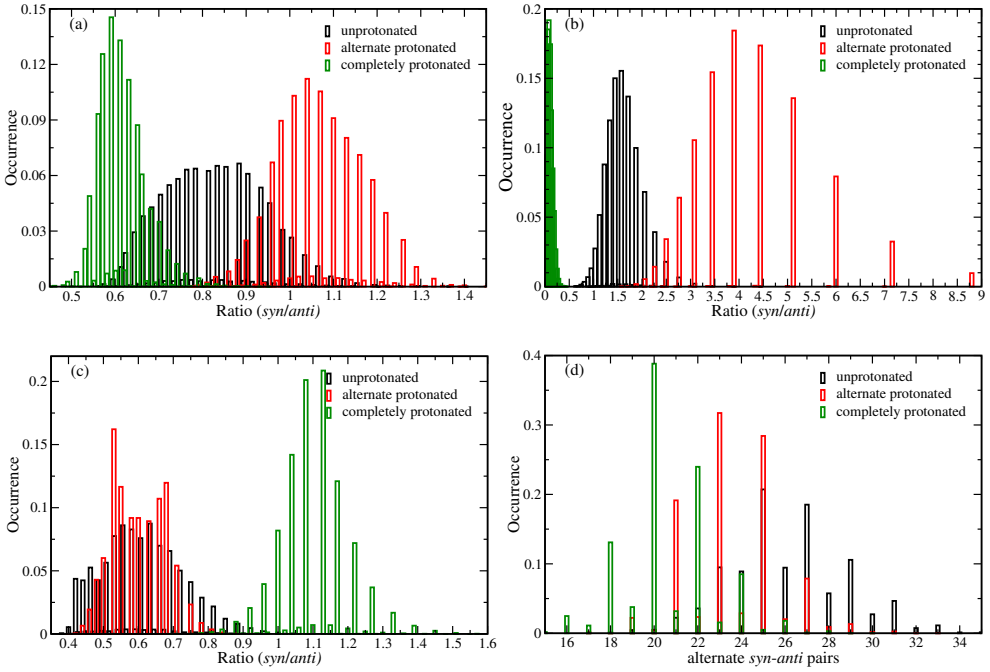

FIGURE 3.7: Distribution for the ratio of *syn* to *anti* dihedrals when (a) all dihedrals (b) only N - C - C - N dihedrals and (c) only C - C - N - C dihedrals were considered. (d) Alternate *syn-anti* pair occurrences of all dihedrals for 50-mer PEI.

number of pairs of *syn-anti* (or *anti-syn*) in between un and all protonated system but has fairly large frequency of this count. Thus, the higher number of alternate *syn-anti* (mismatches) pairs for the unprotonated justifies the fact that it is more coiled than the alternate protonated chain. Similar *syn* to *anti* ratio and alternate *syn-anti* ratio were calculated and plotted for the 20-mer PEI system and are reported in Figure 3.8.

3.3.2 Arrangement of water molecules around the PEI chain

3.3.2.1 Pair distributions

Pair distribution of particles gives the probability of finding a particle at a distance, r, from another particle. It is helpful in describing the local structure of a chemical moiety. Here we have analyzed the arrangement of water molecules around the PEI chain and depicted it in Figure 3.10 for 50-mer PEI and Figure 3.9 for 20-mer.

Pair distributions between the N-atoms (hydrophilic atoms) of PEI chain and the oxygen (O) atoms of water molecules for different protonation states are plotted in Figure 3.10(a). The plot shows two prominent peaks indicating two solvation shells around the N atoms. The height of the peaks increases with the increase in the level of protonation. All protonated chain has a sharp first peak with greater height indicating higher amount of water molecules around the N atoms. This is may be because of the positively

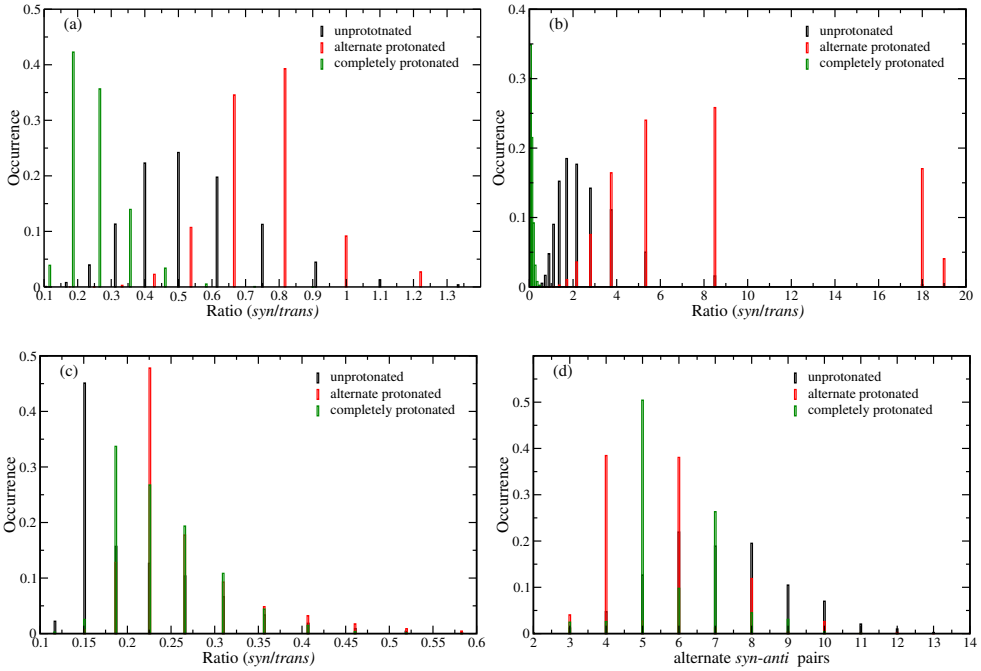

FIGURE 3.8: Distribution of ratio (*syn/anti*) when (a) all, (b) N-C-C-N and (c) C-C-N-C dihedrals were considered. (d) Alternate *syn-anti* occurrences of all the dihedrals for 20-mer PEI.

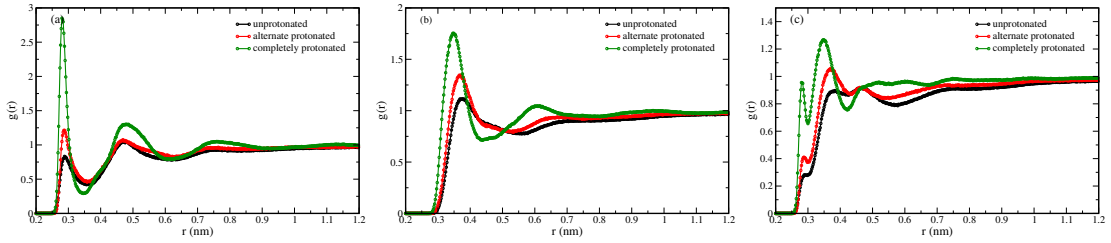

FIGURE 3.9: The pair distribution plot of (a) N of PEI and O of Water, (b) C of PEI and O of Water and (c) N and C of PEI and O of Water for 20-mer PEI.

charged amine groups of PEI chain that causes higher electrostatic attractions with water molecules and hence increases the number of water molecules in the first solvation shell as compared to the other states.

The pair distribution of hydrophobic atoms along the polymer backbone (C atoms) and O of water molecules are reported in Figure 3.10(b). The peaks are broader than the N - O atom's pair distribution (Figure 3.10(a)) and are shifted to higher distance. However, as similar to N - O case, the peak height increases with the increase in level of protonation. This can be attributed to the increase in electrostatic interactions (because of protonation level) of the PEI chain that influences the hydrophobic environment of C atoms. The number of water molecules in the first solvation shell for alternate protonated system is higher than unprotonated state but less than all protonated state.

The pair distribution plot for all backbone atoms (N and C) of PEI with O (water) atoms (Figure 3.10(c)) shows increase in peak height for the first and second solvation shell with the increase in protonation level. This implies that the water molecules around the chains are ordered and the ordering increases with the level of protonation. The peak minima for first and second solvation shells for the backbone atoms (Figure 3.10(c)) are at ~ 0.30 nm and ~ 0.42 nm, respectively. The first solvation shell of N has larger number of water molecules than that of N and C combined. This is because of the merging of hydrophilic and hydrophobic solvation shells. It can be noted from the pair distribution (of N - O), the first minimum of hydrophilic solvation shell is at 0.35 nm whereas the hydrophobic solvation shell starts at 0.30 nm. So, there are regions near C atoms (C atoms are double in number than N atoms in the polymer backbone) which are less filled with water compared to N atoms and thus it contributes negatively to the number of water molecules present in the solvation shell of the polymer backbone atoms.

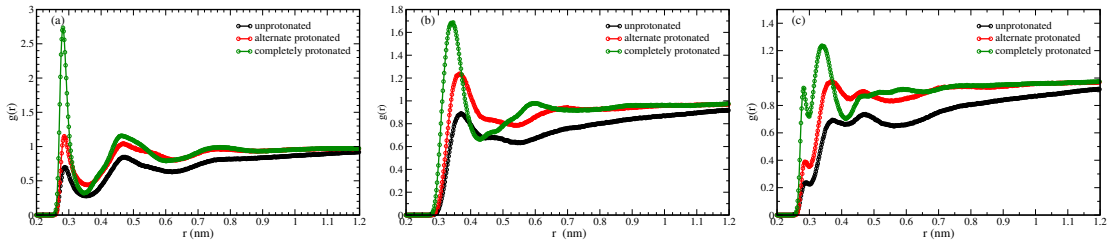

FIGURE 3.10: The pair distribution plots for 50-mer PEI between (a) N of PEI and O of Water, (b) C of PEI and O of Water and (c) N and C of PEI and O of Water.

3.3.2.2 Solvation shells of backbone monomers

We have used the first minima of pair distribution plots to find the number of water molecules present in each of the solvation shells. For all and unprotonated polymer chains the minima of first peak (i.e., end of first solvation shell) are at 0.30 nm (Figure 3.10(c)) when all backbone atoms are considered. We have used this distance (0.30 nm) as the cutoff to calculate the number of water molecules around the PEI chain and depicted in Figure 3.11. Last 3 ns of the condensed trajectory (refer computational details) were used for this calculation. We discarded all the double count because of overlap of a solvation shells within the cutoff. The plot was normalized by total number of monomers. Figures 3.5(a) and 3.5(c) show the conformation of polymer and arrangement of water molecules along the first solvation shell of the un and all protonated PEI, respectively. Similarly, for second solvation shell we have considered the water molecules residing at distances between 0.30 nm to 0.42 nm (between the minima of first and second peaks in Figure 3.10(c)) from the PEI backbone atoms. The number of water molecules per

monomer along the polymer backbone for first and second solvation shells as a function of time is shown in Figure 3.11 and its averages are tabulated in Table 3.10. The unprotonated chain has less number of water molecules in its first solvation shell ~ 0.55 per monomer while the all protonated system has ~ 2.12 per monomer, around 4 times more than unprotonated PEI. Because of hydrophobic backbone and less electrostatic interactions there is less number of water molecules near the unprotonated chain. However, in case of all protonated system due to protonation on the N atom, the hydrophilicity increases that cause higher water count in the solvation shells. Similarly the second solvation shell has a considerable increase (~ 1.5 times) in number of water molecules from un to all protonated level but the magnitude is less than the first solvation shell.

TABLE 3.10: Number of water molecules per monomer along the polymer backbone for solvation shells of un and all protonated PEI.

	unprotonated	all protonated
1^{st} solvation shell	0.55 ± 0.07	2.12 ± 0.12
2^{nd} solvation shell	3.71 ± 0.24	5.44 ± 0.20

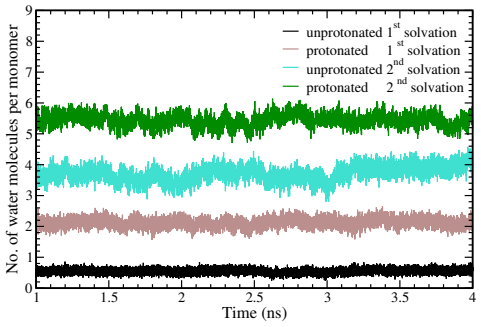

FIGURE 3.11: Number of water molecules along the polymer backbone for the 1^{st} and 2^{nd} solvation shells.

3.3.3 Dynamical properties

3.3.3.1 Residence time of water molecules

Residence time of a particle is defined as the amount of uninterrupted time the particle stays in a specified state. Computationally, the definition for calculating the residence time of water molecules along an ion was suggested by Impey et al. [142] According to them, the residence time (t) of a water molecule in the first solvation shell is the time it stays in the shell without leaving the shell for more than t^* where $t^* = 2$ ps. In our study we have incorporated the same definition for the calculation of residence time of water molecules along the polymer backbone for the first solvation shell (within the radius of 0.30 nm from the polymer backbone) and for the second solvation shell (between 0.30 nm and 0.42 nm) (see Figure 3.10(c)). This distance cut-offs are from the

polymer backbone including both hydrophilic and hydrophobic atoms. The last 3 ns of the condensed trajectories (refer computational details) of the un and all protonated PEI systems of 50 mer were used to calculate the residence time of water molecules for both the solvation shells. These 3 ns trajectories for all the systems were split in 3 parts with 1 ns each for averaging. For every frame, in each of the systems, unique (avoiding double count) water molecules in the solvation shells were recorded. These water molecules were tracked for the subsequent times (frames) and the time when it was not found for more than 2 ps, the time up to which it was continuously found was recorded as the residence time. It may also happen that a water molecule may become part of the solvation shell after leaving the shell for atleast 2 ps. All such incidences were taken as distinct occurrences. For every water molecules initially the residence times were 0. The residence time increases on finding the same water molecule in the succeeding time steps (until continuously not found for more than 2 ps). The average residence time distribution as a function of time is depicted in Figure 3.12 at 300 K for protonated and unprotonated systems and for first and second solvation shells. The total count of water molecules at 0 ps was used to normalize the residence time distribution plot. As the distribution plots are exponentially decaying, we have fitted these residence time distributions with a biexponential function (Equation (3.2)) where a_f and a_s are the amplitudes of the fast and slow relaxation components with relaxation times τ_f and τ_s respectively.

$$y = a_f e^{-t/\tau_f} + a_s e^{-t/\tau_s} + a_0 \tag{3.2}$$

The values for a_f, τ_f, a_s and τ_s of the water molecules in the first and second solvation shells obtained by fitting Equation (3.2) to Figure 3.12 are tabulated in Table 3.11. Figure 3.12 shows two distinct slopes one fast and another slow decaying. The fast decaying component is represented by τ_f while τ_s represents the slow component. As reported by Bakker et al. [143], in liquid water there exists two distinct molecular species one with fast relaxation and another with slow. Slow relaxation (orientational relaxation) is attributed to the strongly bonded hydrogen bonds, which only relaxes via the slow process. Thus, the structural reorganization of the hydrogen bonding networks via rotation or translation of water molecules is connected to this slow relaxation times. [144] The single molecule reorientation (the proton motion) is characteristic of the fast orientational relaxation.

From Equation (3.2), it is evident that higher the value of τ_s or τ_f, slower is the relaxation time and hence the dynamics will be slow. For the first solvation shell, τ_f component increases from 0.11 ps to 0.18 ps on moving from un to all protonated system while the slow relaxing component, τ_s increases from 2.41 ps to 4.41 ps (Table 3.11). Thus, we observe for the first solvation shell of the protonated system τ_s and τ_f are higher than

TABLE 3.11: Residence time of water molecules at 300 K for different solvation shells of un and all protonated PEI. a_f, a_s are respective, amplitudes of the fast and slow components with relaxation times τ_f and τ_s (see Equation (3.2)). These components were obtained by fitting each of the plots of Figure 3.12 with Equation (3.2). For each of the fit R^2 were > 0.99.

		a_f	τ_f (ps)	a_s	τ_s (ps)
Unprotonated	1^{st} solvation shell	0.95	0.11	0.13	2.41
	2^{nd} solvation shell	0.69	0.27	0.33	6.75
All protonated	1^{st} solvation shell	0.84	0.18	0.20	4.41
	2^{nd} solvation shell	0.93	0.11	0.14	3.12

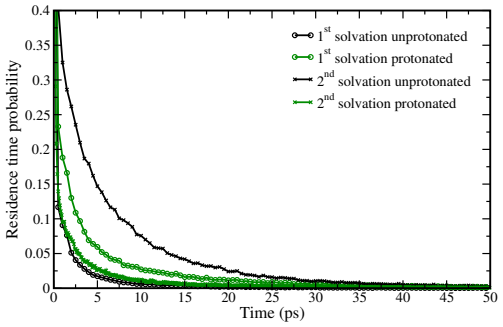

FIGURE 3.12: Residence time probability of water molecules at 300 K. Black lines shows the residence time probability of the unprotonated PEI while the green lines are for the all protonated polymer. The filled circles denote the 1^{st} solvation shell while crosses represents the 2^{nd} solvation shell.

the unprotonated system i.e., it has slower dynamics. This observation can be attributed to the higher interactions between the water and the PEI chain for all protonated system i.e., stronger hydrogen bonding network in the system. For the second solvation shell, τ_f component of the unprotonated system is 0.27 ps which is higher than the all protonated system (0.11 ps). This is may be because of inward pull towards the protonated groups of PEI chain, which is absent in case of unprotonated system. This inward pull leads to the faster motion (smaller τ_f) of the water molecules in second solvation shell to jump into the much favorable tetrahedral like configuration to form stronger H-bond in the first solvation shell. [144, 145] τ_s for second solvation shell decreases from 6.75 ps to 3.12 ps on moving from un to all protonated system. The second solvation shell of unprotonated system has τ_s of 6.75 ps which is much more water like ($\tau_{s\ H_2O(l)} \sim 8$ ps [144]). But for the all protonated system, there exists an attraction of the water molecules of the second solvation shell towards PEI. This leads to the faster dynamic which is reflected also in τ_s values (Table 3.11). Similar residence time distributions for the water molecules in the first and second solvation shells at higher temperatures viz., 310 K, 320 K and 330 K are reported in Figure 3.13. In liquid water, the water molecules hops from occupied to an unoccupied corner of the cube in $(H_2O)_5$ tetrahedron. This tetrahedral displacement regulates the mechanism of τ_s and this mechanism also govern the self-diffusion of water. [146] In the next section we discuss the self-diffusion of water

molecules along the polymer backbone and factors governing it.

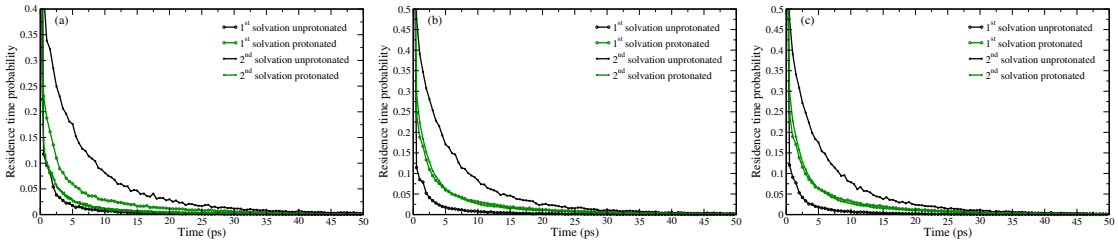

FIGURE 3.13: Residence time probability of the water molecules in different solvation shells of the polymer chain (50-mer) at (a) 310 K (b) 320 K and (c) 330 K.

3.3.3.2 Self-diffusion of water molecules around polymer chain

Self-diffusion coefficients were calculated for the water molecules present in the first and second solvation shell (as defined above) along the PEI chain for the un and all protonated system. The self-diffusion coefficients, D, were computed using the Einstein relation as in Equation (3.3) by following the mean square displacement (msd) of water molecules as a function of time.

$$D = \lim_{t\to\infty} \frac{1}{6t} < |r_i(t) - r_i(0)|^2 > \tag{3.3}$$

From the residence time plot (Figure 3.12) of the water molecules of the solvation shells, 20 ps was considered as the minimum time for which a water molecule should reside for calculating the msd. The minimum stay time of 20 ps for the water molecules also incorporates the soft boundary of t^*= 2 ps. A water molecule can continuously stay for 20 ps more than once i.e., if a water molecule continuously stayed for 20 ps or more (in a solvation shell) may leave the shell for time greater than 2 ps and can again enter or be the part of shell for another 20 ps or more. All such incidences were taken as distinct occurrences and contributed to the msd. The initial time for individual water molecules (residing for minimum of 20 ps) may vary and were taken as 0^{th} time. For calculating the msd, the last 1 ns of condensed 4 ns trajectories were used. These 1 ns trajectories were split in two parts with 500 ps each for better statistics. For each trajectory, the msd as a function of time were computed. These plots were then averaged. For 300 K, the evolution of msd as a function of time is depicted in Figure 3.14. Figures 3.14(a) and 3.14(b) shows the msd plots for first and second solvation shells, respectively. The water molecules in the first solvation shell of all protonated chain move faster than the unprotonated chain. However, in case of second solvation shell the observation is opposite. Since the calculation of msd (and diffusion constant from this msd plots) is only for the water molecules which are residing for minimum 20 ps in the solvation shells of

PEI backbone atoms, we term this self-diffusion coefficient as the effective self-diffusion coefficient, D_{eff}.

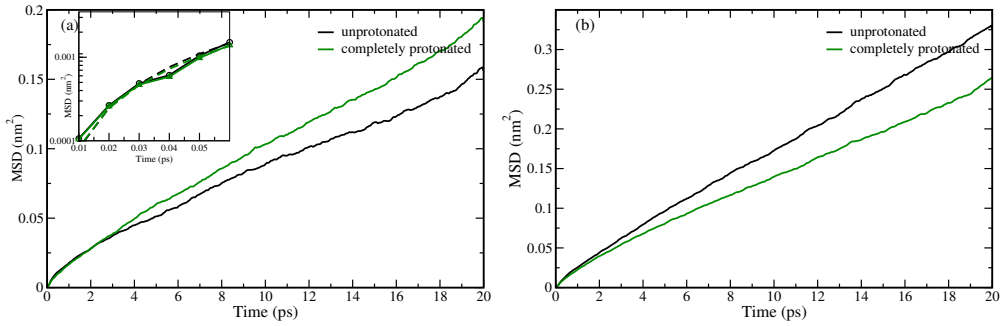

FIGURE 3.14: Mean Square Displacement of water molecules for the 50-mer PEI at 300 K for (a) 1^{st} solvation shell and (b) 2^{nd} solvation shell. Inset (of Figure 3.14(a)) shows the semi-log plot of the msd of water molecules in the sub-picosecond time. Dotted lines (in inset) were fitted to Equation (3.4).

The effective self-diffusion and slow relaxation time are governed by the elementary mechanism of tetrahedral displacement. [146] The second solvation shell of the unprotonated system has higher value of τ_s (6.75 ps, Table 3.11). Therefore, these water molecules behave much more like the liquid water and thus it has higher effective self-diffusion coefficient (at 300 K) ($D_{eff} = 2.65 \times 10^{-5}$ cm^{2}s^{-1}, Table 3.12). Effective self-diffusion coefficient ($D_{eff} = 1.16 \times 10^{-5}$ cm^{2}s^{-1}, Table 3.12) is the lowest for first solvation shell of unprotonated system and same is true for τ_s. For all protonated system, there is a tendency of water molecules of second solvation shell to move towards PEI due to the higher electrostatic attractions between the charged amine groups and the water molecules. This electrostatic interactions acts as s driving force which overrides the mechanism of tetrahedral displacement and thus the second solvation shell has higher effective diffusion coefficient ($D_{eff} = 2.03 \times 10^{-5}$ cm^{2}s^{-1}) than first solvation shell ($D_{eff} = 1.48 \times 10^{-5}$ cm^{2}s^{-1}). The msd of water molecules in the first and second solvation shells at higher temperatures viz., 310 K, 320 K and 330 K are reported in Figure 3.15. The effective diffusion coefficient for every solvation shells is tabulated in Table 3.12 and it increases with the increase in temperature owing to the greater movement of water molecules on increasing the temperature.

TABLE 3.12: Effective self-diffusion coefficients, D_{eff}, 10^{-5} cm^{2}s^{-1}, of different solvation shells at each of the simulated temperature, computed from the slopes of Figure 3.15.

		300 K	310 K	320 K	330 K
Unprotonated	1^{st} solvation shell	1.16	1.27	1.47	1.49
	2^{nd} solvation shell	2.65	2.88	3.17	3.41
All protonated	1^{st} solvation shell	1.48	1.60	1.72	2.01
	2^{nd} solvation shell	2.03	2.25	2.39	2.75

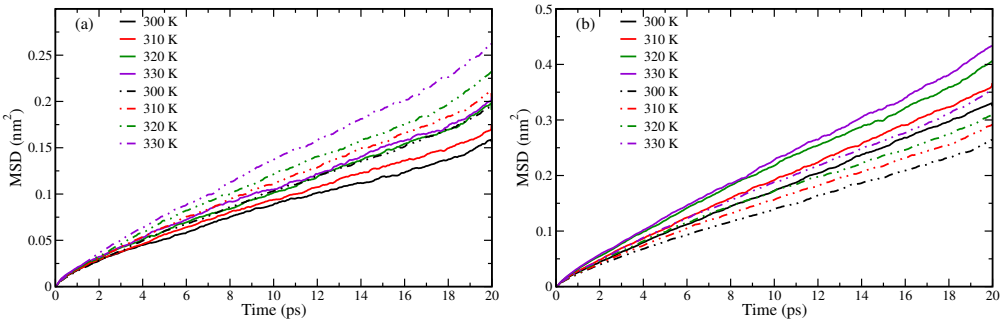

FIGURE 3.15: Mean square displacement of water molecules around the (a) 1^{st} solvation shell and (b) 2^{nd} solvation shell at different temperatures for unprotonated (solid lines) and protonated (dotted - dashed lines) states of 50-mer PEI.

For protonated polymer water molecules reside longer (both τ_f and τ_s are higher than the unprotonated case) in the first shell and the effective self-diffusion of water molecules are faster than the unprotonated case. We may attribute to the fact that protonated chains are elongated and water molecules can move along faster than the coiled unprotonated chain. Inset of Figure 3.14(a) shows the semi-log plot of the msd at sub-picosecond scale that has been fitted to Equation (3.4). The value a_1, in Equation (3.4), defines the type of diffusion possessed by the water molecules. The value of 0.5, 1 and 2 of $a_1$represents single-file, Fickian and ballistic diffusions, respectively. [147]

$$dr^2 = a_0\, t^{a_1} \tag{3.4}$$

For the un and all protonated system at 300K, a_1 is 1.65 and 1.60, respectively, suggesting a diffusion mechanism between Fickian and ballistic, in the sub-picosecond time scale for the first solvation shell.

To understand whether the water molecules of the first solvation shell diffuse along the chain or jump to the solvation shell of another atom, we have traced the path of the water molecules. We have considered those water molecules that satisfied the minimum residence of 20 ps (with soft boundary of 2 ps, as explained above) in the first solvation shell. These water molecules were paired to the nearest N-atom of PEI. Water molecules (satisfying the residence criteria) were paired in every frame. If it changed the pair (i.e., comes closer to the another N-atom), then the distance was computed between the N-atom of previous pair and the new pair. These distances were computed for every water molecule in the first solvation shell of un and all protonated systems from the last 500 ps of condensed trajectories. Among these distances, those water molecules that moved to the immediate solvation shell of the neighboring N-atom along the PEI chain were denoted as $d1$ otherwise marked as $d2$. The distributions of such distances are plotted in Figure 3.16(a) for unprotonated and Figure 3.16(b) for all protonated systems. The

total number of water molecules (satisfying the residence criteria) in the first solvation shell was used to normalize the plots. It is quite obvious that water molecules will predominantly change its solvation shell with the nearest neighbors. As expected, for both the systems $d1$ is more probable than $d2$. Thus, the movement of water molecules from its solvation shell to the immediate neighboring solvation shell is more probable. $d2$ is significant for the unprotonated system, Figure 3.16(a), which implies that the exchange of water molecules from one solvation shell to the neighboring shell (which are not immediate neighbors) is greater for unprotonated PEI than protonated PEI system. Protonated PEI chain is elongated so water molecules only see the solvation shells of immediate neighbors. However, unprotonated PEI chain is highly coiled (see Figure 3.5), which helps water molecules to see the solvation shells of nitrogen atoms that are not only the immediate neighbors but also are spatially very close (neighbor). So the motion of the water molecules for all protonated PEI chain is along the chain and for the unprotonated chain both type of motions i.e., along the chain and jumps to spatially neighboring solvation shells is possible. We have also observed the frequent rattling motion of water molecules between the neighboring solvation shells.

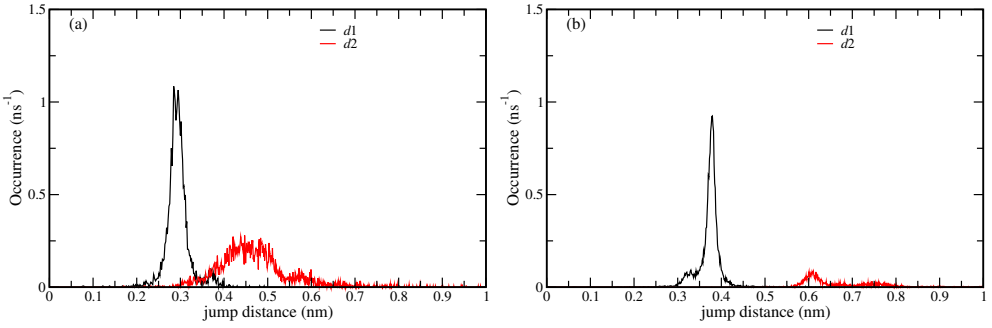

FIGURE 3.16: Shows the motion of the water molecules residing in 1^{st} solvation shell of 50-mer PEI. $d1$ are the jumps of water molecules to the solvation shell of the successive N-atom along the chain while $d2$ are the jumps to the spatially neighboring solvation shell (excluding $d1$) for (a) unprotonated PEI chain and (b) all protonated chain.

Activation energy The diffusion coefficient follows an Arrhenius relation with temperature, T (Equation (3.5), where E_a is the activation energy for diffusion).

$$D(T) = D_0\, e^{-E_a/RT} \tag{3.5}$$

The natural logarithm of diffusion coefficients, $D(T)$ as a function of $1/T$ for water molecules of first and second solvation shells for the un and all protonated systems are shown in Figure 3.17. Each of these plots were fitted to a straight line and from the slope, activation energy barrier, E_a, were computed and reported in Table 3.13. TIP3P water model's E_a is 2.45 kcal mol^{-1} while the experimental [148, 149] value is 4.58 kcal mol^{-1}.

TIP3P model underestimates activation energy. Activation energy corresponds to the energy of hydrogen bond and the average number of hydrogen bonds attached to each water molecule. [149] Thus, lower E_a for a solvation shell indicates lower strength or less number of hydrogen bonds within the solvation shell. Among the studied systems, first solvation shell of all protonated system has highest E_a, $1.93\,\mathrm{kcal\,mol^{-1}}$. The all protonated system being highly charged, as all the nitrogen atoms are protonated has high activation energy, so the water molecules posses higher number of hydrogen bonds with greater strength. For each of the solvation shells, the activation energies were less than that of the TIP3P water model.

TABLE 3.13: Activation energy barrier, $E_a, kcal\ mol^{-1}$, for different solvation shells of un and all protonated PEI. E_a for the TIP3P water and its experimental values are also tabulated. E_a's were computed from the slope of plots in Figure 3.17.

System		E_a, $kcal\ mol^{-1}$
Unprotonated	1^{st} solvation shell	1.81
	2^{nd} solvation shell	1.69
All protonated	1^{st} solvation shell	1.93
	2^{nd} solvation shell	1.90
Water (TIP3P)		2.45
Water (expt.) [148]		4.58

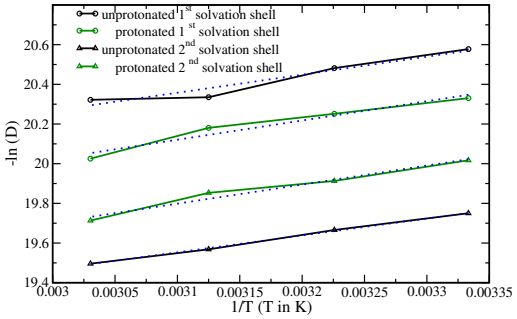

FIGURE 3.17: Natural logarithm of effective self-diffusion coefficient, D_{eff}, vs. $1/T$ of different solvation shells for un and all protonated states of PEI. Dotted lines are fitted to the equation of straight line.

3.4 Conclusions

In this chapter, we have investigated the structural and dynamical properties of linear PEI in explicit water at different protonation states of PEI. Two different chain lengths, 20-mer and 50-mer, of PEI were simulated. As the systems consisted of single chain, the results are well representative for PEI at dilute concentrations. The polymer conformation and the solvation dynamics have been studied in presence of water (TIP3P water model only) as a solvent. The results will not change much if we use different water models; of

course, an extensive study is required for the quantitative estimation, which is beyond the scope of this chapter.

The PEI chain elongates on increasing the protonation level, which is inferred from the increase in radius of gyration and end-to-end distances. On increasing the protonation level, i.e., moving from un to alternate to all protonated system, there is a steady increase in the electrostatic interactions. This causes repulsion among the monomeric units and to minimize the interactions, PEI chain elongates. We have correlated these phenomena with the distributions of dihedral angles of the polymer chain. The all protonated PEI chain prefers *anti* conformations for all its dihedral angles. The unprotonated chain has higher alternate *syn-anti* pairs than the alternate protonated chain.

Local structuring of water near PEI chain i.e. in the solvation shells for backbone atoms was analyzed by calculating pair distribution functions. Number of water molecules in the first solvation shell increase with the increase in protonation level which suggest that the all protonated system has larger amount of water along the polymer backbone than unprotonated system. Because of elongation the protonated PEI chain also can accommodate more water molecules, whereas, the unprotonated PEI shares solvation shells from its neighbors. This fact can be justified as the all protonated chain has large number of water molecules for both the solvation shells, the attraction toward the surfactant molecules get shielded while for the unprotonated system the shielding is less so the surfactant molecules can come closer to the PEI chain and facilitate aggregation.

Water molecules in the first and second solvation shells were further analyzed to understand their dynamics around the PEI chain. Residence time for water molecules around the chain was calculated which showed that there are two distinct types of water molecules with slow and fast relaxation in the solvation shells. The water molecules of first solvation shell of the protonated system (as compared to unprotonated system) experience higher attractive attractions towards the chain with strong H-bonding network, which retard its dynamics. For the second solvation shell, the water molecules of the all protonated system feel an inward pull towards the first solvation shell due to the additional electrostatic interactions. This leads to the faster motion of the water molecules to jump into the favorable conformations to form stronger H-bond in the first solvation shell. In addition, the diffusion of water molecules in the first solvation shell is slower than the second solvation shell. The water molecules of the first solvation shell of unprotonated system diffuse slowly than that of the all protonated system. The motion of these water molecules for all protonated PEI system is along the chain. In case of unprotonated chain the water molecules move along the chain and also jump to spatially neighboring solvation (not the nearest neighbors) shells of nearby N-atom. The second solvation shell of unprotonated system has the lowest activation barrier for the

self-diffusion of water molecules while the first solvation of all protonated system has the highest activation barrier.

All the studied systems were neutral and the effect of counter ions has not been studied in the present article. The reason behind this was all protonated systems were simulated with only 50 counter ions to neutralize the system. Thus the study of the effect of counter ion in this case would be statistically very poor. One way to check the effect of ions on the polymer conformations and solvation dynamics would be to add salt to it. [150] The simulations of these systems with added extra salt ions will be computationally expensive, as the ions have to be treated explicitly and need longer time scales to equilibrate the system. Thus the effect of counter ions possibly can be checked by treating PEI and water molecules as coarse-grained beads [151, 152] by evaluating coarse grained potentials. However, we may predict that on adding salt in the PEI-water system, at lower pH where PEI chain is protonated, the oppositely charged ions will be distributed around the polymer chain. [150]

PEI is well known polymer used as gene delivery agent. This chapter has future objective to eventually relate to the atomistic level understanding to the functional properties of PEI. In gene delivery PEI complexes with DNA and provides a stable environment in respect to the degradation by the enzyme. It may provide a physical barrier to the enzyme by which enzyme cannot reach DNA and/or the electrostatic interactions between the PEI and the enzyme prevent the enzyme to reach DNA. DNA coupled with PEI enters the cell through endocytosis, here, PEI protects DNA from lysosomal nucleases. PEI gets protonated due the low pH at lysosomes. This results in the influx of chloride ions and leads to the osmotic swelling of the endosomes. At the very same time, due to protonation, PEI expands its polymeric network. Both processes, the swelling of endosomes and the elongation of PEI leads to the bursting of the endosomes. This protects DNA to get degraded from the degradative lysosomal trafficking pathway and DNA gets introduced. This ability of PEI vectors to avoid the acidic lysosomes increases its transfection efficiency. [30] At very low pH, we can expect the N-atoms getting protonated leading to the elongation of polymer and simultaneously, causing the endosomes to swell. [153] The stability provided by PEI induces it (DNA) to have greater antifection efficiency than other polycations. [26] Thus the understanding of polymer chain and solvation dynamics at different protonation states can provide benchmarks to study the dynamics of PEI-DNA complexes inside the cells.

In the next chapter (chapter 4), the interaction of PEI in two different protonation states viz., unprotonated and protonated were studied with one of the class of soft matters – Surfactants. Surfactant molecules assembly in presence of polymers are governed by the nature of the polymer, thus highlighting its intriguing behavior.

Chapter 4

Interaction of Polyethyleneimine in two different protonation states with the non-ionic surfactant[1]

4.1 Introduction

In the previous chapter, we had investigated the solvation dynamics of polymer. The study was undertaken in a very dilute solution of polyethylenimine. The presence of polymer affects the morphology of surfactant matrices. These matrices are routinely used in food and drug industries. In this chapter, we explore the molecular level understanding of the interaction of Polyethylenimine with the non-ionic surfactant matrix.

The organization and phase behavior of nanoparticles and polymers dispersed in a matrix, are strongly governed by their interactions with the matrix. These matrix are generally formed by the surfactants. Surfactants are intriguing materials that self-assemble in various forms when mixed with oil and water. In disordered phases they take a structure of spherical droplets of water-in-oil (or oil-in-water) or a bicontinuous structure, in which both water and oil are separated from each other by intertwined interfacial films. In ordered phases they take a rather regular structure of hexagonal arrays of cylindrical tubules made of oil (or water) in surrounding water (or oil) or parallel arrays of alternative oil and water sheets. In these mixtures amphiphile molecules are mostly located at the interface of oil and water with their polar heads directed into water media and with apolar acyl tails into oil media, thus forming interracial monolayers.

[1]Part of the chapter (the structural and pair distributions) were adapted from the publication K. P. Sharma, C. K. Choudhury, S. Srivastava, H. Davis, P. R. Rajamohanan, S. Roy and G. Kumaraswamy, Assembly of Polyethyleneimine in the Hexagonal Mesophase of Nonionic Surfactant: Effect of pH and Temperature , J. Phys. Chem. B 2011, 115, 9059–9069.

The formation of these structures occur above a critical concentration called the critical micelle concentration (c.m.c.). The micelle size and shape depends on various parameters, for example, temperature, pH, salt and type and concentration of co-surfactant. The c.m.c. of non-ionic surfactants is typically lower than that of ionics having a similar number of C-atoms. As the number of C-atoms in the hydrophobic chain increases, the c.m.c. decreases. Temperature and salt may alter the c.m.c. of the ionic surfactants, but for non-ionic surfactants there is no pronounced effect of added salt. The size of the micelle depends on the length of the hydrocarbon chain while shape is determined by the molecular packing to form the aggregate or micelle.

Surface-active molecules reduce the surface tension at the air–water interface, reduce the curvature of water drops on non-polar surfaces, enhances foaming and makes water feel slippery or soapy. Detergents, natural or synthetic, are surface-active molecules specially crafted for washing efficiency. The term surfactant (surface active agent) generally refers to synthetic compounds of high purity (commercial or prepared in the laboratory) with structures designed for particular research applications. Amphiphiles are surface-active molecules found in living systems and mixtures of amphiphiles of various types are the structural elements of biological membrane bilayers of cells and cell compartments, for example, mitochondria, chloroplasts and vacuoles. Often the terms amphiphile or surfactant can be used interchangeably and the word surfactant is generally used here.

Organized mesophases of surfactants are encountered in nature [154, 155] and have technological relevance for a variety of areas. For example, the process of digestion of fat in the intestine is known to involve the formation of liquid crystalline intermediates. [156, 157] Liquid crystalline phases of surfactants are also present in creams and gels that are used in pharmaceutical applications. [158] Mesophase structure is also believed to contribute to the texture and mouth feel of several common foods. [159] Often, when such mesophases occur, they do so in the presence of colloidal particles or polymers – for example, polysaccharides with mesophases in foods. The presence of these polymers or colloidal objects (especially, when the colloid size is comparable to the characteristic mesophase spacing) can dramatically alter the phase behavior of the surfactant and the mesophase structure. Therefore, the interactions of surfactant mesophases with polymers and colloids have implications for diverse applications in nanomedicine and hygiene, food engineering, photonic materials and mesostructured materials for consumer care products, in molecular separations, or catalyst supports. In the food industry, certain surfactants are used as emulsifiers, including the Spans and Tweens, which are used extensively and can form mesophases in water. In addition, oil lipids (monoglycerides, phospholipids and sterol esters) are used and can also form mesophases that promote emulsion stability and stabilize aerated systems (i.e., whipped cream), improve consistency, texture and shelf-life and modify rheological properties.

Thus, it is clear that understanding of how polymers and particles interact with surfactant mesophases has implications for biomedical research, especially in areas such as nanoparticle-based carriers for delivery of medicines and gene therapy. Specific interactions between the polymer and surfactant molecules also influence the mesophase structure. Polyethyleneimine (PEI) is widely used to prepare polymer complexes for pharmaceutical formulations in gene transfection, drug delivery and so on. [159–161] When polymer complexes need to be incorporated in a surfactant matrix, it is important to understand the nature of the interactions between the polymer and the surfactant.

The origin of the problem was from one of our experimental collaborators (Dr. K. Guruswamy, Polymer Science and Engineering Division, CSIR-National Chemical Laboratory) who had investigated the effect of pH (and temperature) upon the self-assembly of the surfactants ($C_{12}E_9$) in presence of polymer-polyethylenimine (PEI). Their NMR experiments (see Figure 4.1) showed that as the pH is decreased, there is a decrease in the strength of PEI-surfactant interactions. Thus, we used the molecular dynamics tool to understand the molecular level interactions which governs the PEI-surfactant interactions. To mimic the pH, we protonated the amine-moiety of PEI for low pH and for high pH PEI chains were not protonated. The computations details involved in this study is described in the next section.

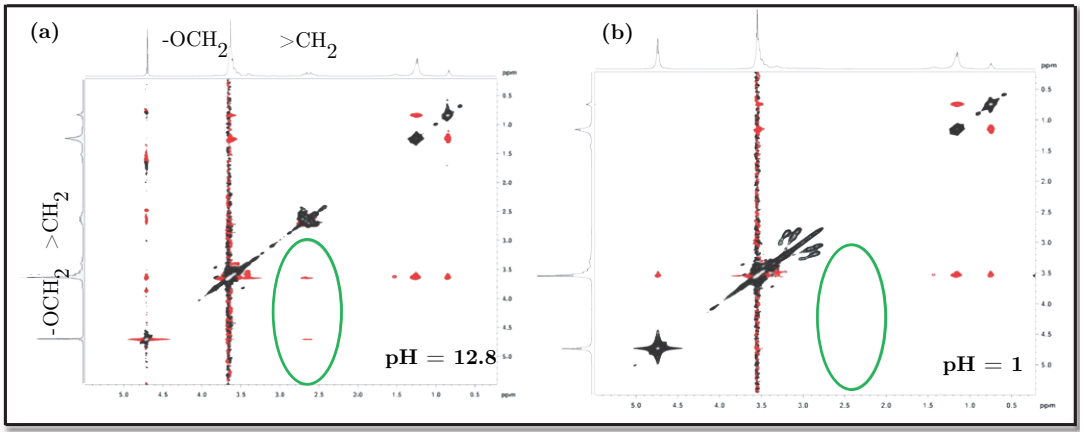

FIGURE 4.1: NMR for 5 wt% PEI in 25 wt% $C_{12}E_9$ in D_2O at (a) pH 12.8 and (b) pH 1.

4.2 Methods

4.2.1 Computational details

We have performed the all atomistic molecular dynamics simulation of

a) a linear 20-mer polyethyleneimine (PEI, -(CH_2-CH_2-NH)-) in water and

b) 10 linear 20-mer PEI chains with 49 surfactant molecules and water.

using Gromacs 4.0.7 simulation package. [129–131] Results from the simulation of 20-mer PEI were compared with the results of Ziebarth et al. [135] to validate our simulations. All the simulations in the present study were performed with the amber force field. [136, 137] as in Ziebarth et al. [135] The PEI chains had three subsystems on the basis of different levels of protonation, namely, no protonation (unprotonated, representative of behavior at high pH, basic medium), protonation on every alternate nitrogen atom along the chain (alternate protonated, representative of intermediate pH) and complete protonation (all protonated, representative of very low pH, acidic medium). For the PEI–surfactant systems, we simulated only the unprotonated and all protonated PEI. Protonation was done at the secondary nitrogen atoms present in the polymer chain. The partial charges for each atom were derived from quantum chemical calculations using the Gaussian 09 package [162] with 6-31G* basis sets and the CHELPG method. [163] The derivation of the charges was necessary because the amber force field did not contain the partial charges of the atom types involved in the present study. All the other parameters (bonded, Lennard-Jones parameters) were adopted from the amber force field itself, as in Ziebarth et al. and are tabulated in Table 3.1 for bonds, for bond bending in Table 3.2, for dihedral angle in Table 3.3 and for van der Waals' in Table 3.4. [135] The charges for each atom type used for the simulation of all the systems are summarized in the Tables 3.5, 3.6 and 3.7 for unprotonated, alternate protonated and all protonated, respectively. The TIP3P water model [138] was used in all simulations. The 20-mer had a single chain solvated with a TIP3P water model, while the PEI–surfactant system consisted of 10 20-mer PEI chains along with 49 surfactant molecules and 6125 and 5887 water molecules for unprotonated and all protonated systems, respectively. The charges for the surfactant atoms were adapted from the OPLS-AA force field. The structure of the surfactant is depicted in Figure 4.2. In the experiments, pHs were controlled with the nitric acid.

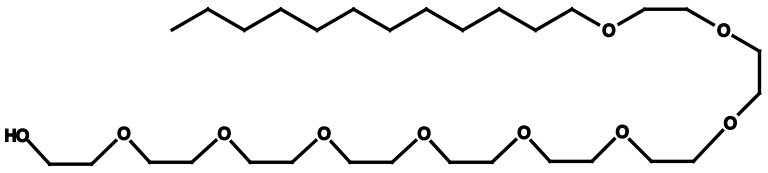

FIGURE 4.2: Surfactant ($C_{12}E_9$) structure.

Experiments also showed that the concentration dependence of the viscosity of PEI solutions at different values of pH does not depend on whether nitric or hydrochloric acid was used to adjust the pH. Thus, in simulations we used the chloride as the counter ions to neutralize the alternated and all protonated PEI systems. Also the force fields for

nitrate ions were not available. Therefore, we believe that the trends from the simulation data (obtained using a chloride counterion) may be compared with the experimental data (where nitric acid was used to adjust the pH). The time step of integration in our simulations was 0.001 ps for every system. The electrostatic and nonbonded potential cutoff was 1.2 nm and Particle-Mesh Ewald [114] was used to take care of the electrostatic interactions. Simulations were carried out at 300 K for a 50 ns production run for PEI single chains in water and at 400 K for a 100 ns production run for the PEI–surfactant systems (NPT ensemble using Berendsen barostat [122] with time constant of 1.0 ps and v-rescale temperature coupling [123] with time constant of 0.100 ps). The trajectory was recorded after every 2 ps. Simulations during pre- and post equilibration (5 ns of simulation) were not included for our analysis.

4.3 Results and discussions

4.3.1 Single linear 20-mer PEI chain in water

4.3.1.1 Structural properties of polymer

To investigate the size and shape of PEI chain as a function of ionization along the chain, we did all atom molecular dynamics simulations for a single chain in water. The simulations were carried out on a linear PEI chain containing 20 monomer units of -(CH_2-CH_2-NH)-. We performed simulations for 50 ns and the last 10 ns of the trajectory was used for analysis of the end-to-end distance and the radius of gyration (R_g) to understand the effect of protonation on the size and the shape of the polymer chain. For the all protonated system, the end-to-end distance and the radius of gyration (R_g) are greater than that of the alternate protonated and unprotonated systems (Figures 4.3 and 4.4 and Table 4.1). Figure 4.5 shows the representative snapshots of the different protonation states of the 20-mer PEI chain. These figures were created using PyMol [164]. Clearly, the PEI chain expands due to repulsion between the charged amine groups as the pH is reduced. The end-to-end distance and R_g for the unprotonated 20-mer chain is in agreement with the calculations reported by Zakharova et al. [165] We also

TABLE 4.1: Average end-to-end distance (nm) and radius of gyration (R_g) (nm) for 20-mer PEI chain at different protonation states.

	unprotonated	alternate protonated	all protonated
end-to-end distance	2.37 ± 0.82	3.83 ± 0.56	5.38 ± 0.56
radius of gyration (R_g)	0.97 ± 0.16	1.27 ± 0.56	1.79 ±0.74

computed the nearest neighbor (NN) and next nearest neighbor (NNN) for unprotonated,

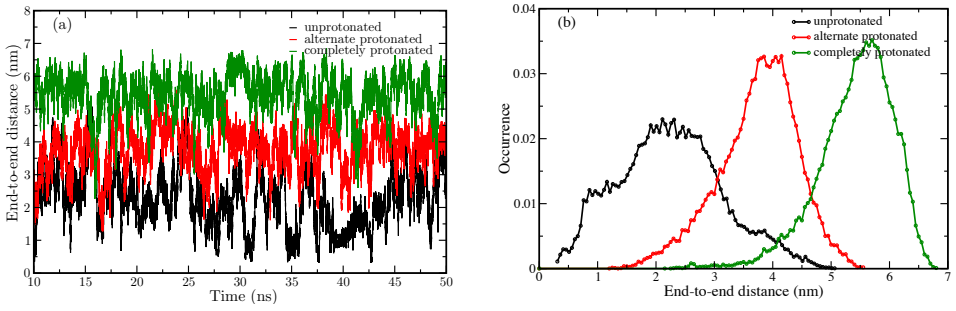

FIGURE 4.3: (a) End-to-end distance and (b) its distribution of 20-mer PEI for different protonation states.

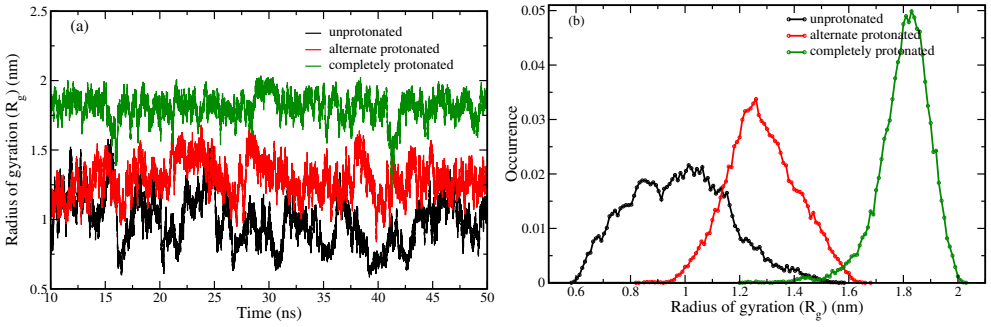

FIGURE 4.4: (a) Radius of Gyration and (b) its distribution of 20-mer PEI for different protonation states.

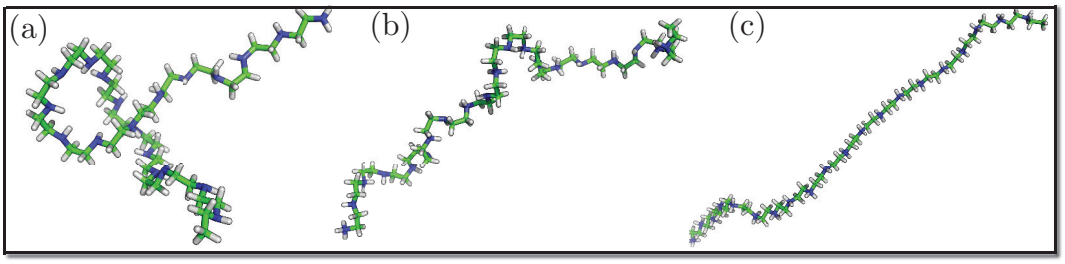

FIGURE 4.5: Shows the conformations of PEI when the chains are (a) Unprotonated, (b) Alternate protonated and (c) All protonated. They represents the R_g tabulated in Table 4.1.

alternated protonated and all protonated systems and plotted them in Figures 4.6(a) and 4.6(b), respectively. We note that the NN (Figure 4.6(a)) and NNN (Figure 4.6(b)) distributions for the 20-mer chains are in quantitative agreement with Ziebarth et al. [135] The NN distribution (Figure 4.6(a)) exhibits two prominent peaks at 0.29 and 0.38 nm, for both unprotonated and alternate protonated chains. The all protonated state also exhibits two peaks, with a weak peak at 0.32 nm and a stronger peak at 0.38 nm. These peaks correspond to the *syn*- and *anti*-conformation, respectively, suggesting that, in the all protonated system, the neighboring nitrogen atoms are mostly *anti*. For the NNN distribution (Figure 4.6(b)), the *syn–syn*, *syn–anti* and *anti–anti* configurations correspond to distances of ∼0.57, ∼0.65 and ∼0.73 nm, respectively.

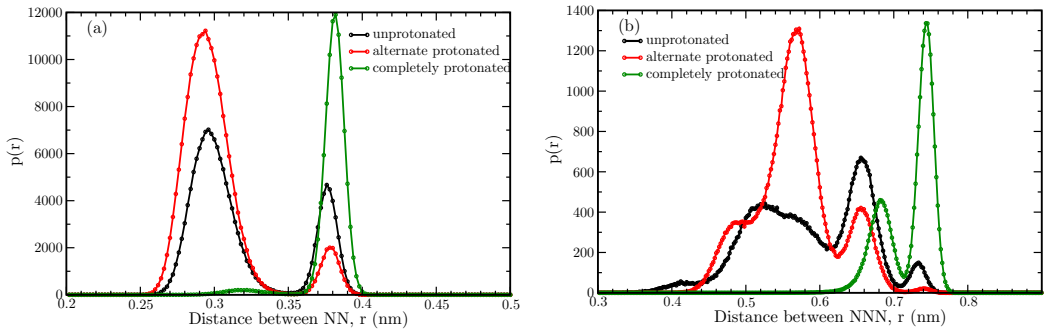

FIGURE 4.6: (a) The nearest neighbor, NN and (b) The next nearest neighbor, NNN distributions of the nitrogen atoms for the 20-mer PEI.

4.3.2 PEI chains with surfactant molecules

4.3.2.1 Pair distribution of polymer chains and surfactant molecules

Simulations of the nonionic surfactant H_1 mesophase are computationally very expensive. Therefore, to understand surfactant–PEI interactions, we simulate a system having 10 20-mer PEI chains and 49 surfactant molecules, solvated with TIP3P water molecules (see Figure 4.7). We performed 100 ns simulations, for both the unprotonated PEI and

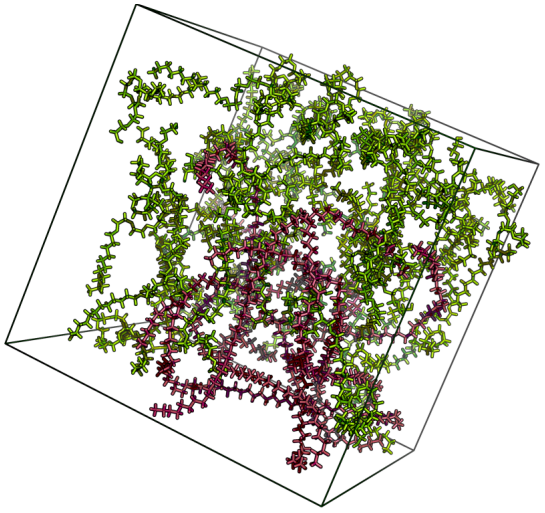

FIGURE 4.7: Shows the initial snapshots of the PEI–Surfactant–Water system. Water molecules are not shown for clarity. Surfactant molecules are shown in green and the PEI molecules are presented in violet as a ball and stick model.

all protonated PEI systems with surfactants and the trajectory for the last 10 ns has been analyzed. Figure 4.8, created using PyMol [164], clearly depicts the differences in interaction of the all protonated (Figure 4.8(b)) and unprotonated (Figure 4.8(a)) PEI chains with the surfactant. In Figures 4.7 and 4.8, the water molecules are not shown for

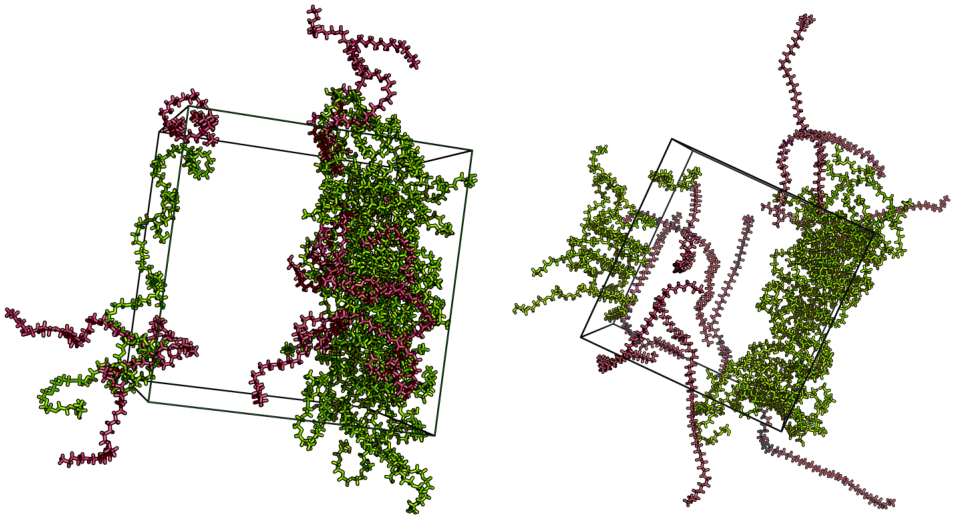

FIGURE 4.8: Shows the snapshots at 100^{th} ns for the PEI–Surfactant–Water system. Left panel is when unprotonated PEI is considered and rigth is one when the protonated PEI is considered. Water molecules are not shown for clarity. Surfactant molecules are shown in green and the PEI molecules are presented in violet as a ball and stick model.

clarity. The surfactant self-assembles with its nonpolar tail buried inside, shielded from the water molecules by the polar head groups.

Dipolar interactions To check the interaction between the surfactant molecules and the PEI chains, we plotted the pair distribution between the oxygen atoms of the surfactants and nitrogen atoms of the PEI chains (Figure 4.9(a)). The minima for the first peak for both the fully protonated and unprotonated cases are at 0.36 nm. We find a higher value of the peak for the unprotonated system, indicating that this system has higher attractive interactions between the PEI and the surfactant molecules, as compared to the all protonated system. We observe that integrating the first peak for the unprotonated system yields a 10-fold higher peak area compared with the all protonated system. This result is in good accord with the experimental NMR observations.

Hydrophobic interactions We have also plotted the pair distribution of C-atoms of the PEI chains and the C-atoms on the hydrophobic part of the surfactant molecules in Figure 4.9(b). We find that this hydrophobic interactions is dominated for the unprotonated system. Thus, along with the dipolar interactions, the hydrophobic interactions also contributes in the PEI–surfactant interactions resulting them to assemble. While for the all protonated such interactions are very feeble.

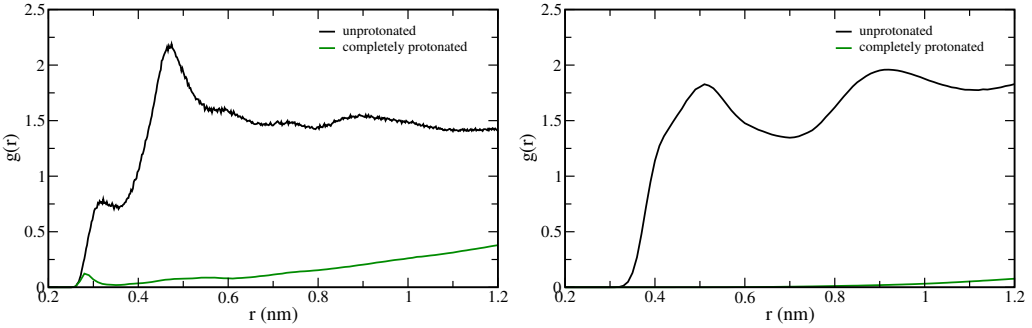

FIGURE 4.9: Pair distribution of (a) all the N- atoms present in the PEI chain and all the O- atoms present in the surfactant molecules, (b) the hydrophobic segments of the PEI chains and the surfactant molecules.

4.3.2.2 Solvation shells of polymer chains and surfactant molecules

To understand the arrangement of water molecules around the polymer chains and the surfactant molecules, we have computed the radial distribution of O-atom of water molecules and N-atom of PEI chains in Figure 4.10(a) and O-atom of water molecules and O-atom of surfactant molecules in Figure 4.10(b) for the unprotonated and the protonated systems. The water molecules around the all protonated PEI chains are

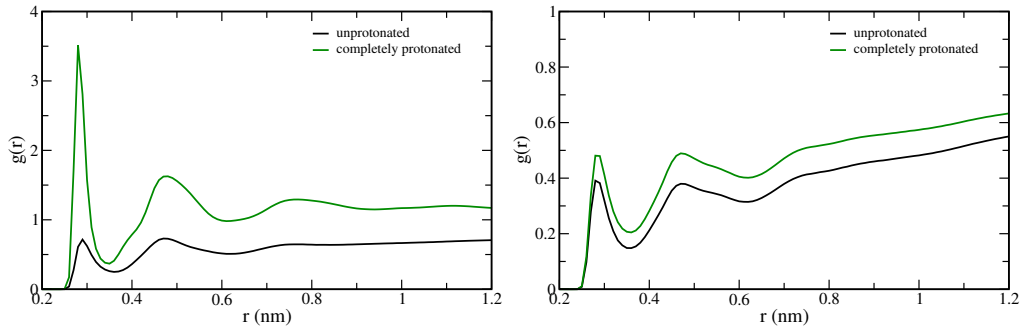

FIGURE 4.10: Radial distribution of O-atoms of water molecules with (a) N-atoms of PEI chains and (b) O-atoms of surfactant molecules for unprotonated and protonated systems.

highly ordered, forming multi layer of solvation shells, while the water molecules around the unprotonated chains are sparse (Figure 4.10(a)). The arrangement of water molecules along the head groups of surfactant are scare because of low availability of head group's surface area. This arrangement is similar for the unprotonated and protonated systems.

The prominent peak in the pair distribution of water molecules around the protonated PEI chains suggests that the PEI chains are solubilized in water. The interaction between the surfactant molecules and PEI chains are screened and eventually avoids the chains to aggregate with the surfactant molecules. While the modest solvation shell around the unprotonated PEI, causes the unprotonated PEI to assemble with surfactant molecules.

4.3.2.3 Dynamical properties

Diffusion of PEI chains and surfactant molecules The protonated PEI chains separates out with the surfactant molecules. The effect of this aggregation on the dynamical property was investigated. The mean square displacement (MSD) of the PEI chains and the surfactant molecules were calculated for the unprotonated and the protonated systems. The MSD are shown in Figure 4.11. The diffusion coefficients obtained from these plots are tabulated in Table 4.2. The diffusion of PEI chains is faster in the all protonated system. The diffusion of surfactant molecules are similar for both the systems. As the surfactant molecules interacts substantially with the unprotonated PEI chains, the diffusion of PEI chains are also slowed down.

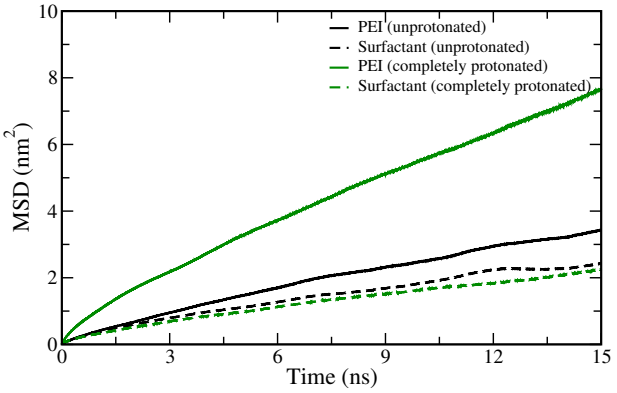

FIGURE 4.11: Pair distribution of the hydrophobic segments of the PEI chains and the surfactant molecules.

TABLE 4.2: Diffusion coefficients, D, 10^{-5} cm^2 s^{-1} for PEI and surfactant molecules in unprotonated and protonated systems, computed using the Equation 3.3.

	unprotonated	all protonated
PEI chains	0.031 ± 0.001	0.071 ± 0.002
Surfactant molecules	0.022 ± 0.002	0.018 ± 0.001

4.4 Conclusions

We investigated the interaction of PEI (in two different protonation states) with the non-ionic surfactant molecules in the aqueous medium. It is known that the non-ionic surfactant molecules being amphiphilic in nature self-assembles to form hexagonal mesophases. Experimentally it was shown that the PEI in high pH chemical environment disrupts the formation of this phase, while in the low pH condition, the hexagonal mesophase was formed. NMR experiments did provide the evidence of the interaction of PEI with surfactant was substantial in high pH. To gain the molecular level interactions,

the molecular dynamics simulations were performed with 20-mer PEI at different protonation states – unprotonated, alternate protonated and completely protonated. The protonated PEI goes to solution phase more easily than unprotonated PEI, because the solvation energy of protonated PEI overrides the interaction energy with surfactant molecules. For protonated PEI, we observe an extended chain structure, allowing the water to access the chain more than for the unprotonated PEI. Thus, the protonated PEI gains solvation energy. This interaction between the PEI and the surfactant inhibits formation of the H1 phase. PEI chains phase separated from the hexagonal mesophase and aggregated at the hexagonal domain boundaries to form opaque PEI/hexagonal phase composite structures. Also the protonated linear PEI chains (representative of the low pH state) interact less strongly with the non-ionic surfactant, when compared with unprotonated chains (representative of the high pH state). The protonated chains are extended relative to the unprotonated chains, thus, possibly explaining the formation of anisotropic PEI aggregates at pH = 1. Also, the self-assembly has an effect upon the dynamics of the individual components. As the surfactant molecules interacts substantially with the unprotonated PEI chains, the diffusion of PEI chains are slowed down.

Gaining the insights of the surfactant and PEI interactions, we explore (in the next chapter) the interactions of PEI with biological membrane. PEI is known to be a gene delivery vector and thus it interacts with biological membrane while delivering the genetic contents to the target. Lipid molecules are in abundant in the membranes. In the next chapter, we investigate the interactions of PEI at two different protonated states with the lipid bilayer.

Chapter 5

PEI biomembrane interaction[1]

5.1 Introduction

The polymer and surfactant matrices are used in the drug industry for the therapeutic release of drug to the target cells. In the previous chapter, we had investigated the behavior of surfactant matrix in presence of polyethylenimine at different pH. The drugs can be carried to the target cells with the polycationic polymers like polyethylenimine. In this pathway to deliver the drug, the polymer encounters different pHs. They also interact with the lipid membranes. In this chapter we have explored the molecular level interactions of polyethylenimine with the lipid bilayer membrane.

Polycations has been used for the delivery of genetic materials to the cells. [44, 166, 167] They are also used as biocidal agents. [168–170] Thus the study of the impact of synthetic and natural polycations on the bilayer membranes is very crucial. Polycations are internalized in the cell in three steps (a) binding of polycations with the phospholipids and/or glycolipids in membrane, (b) internalization into the cells and (c) exit from the endosomes, [24, 171, 172] this whole process is termed as polycation-meditated endocytosis. In the recent past researchers have widely used polycationic polymers to disrupt the cell membranes and transport materials to the cell. [40–45] Helander et al. [40] studied the microbicidal activity of Polyethylenimine (PEI), a polycationic polymer and its interaction with Gram-negative bacteria. They concluded that Gram-negative bacteria are permeable to hydrophobic probes such as antibiotics and 1-*N*-phenylnaphthylamine because of the presence of PEI. Mecke et al. [41] investigated the dimyristoylphosphatidylcholine (DMPC) supported lipid bilayers using atomic force microscopy with different sizes of poly(amidoamine) (PAMAM) dendrimers, a polycationic polymer. They observed that

[1]This chapter is adapted from the publication C. K. Choudhury, A. Kumar and S. Roy, Characterization of Conformation and Interaction of Gene Delivery Vector Polyethylenimine with Phospholipid Bilayer at Different Protonation State, Biomacromolecules, 2013, 14 (10), 3759 – 3768.

the higher generation dendrimers (e.g., G7) caused the formation and growth of holes in membranes whereas the ability to remove lipids from bilayers was reduced for G5 and completely lost for G3. Sikor et al. [44] in their study showed that the non-specific interactions between the polyplexes and the unilamellar DMPC vesicle in presence of PEI result in the transport of molecules to the cell nucleus. The genetic materials were transfected by the opening of small pores in the nuclear membrane. Dynamic light scattering and zeta potential study showed that the interaction of modified polycation (by introduction of hydrophobic group) with 1-palmitoyl-2-oleoyl-*sn*-glycero-3-phosphocholine (POPC) membrane enhances the hydrodynamic radius and zeta potential. [43] This has been associated with the penetration of polycation into the lipid bilayer. The hydrophilic pore formation in the lipid bilayer because of the incorporation of polycation facilitates the flow of water and ions through it. [43]

PEI based gene vectors are considered as the versatile gene delivery agents. [24, 167] The polyplexes are formed with linear (LPEI) or branched (BPEI) PEI. PEI complexes with nucleic acids through electrostatic interactions forming polyplexes. These polyplexes enter the cell through endocytosis. The comparative transfection efficiency of LPEI or BPEI is quite controversial. Dai et al., [173] reported that both the LPEI and BPEI have similar transfection efficiency when N/P ratio is higher where N is the number of polymer nitrogen atoms and P the number of DNA phosphorus atoms. In this scenario, all the PEI's interaction sites are not bound with the polyplex some free PEI fraction exists. These free PEI's apart from enhancing the transfection efficiency also give rise to toxicity. [174] The mechanism of the escape of polyplex after the internalization is debatable. The most general accepted mechanism is the "proton sponge" hypothesis. [153] However, alternative mechanisms are also suggested. [175] A recent study has shown that the "proton sponge" effect of PEI does not include the change in lysosomal pH and this led them to believe that this effect is not the dominant mechanism of polyplex release. [176] Thus the study of interaction of PEI with bilayer and the mechanism of transfection of PEI into cells are of immense interest for the gene therapy community. Although the interactions of PEI with lipid bilayers have been investigated experimentally [40, 41], no simulations have been performed. Molecular simulations can provide detail insight about the interaction of lipids and PEI and its effect on the bilayer membrane. Therefore, the scope of this chapter spans from understanding conformation of PEI in different protonation states, which mimics the low and high pH in the lipid bilayer to the transfection mechanism of PEI along with pore formation.

In this chapter, we report results based on simulation of linear PEI (LPEI) in different protonation states with 1,2-dioleoyl-*sn*-glycero-3-phosphocholine (DOPC) molecules (see Figure 5.1). We have used classical molecular dynamics (MD) simulations to determine how LPEI interacts and changes conformation with the lipid-bilayer membrane. We

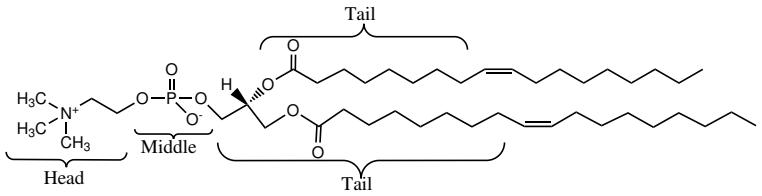

FIGURE 5.1: 1,2-dioleoyl-*sn*-glycero-3-phosphocholine (DOPC). Atoms considered for the center of mass calculation for head, middle and tail moieties are shown.

mimic LPEI in two different pH conditions, high and low i.e., basic and acidic respectively. A low pH (acidic conditions) leads to the protonation of nitrogen atoms of the LPEI chain and here we term it as protonated PEI while at high pH (basic conditions) we call unprotonated PEI. We have allowed PEI to sample conformations with lipid bilayer by placing it in different probable sites in the bilayer. Protonated PEI chain indeed damages the structural integrity of the lipid bilayer forming hydrophilic pores. Helander et al. have experimentally reported this. [40] We observe the change in the orientation of the lipid molecules alongside the pore. We also addressed the water dynamics along the pore.

5.2 Methods

5.2.1 Computational details

We had performed all atom molecular dynamics (MD) simulations of lipid bilayer along with one Polyethylenimine (PEI) chain. The equilibrated structure of 72 DOPC molecules was obtained from Siu et al. [177] To increase the length scale, this system was replicated along Y-axis, forming bilayer with 144 DOPC lipid molecules (see Figure 5.2). This pure lipid bilayer system was then simulated for 250 ns for characterizing the bilayer properties. Last 100 ns of trajectory was used for the analysis and bilayer properties were computed and tabulated in Section 5.3.1. The area per lipid of pure system was 0.76 ($\pm$ 0.02) nm^2, which is very close to that of the reported by Siu et al. [177] (0.74 ($\pm$ 0.03) nm^2). The difference in area per head group can be attributed to the size of the system. The mean square lateral displacement was computed for the Phosphorous atoms present in each leaflet of the bilayer. It was calculated by averaging last 100 ns of trajectory in steps of 10 ns. The lateral diffusion coefficient obtained was 1.84×10^{-7} cm^2/s while the experimentally reported from pulsed field gradient NMR experiment was 1.37×10^{-7} cm^2/s. [178] Thus good agreement of these values validates the bilayer structure and properties. In addition to these properties, we had also calculated the bilayer width (calculated as the distance between the intersection line of the density profiles of the lipid and water molecules) which was 3.83 nm. PEI in both forms (unprotonated and

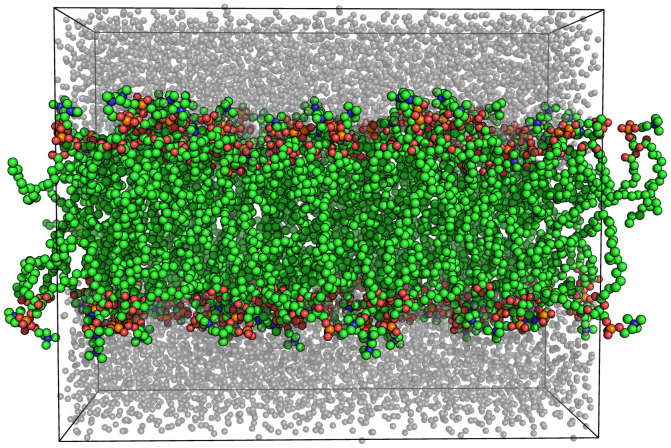

FIGURE 5.2: Snapshot of the pure lipid-bilayer system. The system consisted of 144 lipids with 72 lipids in each leaflet. Water molecules are shown as grey spheres. H-atoms are not shown for clarity.

protonated) were studied in chapter 3, where we have characterized the PEI conformation and dynamics in pure water. The radius of gyration (R_g) gives a sense of the size of the polymer coil. The end-to-end distance is the distance that connects the two terminal atoms of the polymer chain while the square radius of gyration (R_g^2) is the average squared distance of any point in the polymer coil from it's center of mass. The average end-to-end distance and radius of gyration of unprotonated PEI in water were 2.37 ($\pm$0.82) nm and 0.97 ($\pm$0.16) nm while for protonated PEI these values were 5.38 ($\pm$0.56) nm and 1.79 ($\pm$0.74) nm, respectively (see Section 5.3.1). [179]

PEI, being an efficient gene delivery agent its atomic level interaction with biological membrane and its outfall is very crucial to understand. As the all atomistic MD simulation limits itself to the short time scale (in the range of nanoseconds), it is almost impossible to predict the probable insertion mechanism of polymer in the lipid bilayer from the solution. Coarse graining of the PEI and bilayer molecules could enhance the time scale to an order of magnitude higher, however one would miss some important local atomistic level interactions. Thus it is reasonable to consider initial position of PEI by placing it at different favorable positions of the bilayer. So, to study the PEI-bilayer interaction, different sets of simulations were performed where unprotonated and protonated linear PEI chain was separately placed in different regions of the lipid bilayer system. The unprotonated PEI is a coiled polymer while the protonated PEI is elongated. [100, 179] The initial coordinates were constructed by placing PEI at the water or the bilayer region. Unprotonated PEI with different radii of gyration were prepared separately by placing it in the bilayer hydrophobic region (system Un_b, see Figure 5.3(a) and Figures 5.4(a), 5.4(c) and 5.4(e)) and in the water region (system Un_w, see Figure 5.5(a) and Figures 5.6(a), 5.6(c) and 5.6(e)). Protonated PEI, being elongated, three different positions in the bilayer-water system were probable where it could be placed. It was placed in the middle

of the two bilayer leaflets (i.e. in the hydrophobic region), perpendicular to the Z-axis (system Pr_b$_\perp$, see Figure 5.7(a)) i.e, bilayer plane. In second simulation, it was placed parallel to the Z-axis, spanning across the water and bilayer regions (system Pr$_{||}$, see Figure 5.8(a)) and in the third set, it was placed in the water region, perpendicular to the interfacial axis (Z-axis) (system Pr_w$_\perp$, see Figure 5.9(a)). These figures were generated using PyMOL. [164]

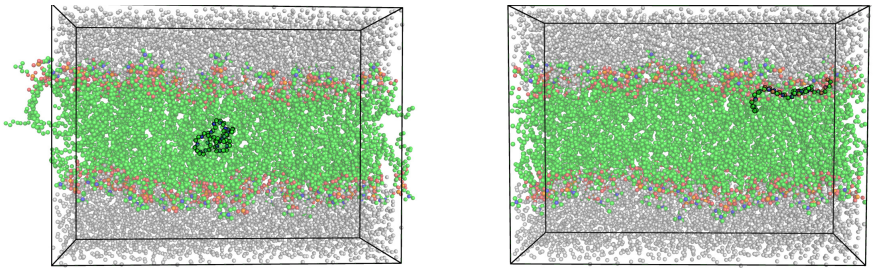

(a) 0 ns (b) 250 ns

FIGURE 5.3: Snapshots of Un_b system at (a) 0 ns and (b) 250 ns. Here PEI was placed in the bilayer region at 0 ns, (a). Water molecules are shown as grey spheres. To obtain the clear position of PEI, DOPC and water molecules have been made transparent by 30%. H-atoms are not shown for clarity.

For each of these systems, the simulation conditions were adopted from Siu et al. 's article. [177] Amber force field [136, 137] was used for DOPC [177] and PEI [100]. TIP3P water model [138] was used to solvate each system such that no water molecules were present inside the bilayer. The hydrogen bonds were constraint with the LINCS algorithm. [120] The time step of integration was 2 fs. Periodic boundary conditions were applied in all directions. The non-bonded potential energy cut-off was 1.0 nm. Particle-Mesh Ewald algorithm [114] was used for long range electrostatic interactions. The simulations were performed using Gromacs-4.5.5 [130] with NPγT ensemble. All the simulations were performed at 310 K (well above the transition temperature of 253 K). Berendsen thermostat and barostat [122] were used for the temperature and pressure coupling with time constant of 10 fs and 1 ps, respectively. The DOPC bilayers were subjected to a surface tension, γ, of 220 bar/nm per surface with reference z-pressure of 1 bar and volume compressibility of 4.5×10^{-5} bar^{-1}.

Initially, systems Un_b and Un_w were equilibrated for 4 ns by position restraining the PEI molecule at its mean position such that the neighboring molecules get equilibrate with the PEI molecule. Water and PEI molecules of system Pr$_{||}$ and Pr_b$_\perp$ were position restraint for 0.5 ns. For system Pr_w$_\perp$, only the PEI chain was position restraint for 0.5 ns. For each of these systems, the position was restraint with force constant, k_{pr} of

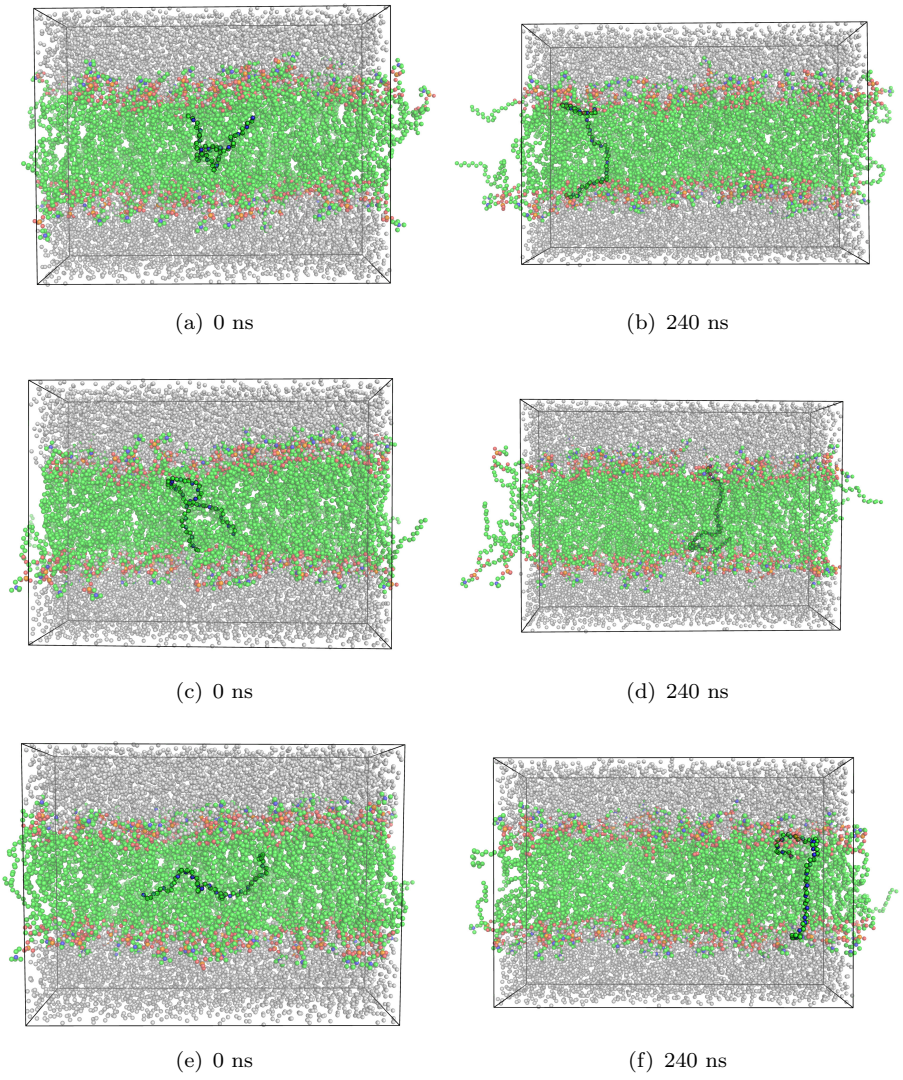

(a) 0 ns (b) 240 ns

(c) 0 ns (d) 240 ns

(e) 0 ns (f) 240 ns

FIGURE 5.4: Snapshots of Un_b system with R_g 0.80 nm (a & b), R_g 1.10 nm (c & d) and R_g 1.25 nm (e & f). Here PEI was placed in the bilayer region at 0 ns. Water molecules are shown as grey spheres. To obtain the clear position of PEI, DOPC and water molecules have been made transparent by 30%. H-atoms are not shown for clarity.

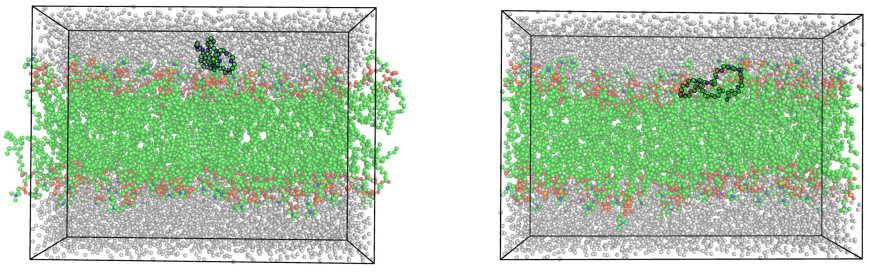

(a) 0 ns (b) 250 ns

FIGURE 5.5: Snapshots of Un_w system at (a) 0 ns and (b) 250 ns. Here PEI was placed in the water region at 0 ns. Water molecules are shown as grey spheres. To obtain the clear position of PEI, DOPC and water molecules have been made transparent by 30%. H-atoms are not shown for clarity.

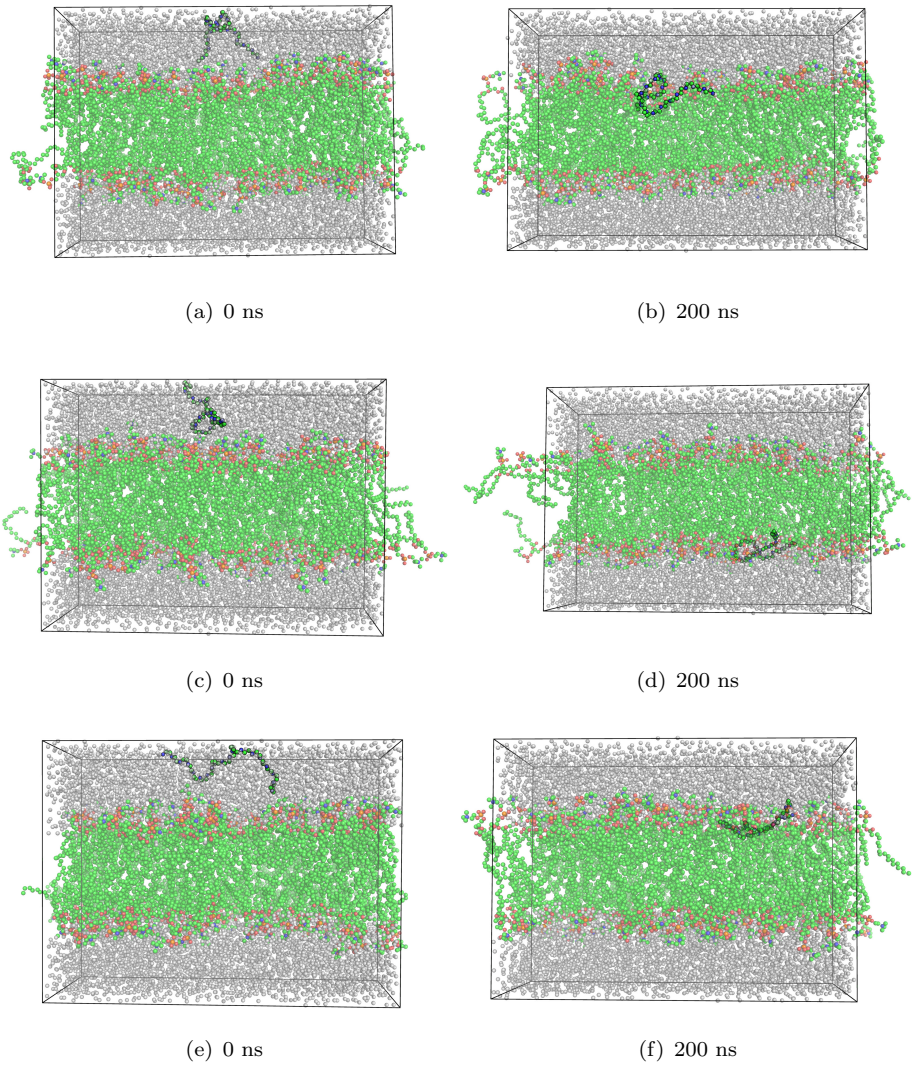

(a) 0 ns (b) 200 ns

(c) 0 ns (d) 200 ns

(e) 0 ns (f) 200 ns

FIGURE 5.6: Snapshots of Un_w system with R_g 0.80 nm (a & b), R_g 1.10 nm (c & d) and R_g 1.25 nm (e & f). Here PEI was placed in the water region at 0 ns. Water molecules are shown as grey spheres. To obtain the clear position of PEI, DOPC and water molecules have been made transparent by 30%. H-atoms are not shown for clarity.

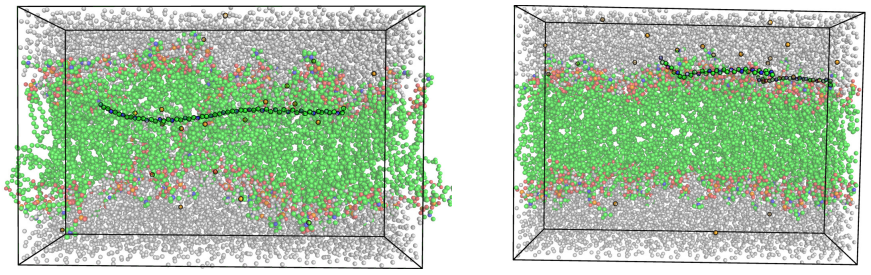

(a) 0 ns (b) 250 ns

FIGURE 5.7: Snapshots of Pr_b$_\perp$ system at (a) 0 ns and (b) 250 ns. Here PEI was placed in the middle of the bilayer region, perpendicular to Z-axis at 0 ns. Water molecules are shown as grey spheres. To obtain the clear position of PEI, DOPC and water molecules have been made transparent by 30%. H-atoms are not shown for clarity.

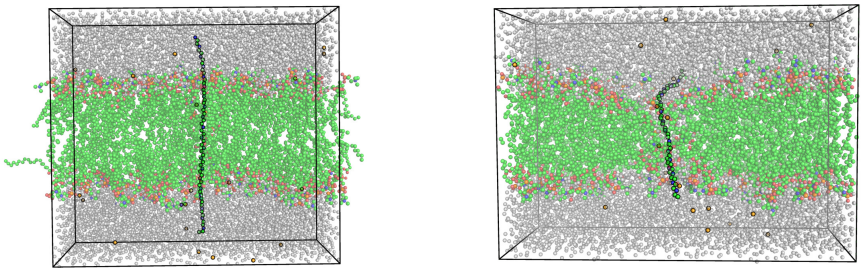

(a) 0 ns (b) 250 ns

FIGURE 5.8: Snapshots of $Pr_{||}$ system at (a) 0 ns and (b) 250 ns. Here PEI was placed parallel to the Z-axis, spanning across the water and bilayer regions at 0 ns. Water molecules are shown as grey spheres. To obtain the clear position of PEI, DOPC and water molecules have been made transparent by 30%. H-atoms are not shown for clarity.

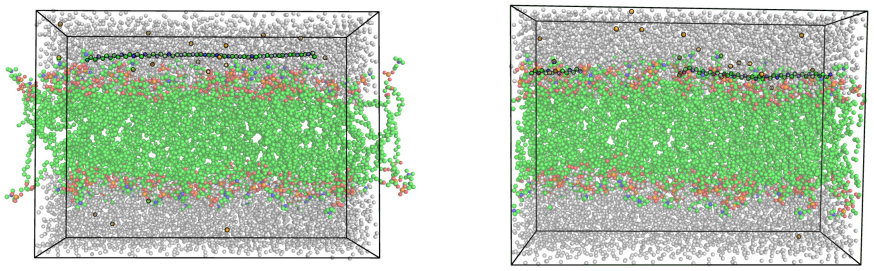

(a) 0 ns (b) 250 ns

FIGURE 5.9: Snapshots of $Pr\_w_{\perp}$ system at (a) 0 ns and (b) 250 ns. Here PEI was placed in the water region, perpendicular to the interfacial axis (Z-axis) at 0 ns. Water molecules are shown as grey spheres. To obtain the clear position of PEI, DOPC and water molecules have been made transparent by 30%. H-atoms are not shown for clarity.

1000 kcal $mol^{-1}nm^{-2}$ by using the following equation,

$$V_{pr}(r_i) = k_{pr}|r_i - R_i|^2 \tag{5.1}$$

The position restraining of PEI molecules affirms us to obtain equilibrated water or lipid molecules around it. The coordinate files at the end of these simulations were used as initial structures for further simulations of 250 ns. The trajectories were recorded at an interval of 1 ps. Last 100 ns of the production runs were analyzed. A frame near 250 ns was extracted from $Pr_{||}$ system such that the whole of PEI was inside the simulation box. This frame served as the initial structure for another 100 ns simulation where the trajectory was recorded every 100 fs. This extracted structure was also used for generating a condensed trajectory of 4 ns, recording the trajectory at every 10 fs. This condensed trajectory was used for analyzing the dynamical properties of water molecules in the bilayer pore.

In this chapter, PEI was placed in the bilayer and the water region in different simulated systems. We have compared the end-to-end distance and the radius of gyration of PEI

in different protonation states when placed in lipid bilayer system. These values were important benchmark to understand the structural properties of PEI in interaction with bilayer system.

5.3 Results and discussions

The properties for the lipids with embedded unprotonated and protonated PEI had been computed and discussed. These properties were compared with the pure lipid-water system. Also the structural properties of PEI for each of the systems were evaluated. These properties were compared with the pure PEI-water system. For $Pr_{||}$ system disruption of bilayer was observed due to the formation of pore. The conformations of lipids and the dynamics of water in the *vicinity* of pore were also studied.

5.3.1 Structural and dynamical properties of bilayer

The partial density along the interfacial axis (Z-axis) for DOPC, water and PEI molecules were computed and plotted in Figure 5.10 for every system. The bilayer width calculated as the distance between the intersection points of the density plot of lipid and water was smaller for system Un_w (3.70 nm) as compared to the pure lipid-bilayer (3.83 nm) and Un_b (3.85 nm) systems (Figure 5.10, Section 5.3.1 and Table 5.1). Bilayer width for $Pr_{||}$ system was ca. 3.50 nm, for systems $Pr\_b_{\perp}$ and $Pr\_w_{\perp}$ was ca. 3.86 nm, Table 5.1. The bilayer width for the $Pr\_b_{\perp}$ system and $Pr\_w_{\perp}$ systems were close to the pure lipid-bilayer system (Section 5.3.1). But, $Pr_{||}$ system had much smaller bilayer width. From the partial density plot (Figure 5.10(b)), we could notice that the partial density of the lipid molecules for $Pr_{||}$ system was less than the other two systems. We also observed (from the density profile of water molecules) that there was finite density of water molecules along the hydrophobic region for system $Pr_{||}$ (also see Figure 5.8(b)). In this system ($Pr_{||}$), protonated PEI chain was placed parallel to the Z-axis spanning across the lipid molecules with ends in the water region (refer Figure 5.8(a)). The finite density of water molecules in the interior of the bilayer suggests the presence of water molecules which were in connection with the bulk water. The existence of water molecules can be attributed to the presence of partially hydrophilic protonated PEI chain, which passes through the bilayer region. The polymer chain being charged attracts water molecules, which find a path to cross the bilayer region. Disruption in the bilayer due to this, decreases the overall average partial density of the lipid molecules. However, decrease in bilayer width for this system was subject to further investigation, which is discussed later in this chapter. This disruption resulted in the pore or channel formation as snapshot after 250 ns of simulation (see Figure 5.8(b)) also suggests the same. The position of

TABLE 5.1: Properties of the lipid (DOPC)–water–PEI System

		Unprotonated PEI		Protonated PEI		
		Un_b	Un_w	$Pr_{\|\|}$	$Pr\_b_{\perp}$	$Pr\_w_{\perp}$
Lipid	Bilayer Width (nm)	3.85	3.70	3.50	3.86	3.86
	Avg. area per lipid (nm^2)	0.76 (± 0.14)	0.76 (± 0.02)	0.83 (± 0.02)	0.76 (± 0.02)	0.75 (± 0.02)
	Lateral Diff. coeff. ($10^{-7} cm^2/s$)	1.54 (± 0.25)	1.56 (± 0.26)	1.21 (± 0.20)	1.11(± 0.18)	1.42 (± 0.23)
PEI	Avg. end-to-end distance (nm)	2.82 (± 1.01)	0.84 (± 0.34)	6.50 (± 0.25)	6.56 (± 0.13)	6.81 (± 0.21)
	Avg. R_g (nm)	1.13 (± 0.17)	0.76 (± 0.04)	2.01 (± 0.05)	2.01 (± 0.03)	2.08 (± 0.03)

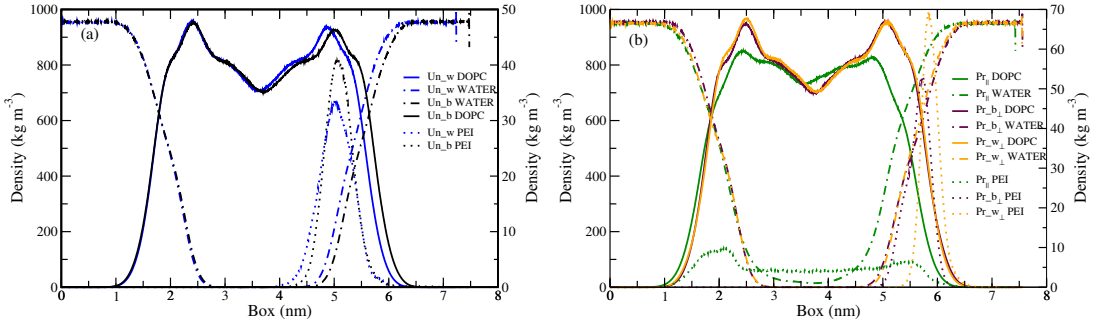

FIGURE 5.10: Partial density profile for (a) unprotonated and (b) protonated PEI–bilayer–water system. The density plots (of water and lipids) for each of the systems were shifted such that the intersection points coincide. The density for PEI is placed on the right side.

PEI after equilibration for systems Un_b and Un_w, in Figure 5.10(a), were almost the same. The PEI molecules diffused to the interface (see Figures 5.3(b) and 5.5(b)) from their respective starting positions i.e. from water (Un_w) and from middle of the bilayer (Un_b). This indicates whether one simulates PEI by placing it in the bilayer region (as in system Un_b) or in the water region (system Un_w), it ends up at the interfacial position because of favorable interactions. Thus the starting position of unprotonated PEI was immaterial. However, the question remains whether the initial position (initial interactions with the regions) could favor some specific conformation of PEI. Therefore, the conformational analysis of PEI is also an important aspect of this chapter.

Area per lipid is one of the important structural characteristics of bilayer and it also serves a quantity to confirm equilibration of such self-assembled system. Area per lipid for all the systems are plotted in Figure 5.11 and tabulated in Table 5.1. From the plots it was apparent that the systems were well equilibrated. For system Un_b, average area per lipid molecule was 0.76 (± 0.14) nm^2 and for system $Un\_w_{\perp}$ it was 0.76 (± 0.02) nm^2. The average area per lipid for system $Pr\_b_{\perp}$ and $Pr\_w_{\perp}$ were 0.76 (± 0.02) and 0.75 (± 0.02) nm^2, respectively (Table 5.1). These values were same as that of the pure lipid-bilayer system (refer Section 5.3.1). So, the presence of unprotonated (Un_b, Un_w) and protonated (systems $Pr\_b_{\perp}$ and $Pr\_w_{\perp}$) PEI did not change the lateral area. A visual inspection of the $Pr_{||}$ system showed that the conformation of lipid molecules in the *vicinity* of PEI had changed. This had resulted in the increase of the area per lipid of

this system. Further in the chapter, we have analyzed the orientation of lipid molecules around the polymer chain for $Pr_{||}$ system.

TABLE 5.2: Properties of lipid (DOPC)–water system and PEI (unprotonated and Protonated)–water system.

Lipid	Bilayer Width (nm)	3.83 [a]
	Avg. area per lipid (nm^2)	0.76 ($\pm$ 0.02) [b]
	Lateral diffusion coefficient ($10^{-7} cm^2/s$)	1.84 ($\pm$ 0.31) [c]
Unprotonated PEI	Avg. end-to-end distance (nm)	2.37 ($\pm$ 0.82)
	Avg. R_g (nm)	0.97 ($\pm$ 0.16)
Protonated PEI	Avg. end-to-end distance (nm)	5.38 ($\pm$ 0.56)
	Avg. R_g (nm)	1.79 ($\pm$ 0.74)

[a] Experimental value: 2.68 nm [180]
[b] Experimental value: 72.4 $\pm$ 0.5 nm^2 [180]
[c] Experimental value: 1.37 $\times$ 10^{-7} cm^2/s [178]

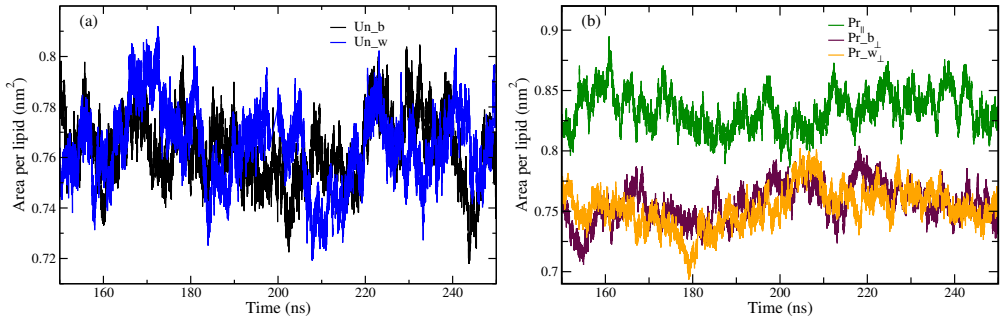

FIGURE 5.11: Area per lipid of the (a) unprotonated and (b) protonated PEI–bilayer–water system.

Similar to the structural properties, dynamical properties of lipid molecules could get altered due to perturbation. The presence of PEI in the vicinity of the head groups of lipid molecules and the interaction between them might slow down the lateral motion of lipid molecules. Therefore, we had calculated the lateral mean square displacement (in XY plane) (MSD) of P atoms of the leaflets. Last 100 ns of the production run trajectory was spilt in 10 equal interval comprising of 10 ns each. For each of these trajectories, lateral MSD in the xy plane were calculated. These plots were averaged and plotted in Figure 5.12. Lateral diffusion coefficient of lipids were computed from the slope of these plots and are tabulated in Table 5.1. For systems Un_b and Un_w, lateral diffusion coefficients were same. Although the diffusion coefficient for these two systems were smaller than the pure bilayer system but within the error bar with the pure lipid–bilayer system. Thus, the presence of unprotonated PEI had no effect or negligible effect on the lateral diffusion of lipid molecules. The diffusion coefficient for systems $Pr_{||}$, $Pr\_b_\perp$ and $Pr\_w_\perp$ were smaller (Table 5.1) than the pure and unprotonated systems. PEI chain being protonated interacted with the lipid molecules and slowed down the lateral movement of the molecules. Thus, the presence of unprotonated PEI shows negligible

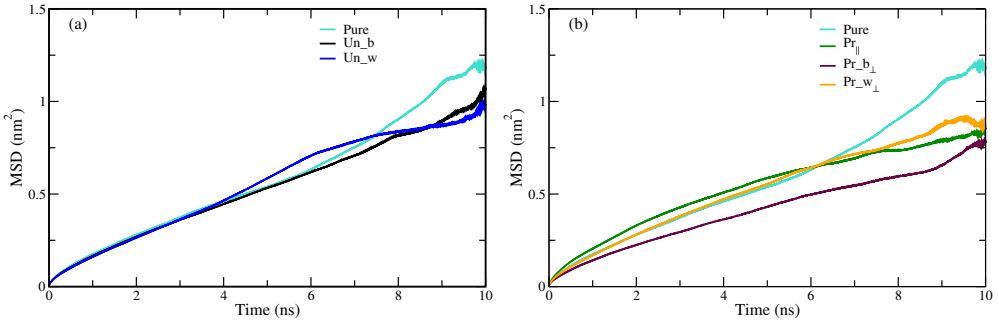

FIGURE 5.12: Lateral mean square displacement of the P atoms present in the single leaflet of the bilayer for (a) unprotonated and (b) protonated PEI–bilayer–water system.

effect on the structural and dynamical properties of bilayer while the protonated PEI slows down the motion of the lipid molecules and in particular, $Pr_{||}$ deforms the bilayer forming pore. PEI in both forms (unprotonated and protonated) settles near the interface of the lipid-bilayer system. However, protonated PEI was more bound to the bilayer head group because of the higher electrostatic interactions between the charged PEI atoms with the hydrophilic head group and water molecules present at the interface.

5.3.2 Structural properties of PEI in the bilayer

Properties of polymer also change due to its interaction with the bilayer. PEI may also take conformations which is biased due to the neighboring atoms as well as initial conformation and initial environment. To understand this we had calculated end-to-end distance and radius of gyration (R_g) of PEI as a function of time from last 100 ns of the production run trajectory and plotted in Figure 5.13. The average end-to-end distance for systems Un_b and Un_w were 2.82 and 0.84 nm respectively. Their respective average R_gs were 1.13 and 0.76 nm (see Table 5.1). Thus when PEI was placed in water region (at the beginning of simulation, system Un_w), it attained a highly coiled structure. In fact, this structure was slightly more coiled when compared with the pure PEI-water system (see Section 5.3.1 and table 5.1). From the distribution plots (see Figures 5.14(a) and 5.14(c)) of end-to-end distance and R_g, it was evident that unprotonated PEI in Un_b system scans a much wider region than Un_w system. Interestingly there were small overlaps of end-to-end distance and R_g distributions of Un_b and Un_w systems. In case of Un_w system, PEI was confined to a certain compact conformation. Similar end-to-end distance and R_g of PEI as a function of time (see Figure 5.13) and its distributions (refer Figures 5.14(b) and 5.14(d)) for the protonated PEI showed that PEI was confined to extended conformation in every system as in pure water. The average values are tabulated in Table 5.1. The elongation of the structure could be due to the electrostatic repulsion between the monomers of PEI which restricts the conformational

flexibility. However, the question remains open whether different starting (initial)

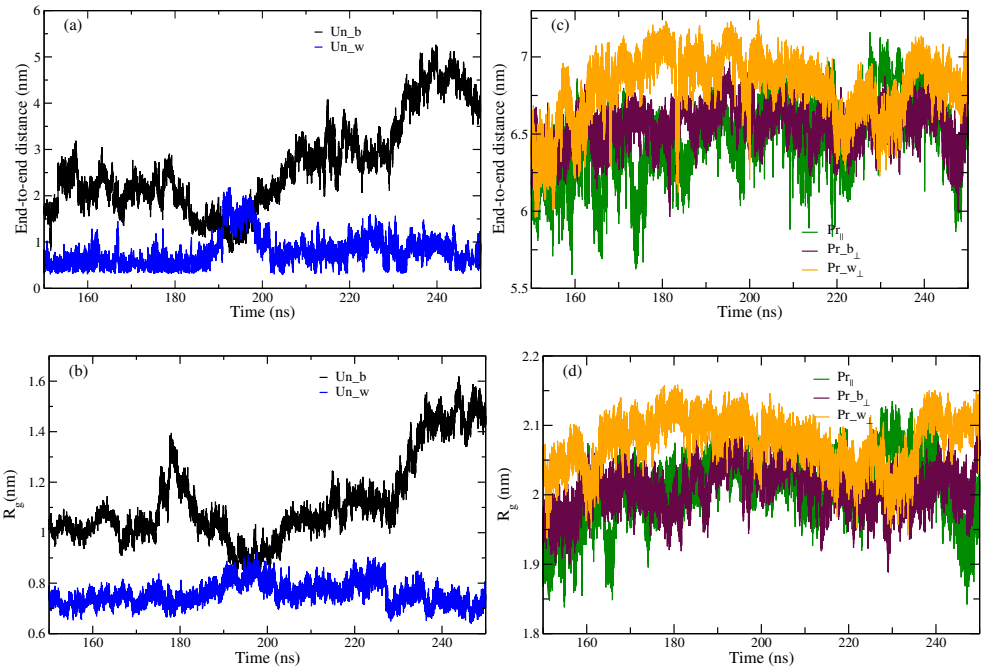

FIGURE 5.13: The variation end-to-end distance (a) and radius of gyration (b) for unprotonated. (c) and (d) are the end-to-end distance and radius of gyration for protonated system, respectively.

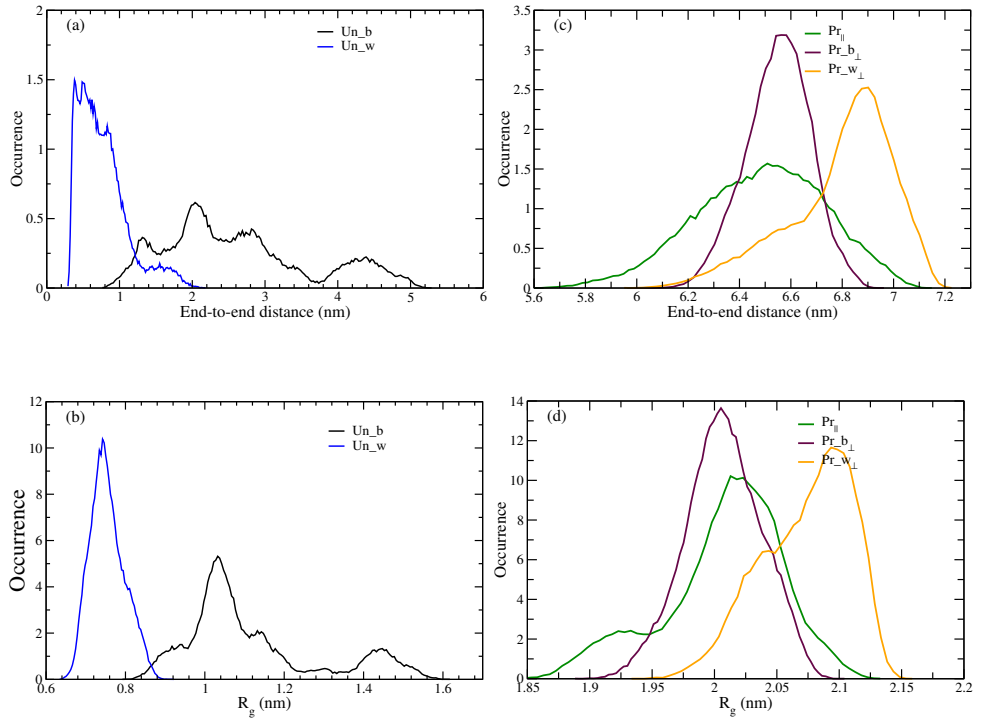

FIGURE 5.14: The distribution of end-to-end distances and radius of gyration of PEI for (a, b) unprotonated and (c, d) protonated systems. Its variation with time are shown in the Figure 5.13.

conformation of unprotonated PEI can results into different conformation of the chain and therefore can reside in different location of the bilayer. To investigate it further and statistically prove the result we had performed 6 more simulations starting from different conformation of unprotonated PEI initially positioned it in the hydrophobic (3 simulations, see Figure 5.4) and hydrophilic (3 simulations, Figure 5.6) region of the bilayer. These unprotonated chains of different conformation with R_gs 0.80, 1.10 and 1.25 nm were extracted from trajectories generated from a system where the PEI chain was simulated only in water. [179] These conformations when placed in the water region (above the interface) of lipid bilayer system, they settled in the interface by attaining equilibrium R_gs of 0.85, 0.80 and 0.87 nm, respectively (see Figures 5.6(b), 5.6(d) and 5.6(f)). These PEI chains on positioning in the bilayer region get expanded and in all three cases terminal groups of the PEI chains touched the bilayer water interface on both sides (see Figures 5.4(b), 5.4(d) and 5.4(f)). For 0.80 and 1.10 systems, the R_gs were approximately 1.2 nm and for 1.25 system the R_g was 1.4 nm (see Figure 5.16). So it is evident that the unprotonated PEI gains conformational flexibility in bilayer and expanded itself. However, PEI chains with same conformation in water preferred coiled conformation and sampled the interface region.

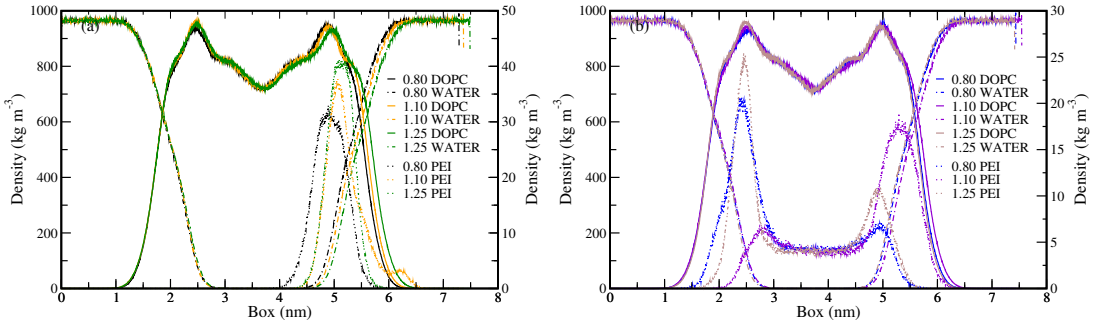

FIGURE 5.15: Partial densities for (a) PEI in water system and (b) PEI in bilayer system. The numerals in the legends shows the R_g of PEI at the start of the simulations. The density for PEI is shown in the right. In (a) PEI settles in the interface while in (b) PEI expands to the interface of both the ends.

5.3.3 Pore formation and water dynamics in the pore

PEI chain of the $Pr_{||}$ system, passes through the lipid region with its terminal groups touching the bulk water molecules on both sides of the bilayer (see snapshot Figure 5.8(a) and density profile of PEI molecule (Figure 5.10(b), green dashed lines)). The density profile plot of the water confirmed the presence of water molecules in the bilayer region (from 2.5 to 5.5 nm, see Figures 5.8(b) and 5.10(b)). Also the unprotonated PEI system when placed initially at the hydrophobic region of the bilayer, expands and the end touches the bulk water on both sides. Here, we did not see any transport phenomena

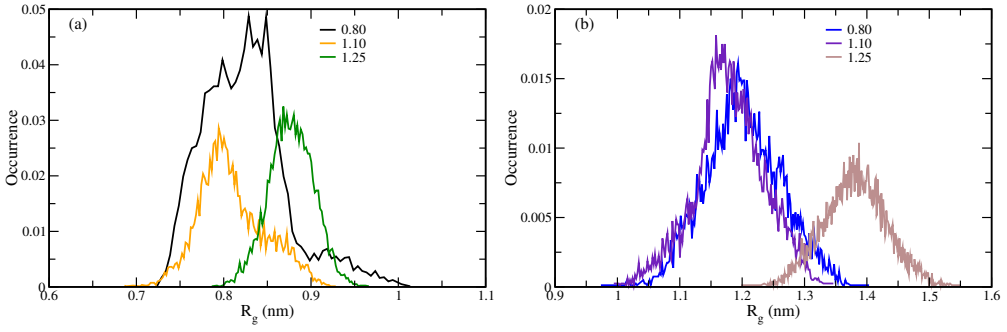

FIGURE 5.16: The distributions for (a) PEI in water system and (b) PEI in bilayer system. The numerals in the legends shows the R_g of PEI at the start of the simulations. R_g for the PEI in water system (a) is confined to 0.8 or 0.9 nm. For (b) the R_g of 0.80 and 1.10 systems are around 1.2 nm while for 1.25 system is 1.4 nm.

of water or ions along the polymer backbone. However, in case of protonated PEI, we did observe the transport of water and ions across the membrane. The increase in hydrophilicity of the PEI chain because of the charged amine groups had effectively helped in forming a pore. Similar pore formation was also observed by Groot et al. [181] in case of nanoscopic hydrophilic channels. Visualization of trajectory also revealed the presence of water molecules and ions across the bilayer region along the PEI chain. The pore radius we had calculated was 0.73 ± 0.13 nm, which is relatively small in size. [58] The variation of pore radius with simulation time is shown in Figure 5.17. Transport of water molecules along this bilayer-PEI channel and the dynamics of water were subjects to our investigation. The presence of multiple cationic moieties along the polymer chain provides a polar environment inside the lipid bilayer which was favorable for water molecules to penetrate deep in the hydrophobic region of bilayer. In our earlier studies, we have shown that how water can penetrate only to some certain extend of the hydrophilic head group region without any external perturbation. [105]

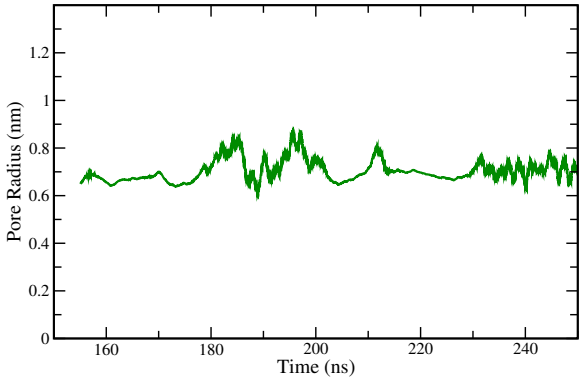

FIGURE 5.17: Pore radius as as a function of simulation time for the $Pr_{||}$.

We have calculated the flux of the water molecules passing through the pore formed in the $Pr_{||}$ system. The 100 ns trajectory (saved every 100 fs) was used for the calculation of

flux. We had divided the bilayer in two regions. Region I was the interior of bilayer whose Z-coordinate ranges from 3.60 nm to 4.50 nm while region II spanned from 2.10 to 3.60 nm and 4.50 to 5.90 nm. The boundaries for region I and region II had been chosen from the density profiles of water and PEI molecule (Figure 5.10(b)). Figure 5.18(a) shows the schematic diagram of the boundaries of the regions. The boundaries (extreme) of the region II were approximately merging with the bulk water. Water molecules present in the region I were tagged and stored every frame. They were counted if they crossed region II in the subsequent frames and were simultaneously untagged. Such counts were recorded for every frame. It was also possible that none of the tagged water molecules (present in region I) crossed region II for some of the frames. Then the count for these frames was set to 0. It was also possible that a water molecule once in region I, crossed region II and re-enter region I. All such incidences were considered as distinct and the water molecules were tagged again. The counts were averaged for every nanoseconds and plotted in Figure 5.18(b). At an average of around 150 water molecules/ns passes through the channel. Ions can also flow through this channel. However, only few ions were added to neutralize the system. So because of poor statistics we did not analyze and report the flow of ions.

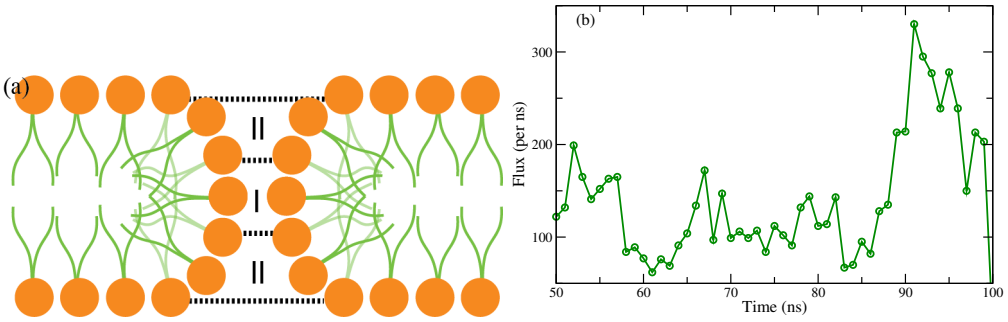

FIGURE 5.18: (a) Schematic of the different regions in the interior of bilayer, (b) Flux defined as the number of water molecules passing through the pore to the bulk water region for the $Pr_{||}$ system.

Electrostatic interaction between water and protonated PEI favors the water molecules to reside in the pore for some time. But we had observed that these water molecules also flow in and out from the channel. Therefore, residence time for the water molecules along the polymeric chain i.e., in the interior of the bilayer for system $Pr_{||}$ was computed. Only those water molecules were considered that were within the distance of 1.5 nm from the polymer backbone and present in the interior of bilayer (by defining Z-coordinate boundaries between 2.70 nm and 5.40 nm, Figure 5.10(b)). The number of water molecules in the bilayer region which satisfied the above conditions as function of time is shown in Figure 5.19(a). We observe that at an average of around 250 water molecules are present in the hydrophobic region in every frame. The methodology for calculating the residence time was same as reported in the article by Choudhury et al. [179] The

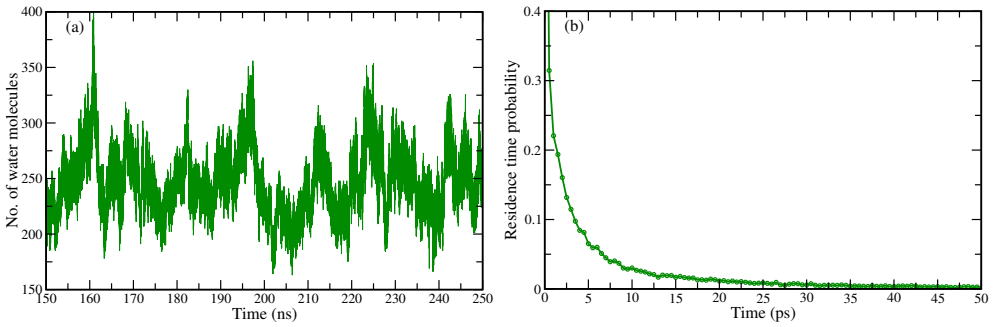

FIGURE 5.19: (a) Total number of water molecules present as a function of simulation time in the hydrophilic pore formed of the $Pr_{||}$ system. (b) Residence time probability of the water molecules present in the pore.

condensed trajectory was spilt in four intervals e.g., 0 - 1 ns, 1 - 2 ns, 2 - 3 ns and 3 - 4 ns (0 - 1 ns was not considered for calculation of residence time). In each of the frames, unique water molecules (which satisfied the criteria of lying within the distance of 1.5 nm from the polymer backbone and present in the interior of bilayer) were recorded. They were tracked for subsequent time (frames). If the water molecule were continuously not found for 2 ps, the time was recorded as the residence time. The residence time plot from these split trajectories were averaged and plotted in Figure 5.19(b). The plot was normalized with the residence time at 0 ps. Since the nature of the plot was bi-exponential, it was fitted with a bi-exponential function, Equation (5.2) with relaxation times τ_f and τ_s and a_f and a_s are the, respective, amplitudes of the fast and slow relaxation components. The values of the fast and slow relaxation with their, respective, components are tabulated in Table 5.3. There exists heterogeneity in the system because of the presence of two distinct molecular species – one with slow and the other one with fast relaxation [143], in the water molecules along the polymer chain, in the bilayer region.

$$y = a_f e^{-t/\tau_f} + a_s e^{-t/\tau_s} + a_0 \tag{5.2}$$

The relaxation of these water molecules were slower when compared to the unprotonated

TABLE 5.3: The Relaxation Coefficients (a_f and a_s) for the Fast and Slow Relaxation Times (τ_f and τ_s, respectively) for the P|| System

	a_f	τ_f (ps)	a_s	τ_s (ps)
$Pr_{||}$ system	0.78	0.25	0.24	4.31

PEI in water system (1^{st} solvation shell). [179] This slow relaxation may be attributed to the stronger H-bond network of the protonated groups of PEI in water (lipid–PEI system). These relaxations were similar to the protonated PEI in water system. [179] The higher τ_f, i.e., slower motion than that of the protonated (1^{st} solvation) system was

due to the restricted motion of the water molecules in the bilayer region. This motion was along the polymer chain.

The mean square displacement (MSD) of water molecules present along the polymer chain was also computed and plotted in Figure 5.20. From the residence time plot (Figure 5.19(b)), only those water molecules were considered which reside for a minimum of 20 ps. The detailed computation have been described elsewhere. [179] MSD was calculated by using the condensed split trajectories. The individual MSD plots from these split trajectories were averaged and plotted in Figure 5.20. The diffusion coefficient obtained from the slope was 1.63×10^{-5} cm^2/s. Inset shows the semi-log plot of the MSD of water molecules present in the interior of bilayer in the sub-picosecond region. This plot was fitted to $dr^2 = \alpha_0\, t^{\alpha_1}$, where the value α_1 indicated the type of diffusion followed by the water molecules. [147] A system follows a ballistic or Fickian diffusion if α_1 is 2 or 1, respectively. For this system, α_1 was 1.8. In this case, the diffusive motion is much more like the ballistic, i.e., the confined water moves in coordination.

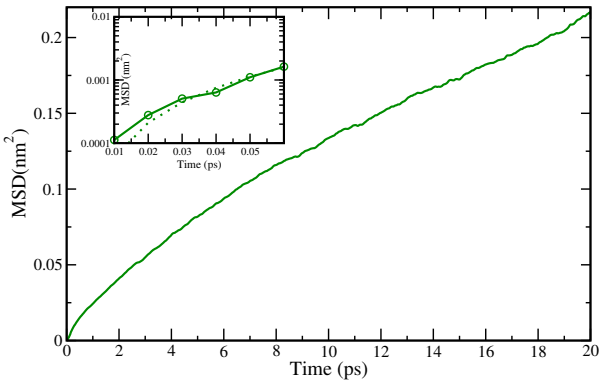

FIGURE 5.20: The mean square displacement of water molecules present in the pore. Inset shows the semi-log plot for the mean square displacement at the sub-picosecond scale.

5.3.4 Orientation of lipid molecules around the pore

The incorporation of PEI in lipid–bilayer system for $Pr_{||}$ system had created a channel which leads to the change in the orientation of lipid molecules. This change had been visually observed in the trajectory. It is schematically shown in Figure 5.18(a). The orientations were such that the lipid molecules tilt or orient themselves along the PEI chain. To quantify the change in orientation we had calculated the orientation of lipids along the Z-axis. We had defined three groups; Head, Middle and Tail, for lipid molecules as represented in Figure 5.1. Middle and Head groups comprise the atoms of the phosphate and choline moiety, respectively and the tail group consisted of all the remaining atoms up to the start of unsaturation (see Figure 5.1). The remaining atoms

were not considered as they were spread out because of unsaturation in hydrocarbon moieties. The center of mass (COM) for each of these groups were computed for every frame. An angle between the line formed by the COM of middle and tail groups with the XZ-plane (perpendicular to the bilayer plane) were computed for every lipid molecules in each frames. These angles were classified as *vicinity* or *far* angle on the basis of the position of the phosphorous (P) atom with respect to PEI chain. If the P atom of a lipid molecule falls within the distance of 5 Å (see Figure 5.21, radial distribution of P atoms of DOPC and backbone atoms of PEI had minima of the largest peak at 5 Å) from the PEI backbone, then the angles computed, were termed as *vicinity* angle. If the separation

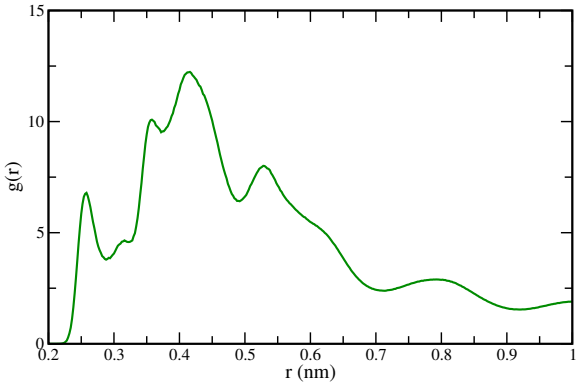

FIGURE 5.21: Radial distribution of PEI atoms with the P atoms of the lipid molecules.

of P atom of a lipid from the PEI backbone was greater than 5 Å, then the angle was termed as *far* angle. These angles were computed for last 100 ns of the trajectory and their distributions are plotted in Figure 5.22(a). Similar distributions were computed for the angle formed between the COMs of Head, Middle and Tail groups (as defined above) for each of the lipid molecules and are plotted in Figure 5.22(b). These plots were

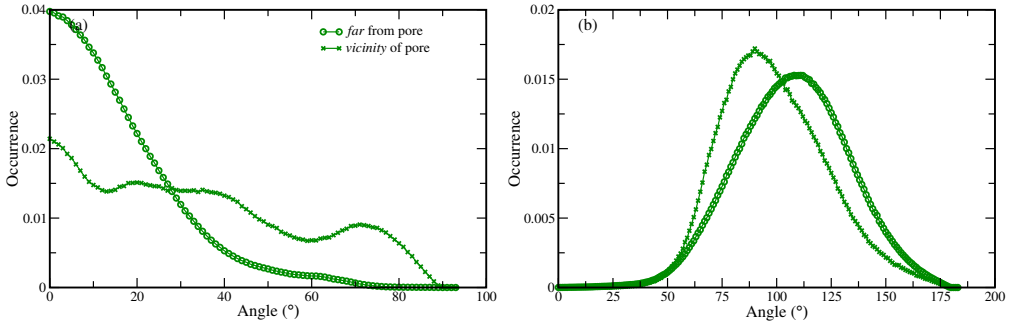

FIGURE 5.22: Orientation of lipid molecules in the vicinity of pore and away from it. (a) shows the distribution of the angle formed between the center of mass of the middle and tail group and the XZ-plane. (b) shows the distribution of angles formed with the head, middle and tail moieties.

normalized by the total number of lipids in each sections (i.e., *vicinity* and *far*). From Figure 5.22(a) it is noticeable that the lipids those are away from PEI prefers to stay

around 0° and has a less probability for higher angles. While for the lipids staying in the *vicinity* of PEI, in addition to staying around 0°, it also prefers to stay around 42° and 75°. The conformations of lipids within the *vicinity* of PEI are different as phosphate moiety are tilted and it makes the pore hydrophilic. Figure 5.22(b) shows the distribution of angle formed by Head, Middle and Tail groups for each of the lipid molecules. We see that the lipids which are at a distance > 5 Å from the PEI backbone, mostly stays around 109° while those in the *vicinity* prefers to stay around 90°. The presence of PEI also had an effect on the tilting of head group which eventually provides a hydrophilic channel and water can flow through it.

5.4 Conclusions

Lipid bilayer with embedded polycationic polymer, PEI at two different protonation states was simulated by all atomistic MD. We had studied the effect of PEI on the lipid bilayer system. In addition to pure lipid-bilayer system, bilayer systems with unprotonated and protonated PEI were separately studied. Unprotonated PEI always settled at the interface, when it was placed at the hydrophilic region (in water) at the start of the simulation. When it was positioned at the hydrophobic region, the PEI chain gains conformational flexibility and expands while sampling across the membrane. At the hydrophilic region, PEI is more coiled as compared to when placed at the hydrophobic region. In case of protonated PEI, it settles at the interface, irrespective of if it was placed at the bilayer or water region at the start of simulation. Exception was observed for the $Pr_{||}$ system where PEI was parallel to the Z-axis. The presence of unprotonated PEI does not significantly perturb the bilayer properties; whereas protonated, being charged, interacts to a greater extend with the interfacial molecules. This interaction resulted the reduction of lateral diffusion of the lipid molecules.

The unprotonated PEI though spans across the membrane in most of the cases when it was placed in the bilayer, no disruption in the bilayer has been observed in the simulation time scale. The protonated PEI in the $Pr_{||}$ system disrupts the structural integrity of lipid bilayers. The presence of multiple cationic moieties along the polymer chains provides a favorable polar environment inside the lipid bilayer to the water molecules to penetrate across the bilayer. This eventually leads to the formation of hydrophilic pore where water molecules and ions can flow through it. These observations are also supported by the experiment studies by Helander et al. on Gram-negative bacteria. [40] These water molecules are homogeneous and they ballistically diffuse along the pore with the diffusion coefficient of 1.63×10^{-5} cm^2/s. We have also observed the inclination of the lipid molecules towards the pore. This new insight of the distortion of lipid bilayers can

be valuable to understand the effect of concentration of PEI on bilayer which eventually may help in designing PEI as better gene delivery vector.

Chapter 6

Coarse-Graining of polymer: Importance of torsions in coarse-grain simulations

6.1 Introduction

Polymers are long chained macromolecule which shows a wide variety of behaviors depending upon its density, molecular weight and temperature. They are studied both experimentally and computationally. The atomistic molecular dynamic (MD) simulations can predict the structural and dynamical properties of the polymers with low molecular weights. These predictions are, though, restricted to the smaller length and time scales. As the characteristic length and time scales are very broad for the polymeric systems, it is not feasible to equilibrate these systems with higher molecular weights using atomisitic simulation. [75] On the mesoscale level, coarse-grained (CG) molecular dynamics have proven to be very efficient means to study the long, entangled polymer systems. Thus, to simulate such system comprising broad spectrum, a multiscale simulation approaches are being developed. Multiscale simulation is a hierarchy of simulation approaches to treat systems at different levels of resolution. These different levels of resolution can be linked using: (*i*) Bottom-up approach, where information at the finer (atomistic level) scale, informs the model at the larger (coarse-grained) scale. Here, generally one develops a model that is easier to simulate and that can also reproduce the correct physical behavior as that of the atomistic scales.

The study of polymeric melt system by computer simulation requires one to equilibrate the chains very long. The equilibration times for the branched polymer melts are even larger. [182] The coarse-grained molecular dynamics (CGMD) simulation technique is an

efficient way to access the longer time and larger length scales, which are not accessible by the atomistic or united atom model simulations. [125, 183] CG simulation is accomplished by grouping the atoms into fewer interaction sites (forming super atoms). Thus, to study the polymeric system, it is necessary to reduce the number of degrees of freedom and simulate it in the larger length scale, using the coarse-grained (CG) simulation. Such CG model does reduce the degrees of freedom and they must preserve the interaction details necessary to reproduce the chemical features of the system. [66] CG method can be broadly divided into two classes based on the procedure used to parameterize the force field acting among the super atoms. Structure based techniques like Boltzmann inversion [90], Iterative Boltzmann inversion (IBI) [69] and Inverse Monte Carlo [94] are employed in CG simulations to obtain the CG potentials. Apart from structure based approaches, force matching method where the CG potentials are generated such that the average force on the super atoms in the CG system matches to that of the fine grain system. [94, 127]

The CG simulation of polymer melts using the Boltzmann inversion was first proposed by Tschop et al. [90] They coarse-grained polycarbonates by considering two beads per repeat unit, one on the geometrical center of isopropylidene group and the other in the geometrical center of carbonate group. This 2:1 mapping scheme could lead to producing artifacts in the melt structure near the interface. [66, 184] This effect was nullified by changing the mapping scheme from 2:1 to 4:1. [184] Reith et al. used the Boltzmann inversion technique to coarse-grain poly(vinyl alcohol) (PVA) and poly(acrylic acid) (PAA). [68] Here they used the simplex optimization techniques to optimize the non-bonded parameters. [185, 186] Later Reith et al. iteratively used the Boltzmann inversion methodology to refine the effective interaction between the CG beads (super atoms) of Poly (isoprene). [69] Poly (isoprene) in the melt and in solution (in cyclohexane) was also coarse-grained and studied using the IBI methodology. [69, 74, 187] Faller et al. could generate a reliable model whose static properties were comparable with the experiments. [187] Bisphenol-A-polycarbonate has a history of being the first polymer upon which the Boltzmann inversion methodology was successfully tested. [90] Later it was coarse-grained [67, 72, 184, 188] using the Boltzmann inversion technique with differing in the mapping scheme of CG beads. Coarse-grained methodology has also been used for cellulose [189], vinyl polymers, [87, 190] polystyrene, [73, 74, 76, 191–198] polyethylene, [199] polyamide-6,6 [191, 196, 200] and its confinement between graphene sheets [201], liquid crystal [202], peptides [78, 86], lipids [203] and ionic liquids [204] involving the optimization of potentials using the IBI methodology. Poly (styrene-b-butadiene), a diblock copolymer, has also been simulated using IBI optimization for CG potentials. [205]

The structure based coarse grained MD simulations using the IBI methodology involves the optimization of bonded and non-bonded potentials. The bonded interaction includes the bond, the angle and the dihedral potentials. While the non-bonded term includes the interactions between the beads beyond 3 bonds (*exclusion* 3) or 2 bonds (*exclusion* 2). Generally one considers *exclusion* 2 in their simulations when the torsions are not considered. Researchers usually neglect the torsional components in a CG simulation of the polymeric systems. [68, 72, 74, 87, 90, 184, 187, 188, 190, 191, 193, 196, 200, 201]. When Reith et al. simulated the long chain of PAA with the CG potentials without including the torsions, the chains collapsed. In these collapsed states, the radius of gyration (R_g) was consistent with the atomistic data. So, to redistribute some degrees of freedom, they incorporated the torsion potentials and found that the inclusion of torsion straightened the chain. There was a marginal increase in the average R_g (1.24 ($\pm$ 0.05) nm when torsions were excluded to 1.25 ($\pm$ 0.05) nm when torsion were included). The distributions of torsional angles were not flat for PAA as in PVA. [68] In few reports, the torsion distributions were almost flat, or the torsional barrier was weak, so they have neglected the potentials. [72, 90, 184, 187, 188, 196, 200] Karimi-Varzaneh et al. have neglected the torsion potential as they were flat, but they have considered non-bonded interaction between the beads separated by 3 bonds (*exclusion* 2). [200] Qian et al. showed that the temperature transferability of CG potentials does not does not upon the inclusion of torsional potential. [195] Thus, much of the understanding regarding the inclusion or *exclusion* of torsions in CG simulations of polymer are still naive and a deeper insight is required to understand the role of torsional potentials for the simulation of polymers. In this chapter, we highlight the importance of torsions in the CG simulations of polymers. For the test case, we simulated Bisphenol-A polycarbonates melt (a widely studied and technically and technologically important polymer) with various molecular weights (3-mer, 5-mer and 10-mer) and a alkane melt (dodecane). Polycarbonates provides with inherent built-in aromaticity while dodecane is an aliphatic chain. We also investigated in which condition are the torsions safe to discard and when do we need it.

In the next section we describe the model and the coarse grain strategies and the simulation details. This is followed by the methodology imposed in the CG simulations and its technical details. Then we discuss the findings in the result and discussion section. We close with the conclusions.

6.2 Models and coarse-graining strategies

In this and the subsequent chapters, we study the the mesoscale models of polycarbonate melts. We have modeled and simulated 3-mer, 5-mer and 10-mer polycarbonate melt.

This chapter is devoted on the investigation of the importance of CG torsions for polymer melts and the chapter 7 discusses the possibility of *scalability* of CG potentials to the higher molecular weights. The complete strategy is shown in Figure 6.1. In this

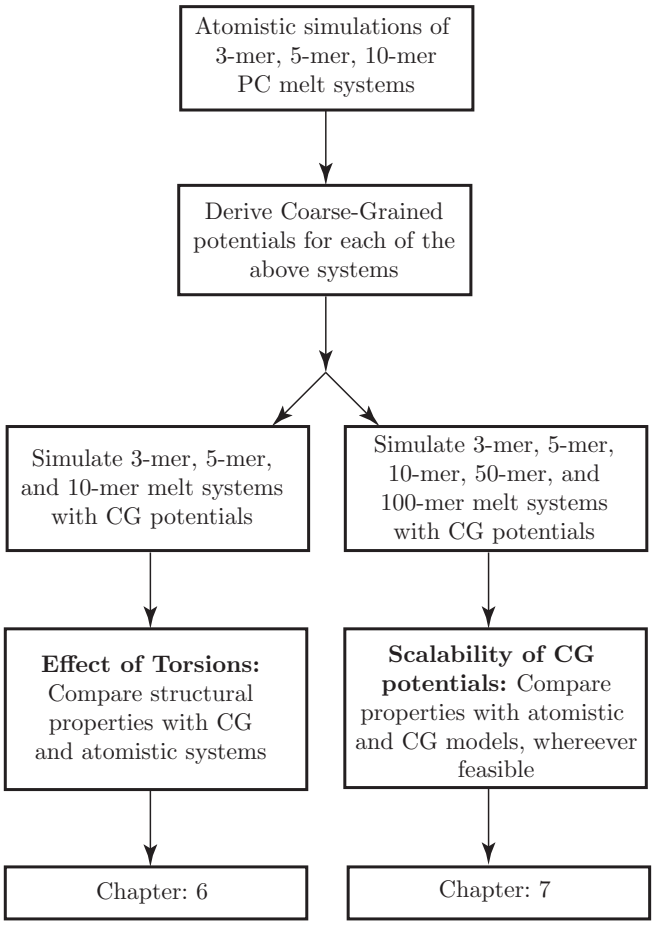

FIGURE 6.1: The flow chart depict the strategies involved to study the effect of torsion and *scalability* of CG potentials on polymer melts.

chapter, the mesoscale models for 3-mer, 5-mer and 10-mer polycarbonate melt have been developed. The strategy to build the mesoscale models requires the atomistic simulation results as a basis. Therefore in the following section we give some information of the atomistic simulations and then the methodology for the development of coarse grained simulations.

6.2.1 All atom simulations

All atomistic simulations of polycarbonate melt were performed for three different chain lengths: 3-mer, 5-mer and 10-mer. The force field parameters and simulations details for polycarbonate melt system were adapted from Chakraborty et al. [206] All bonds were constrained during the simulation using LINCS [119] algorithm. Reaction field [115]

method was used for computing the electrostatic interactions with dielectric constant of 3.5 beyond the cut-off of 1.2 nm. The systems were simulated at 480 K and 1 Bar. Berendsen thermostat with 0.1 ps coupling time constant and Berendsen barostat with coupling time constant of 1.5 ps were used, respectively, for temperature and pressure coupling. [122] The simulations were performed using Gromacs 4.0.7. [130] 80 chains of 3-mer were packed in a box and was simulated for 90 ns. Last 40 ns of the trajectory was analysed for the 3-mer system. The density obtained from the last 5 ns of the trajectory was 1061 ± 4.2 kg m^{-3}. 100 chains of 5-mer and 50 chains of 10-mer were also packed and simulated for 100 ns and 80 ns, respectively. Their respective densities (from the last 5 ns of the trajectories) were 1086 ± 2.8 and 1102 ± 2.5 kg m^{-3} (see Table 6.1). These atomistic simulations serve as a reference for the CG simulations.

6.3 Coarse-grained simulations

6.3.1 Methodology

We have employed the iterative Boltzmann inversion method (IBI) to obtain the CG potentials from the atomistic simulation. We used VOTCA [132] (1.3-dev) package for the preparation and refinement of potentials for the CG simulations. The CG simulation temperature was same as that of atomistic simulations (i.e., 480 K).

6.3.1.1 Mapping scheme

The mapping scheme is shown in Figure 6.2. There are 5 different types of beads (A, B, C, D and E) and each of which is represented at the center of mass of atoms comprising them. This 4:1 mapping scheme is different from the reported ones where the CG beads for carbonate and isopropylidene are the backbone carbon atoms, while for the phenylene subunits the beads lie on the straight line between the carbonate and isopropylidene beads. [72, 184, 188]

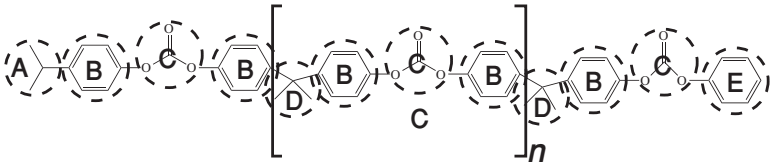

FIGURE 6.2: The mapping of polycarbonate is shown. CG beads were represented by the center of mass of corresponding atoms.

6.3.1.2 Derivation of CG potentials

With this mapping scheme, a 3-mer chain consisting of 101 atoms was mapped to 12 CG beads. The 3-mer melt of 80 chains consisted of 960 CG beads. Last 20 ns of atomistic 3-mer melt were converted to the CG trajectory. These trajectories act as a reference trajectory for coarse-grain simulations. From this reference trajectory, bead-bead bonded and non-bonded distributions were computed. There were 13 bonded (see Figures 6.3(a) to 6.3(c), black lines) and 15 non-bonded distributions (see Figure 6.4, black lines). These distributions ($g^{target}(r)$) act as the target distributions for the refinement of CG potentials. The non-bonded distributions were inverted using the Boltzmann relation (Equation (2.29)) to obtain a guess potential (V_0), where k_B is the Boltzmann constant and T is the simulation temperature. With these guess potentials, CG beads were sampled for 10 ns with the time step of 5 fs. Thereafter, the pair distributions were computed and compared with the reference distributions using Equation (2.30), where g_i refers to the pair distribution at iteration i. If the merit function, f_{merit}, (computed according to Equation (2.30)) was less than 0.003, we stopped the refinement of potentials. We say that the potential is converged. Otherwise, the potential was updated (V_{i+1}) using relation Equation (2.31), where V_i is the potential obtained at the i^{th} iteration step. We updated one interaction at each iteration. For example, at iteration 1, after the sampling was performed by the guess potentials, we then updated one of the interaction potentials (say AA), rest other interactions were untouched. At iteration 2, the updated AA potential was the input for its interaction and the after sampling, the AB potential was updated. For iteration 3, the updated AA (updated at iteration 1) and AB (updated at iteration 2) potentials were the input for these interactions and after sampling, AC potential was updated. In this way, only one interaction potential was refined in each iteration. The iteration continued, till the convergence criteria was achieved ($f_{merit} < 0.003$) for each interaction. In this way, all the non-bonded interaction potentials were refined. Similar, iterative methodology was followed for the refinement of bonded potentials. Only the stretching and bending potentials were refined. The bonded distributions were Boltzmann inverted (Equation (2.29)). This potential was used as the guess potential for the sampling of CG beads. Upon sampling, the convergence of the bonded distribution was checked with that of the target distribution (Equation (2.30)). We iterated till the convergence was achieved ($f_{merit} < 0.003$). Figures 6.3(a), 6.3(b) and 6.4 shows convergence of refined distributions (green lines) with the target (black lines) distributions for the bonded (bonds and angles) and non-bonded distributions, respectively. The match of the distributions from the refined potentials with the target distributions are within the line width. We did not refine the torsional potentials. The refinement of CG bonded and non-bonded potentials were carried out for the 3-mer melt system.

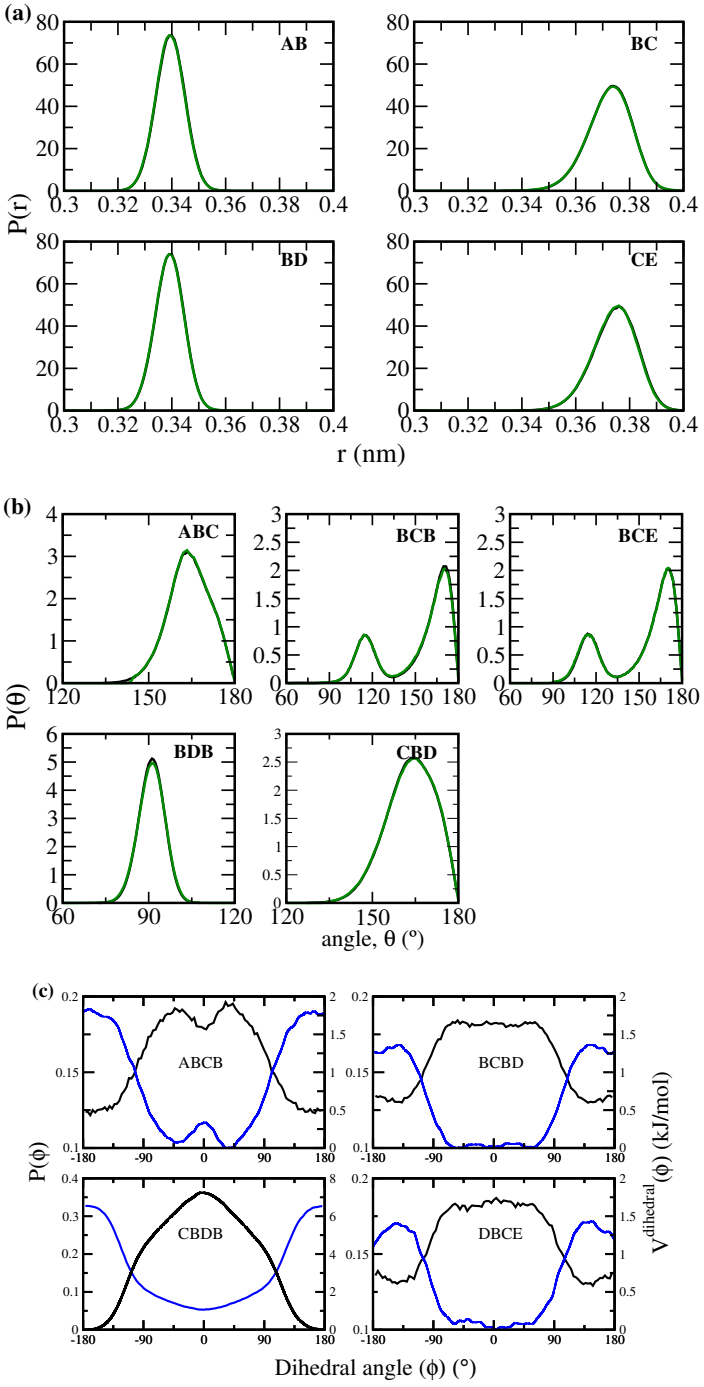

FIGURE 6.3: The distribution of bonded interactions are plotted. Reference distributions are shown as black lines. Green lines corresponds to the distributions obtained from the corresponding optimized potentials (using IBI methodology). The match of the distributions from the refined potentials with the target distributions are within the line width. Blue line shows the potential obtained by Boltzmann inversion (see Equation (2.29)). (a) shows the bond distribution. (b) shows the angle distribution and (c) shows the torsional distribution and potential.

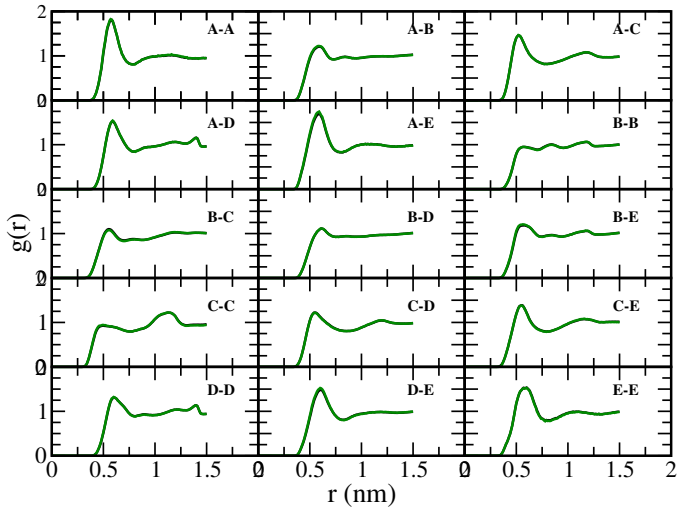

FIGURE 6.4: The RDF of non-bonded interactions when *exclusion* 3 is considered. Reference distributions are shown as black lines. Green lines corresponds to the distributions obtained from the corresponding optimized potentials. The match of the distributions from the refined potentials with the target distributions are within the line width.

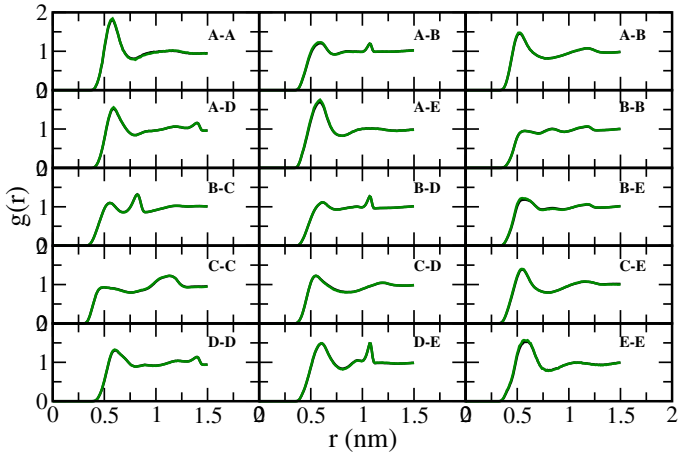

FIGURE 6.5: The RDF of non-bonded interactions when *exclusion* 2 is considered. Reference distributions and the distributions obtained from the optimized IBI potentials are shown as black lines and green lines, respectively. The match of the distributions from the refined potentials with the target distributions are within the line width.

6.3.2 Simulation details

With these refined potentials, 1 µs CG simulation was performed for 3-mer, 5-mer and 10-mer melt systems. The CG interaction potentials obtained from the 3-mer melt system was used to simulate 5-mer and 10-mer systems. We did not generate separate potentials (refined) for 5-mer and 10-mer system. The initial CG structure for 3-mer, 5-mer and 10-mer systems were obtained by mapping the respective atomistic configuration. Table 6.1 lists the CG system size for 3-mer, 5-mer and 10-mer systems. Two sets of simulations were performed where (a) interactions between beads beyond 3 bonds were considered as

non-bonded (we term as *exclusion* 3) and (b) interactions between beads beyond 2 bonds were considered as non-bonded (we term as *exclusion* 2). For both the *exclusions*, the non-bonded interactions were separately refined. The bonded interactions and thus its distributions remains same for both the *exclusions*. The bonded distributions are shown in Figure 6.3. The RDFs of non-bonded interactions for *exclusion* 3 and 2 are shown in Figures 6.4 and 6.5. As we reduce the degrees of freedom by mapping a collection of atoms (see Figure 6.2), we can scale up the integration time compared to the atomistic ones. We used 5 fs as the integration time step for all the simulations. NVT ensemble was used with a temperature of 480 K. The temperature was coupled with v-rescale [123] algorithm with coupling constant of 1.0 ps. The volume of the simulation box was same as that of the configuration written at the end of the corresponding atomistic simulation. The constant volume constraint imposed correct density to each of the studied systems. Gromacs 4.6.3 [130] was used as a simulation engine program to simulate the systems for 1 µs. The trajectory was saved every 25 ps. Last 500 ns of the trajectory was used for the analysis.

TABLE 6.1: Lists the size of polycarbonate melt which have been simulated atomistically and coarse-grained. Density were computed from the atomistic trajectory, which were maintained for the CG simulations.

System	No. of Chains	No. Atomistic Atoms	No. of CG beads	Density (kg m^{-3})
3-mer	80	8080	960	1061 ± 4.2
5-mer	100	16700	2000	1086 ± 2.8
10-mer	50	16600	2000	1102 ± 2.5

6.3.3 Results and discussions

The size of the polymer chain in a melt can be explored by computing the end-to-end distance and the radius of gyration (R_g). End-to-end distance is the distance between the two terminals of a polymer chain. It is different for each configuration of the chain. The square of radius of gyration, R_g^2, Equation (6.1), is defined as the mean square of the distance between the bead, $\vec{r}_i$ and the center of mass, $\vec{r}_{CM}$, of the chain. $\vec{r}_i$ is the position of the bead i and $\vec{r}_{CM}$ is the center of mass of the beads comprising the polymer chain.

$$R_g^2 = \frac{1}{N}\sum_{i=1}^{N} < (\vec{r}_i - \vec{r}_{CM})^2 > \tag{6.1}$$

R_g for each polymer chain for the last 500 ns in the CG melt was computed and its distribution is plotted in Figure 6.6. Each subfigure of the Figure 6.6 consists of three plots. Black lines represent the R_g from the atomistic simulations, green and red lines represent the R_g from the CG simulations where the *exclusion* for the non-bonded

interactions were 3 and 2 respectively. In these CG simulations, the torsional potentials

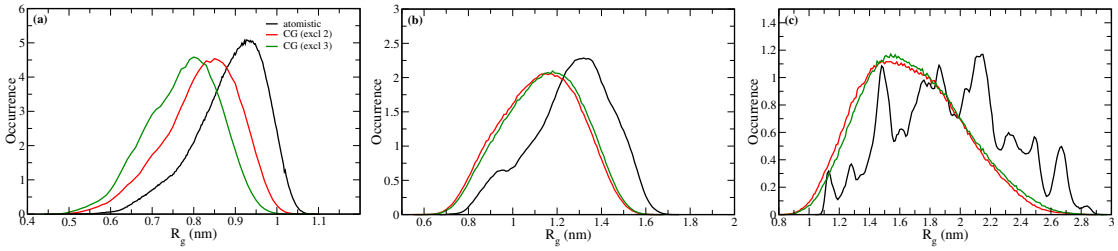

FIGURE 6.6: Distribution of R_g. Black, green and red lines corresponds to the atomistic, CG simulation with *exclusion* 3 and CG simulation with *exclusion* 2, respectively. (a) 3-mer, (b) 5-mer and (c) 10-mer systems.

were not considered. The atomistic ones refers to the reference trajectory (see the Methodology section), which was mapped as the CG bead trajectory from the atomistic trajectory. The distribution of R_g from the atomistic simulation peaks at 0.94 nm while for CG simulation (*exclusion* 3), it drops to 0.80 nm. Since we have neglected the 1-4 torsional potential for the *exclusion* 3 simulations, we have now considered it in the non-bonded interactions in *exclusion* 2 simulations. For *exclusion* 2 simulations, we find a slight increase in R_g (0.85 nm, red line) as compared to that of *exclusion* 3 (0.80 nm, black line). Thus, both the plots (excl 2 and excl 3) have distributions at the smaller R_g. For 5-mer system, R_g distribution from the atomistic simulation peaks at 1.32 nm while for *exclusion* 2 and 3, it is 1.2 nm. R_g distributions for both the *exclusions* are similar and it is smaller than that of the atomistic one. When we consider the 10-mer systems, the polymer samples a wider range of R_g for atomistic system. As the polymer chain length increases, its equilibration time also increases. Thus, we see many peaks for the atomistic simulation. The corresponding coarse-grained simulation R_gs peaks at 1.51 nm. Thus, we see that on ignoring the torsional potential(s), R_g is almost 9% off as compared with the atomistic simulations.

The end-to-end distributions also show a similar behavior (see Figure 6.7). The 3-mer atomistic system's end-to-end distance peaks at 2.8 nm while for *exclusion* 2 and 3 it is 2.5 nm and 2.30 nm respectively. For the 5-mer system, peak at 3.75 nm is obtained for the atomistic system. But the CG simulation end-to-end distance peaks at 3.0 nm. For 10-mer system, we have peaks at 3.2 (atomistic), 4.0 nm (*exclusion* 2 and 3). The end-to-end distance is decreased for the CG simulations with *exclusion* 2 and 3.

The dihedral potential for the CG simulation computed from the reference trajectory is shown in Figure 6.3(c). Here, we see that for the BCBD and DBCE dihedrals are flat in the region -60° to +60°. Thus, these dihedrals does not posses any structure and are safe to be neglected for the CG simulations. While ABCB dihedral has a very subtle barrier, which can be easily overcome at the studied temperature. Thus, this

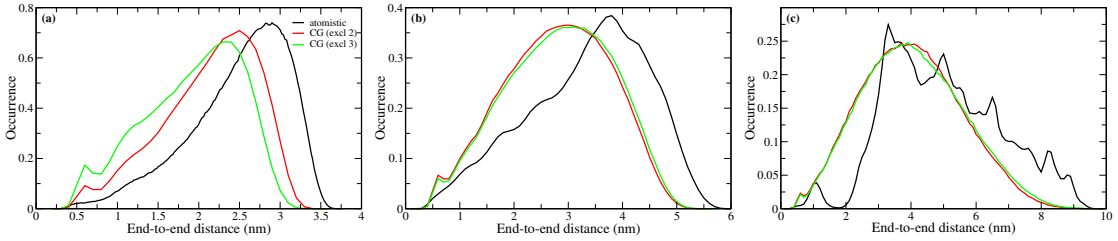

FIGURE 6.7: Distribution of end-to-end distance. Black, green and red lines corresponds to the atomistic, CG simulation with *exclusion* 3 and CG simulation with *exclusion* 2, respectively. (a) 3-mer, (b) 5-mer and (c) 10-mer systems.

dihedral can also be neglected. However, dihedral CBDB do posses structure and has a minima at 0° and maxima at -180° and +180°. We have considered this dihedral for the simulation of 3-mer, 5-mer and 10-mer CG polycarbonate systems. We have used the refined bonded (bonds and angles) and non-bonded CG potentials generated from the 3-mer system (*exclusion* 3's effective potential). In addition, we used CBDB dihedral potential. We have simulated these melt systems (3-mer, 5-mer and 10-mer) for 1 µs and the simulation details are same as the previous simulations. We have computed the R_g for each chain in every frame and then plotted its distribution in Figure 6.8. For 3-mer melt system, we see that the R_g deviates very slightly when CBDB dihedral is considered. Similar observation is made for the 5-mer melt system. For 10-mer system, the highly probable region of the R_g from atomistic simulation is captured very well in the CG simulation when CBDB dihedral was considered. Similar observations can be seen in the distributions of end-to-end distance (see Figure 6.9). This highlights the importance of the consideration of dihedral in the coarse-grain simulations. The chain dimension of

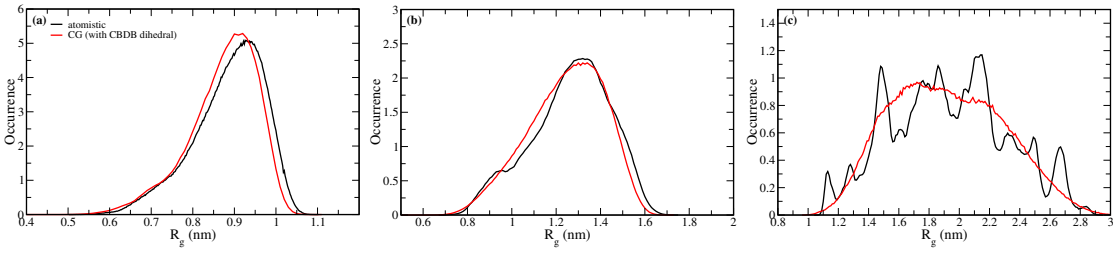

FIGURE 6.8: Distribution of R_g when the torsional CBDB potential was incorporated in the CG simulation. Black, green and red lines corresponds to the atomistic, CG, respectively. (a) 3-mer, (b) 5-mer and (c) 10-mer systems.

a polymer can be characterized by the radii of gyration parallel to the individual axes

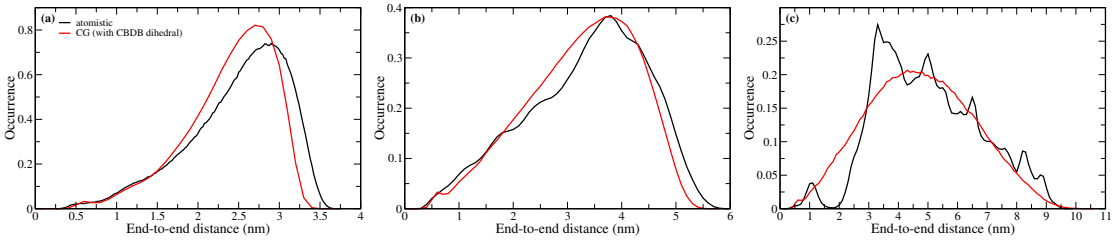

FIGURE 6.9: Distribution of end-to-end distance when the torsional CBDB potential was incorporated in the CG simulation. Black and red lines corresponds to the atomistic and CG, respectively. (a) 3-mer, (b) 5-mer and (c) 10-mer systems.

defined as

$$
\begin{aligned}
R_{gx}^2 &= \frac{1}{N}\sum_{i=1}^{N} < (\vec{x}_i - \vec{x}_{CM})^2 > \\
R_{gy}^2 &= \frac{1}{N}\sum_{i=1}^{N} < (\vec{y}_i - \vec{y}_{CM})^2 > \\
R_{gz}^2 &= \frac{1}{N}\sum_{i=1}^{N} < (\vec{z}_i - \vec{z}_{CM})^2 >
\end{aligned}
\tag{6.2}
$$

where $\vec{x}_i$, $\vec{y}_i$, and $\vec{z}_i$ is the position vector of the i^{th} atom, $\vec{x}_{CM}$, $\vec{y}_{CM}$, and $\vec{z}_{CM}$ is the position vector of the center of mass. We have also computed these components and plotted in Figure 6.10. We see that for 3-mer and 5-mer melt system, the CG components matches well with the atomistic ones. For 10-mer system, R_g components along x and z directions represents the probable region of the atomistic simulations. However, there is a slight ambiguity for the component along y direction. Thus, it can be understood that the torsions are important to reproduce the correct structural properties (R_g and end-to-end distance).

6.4 Conclusions

In this chapter, we have highlighted the importance of the inclusion of dihedral potential in the structure based coarse-grained simulation of polymers. We have optimized the potential for the CG simulations from the atomistic simulation of Bisphenol-A-polycarbonate. The bonded and non-bonded potentials were optimized using the IBI methodology. A merit function was used to check the convergence of CG potential with the target distributions and RDFs. These CG potentials were used to simulate the polycarbonate melt of 3-mer, 5-mer and 10-mer. When we have simulated these melts without the inclusion of dihedrals, we found that though the RDFs matches with that of the corresponding atomistic trajectories, but the distribution of radius of gyration

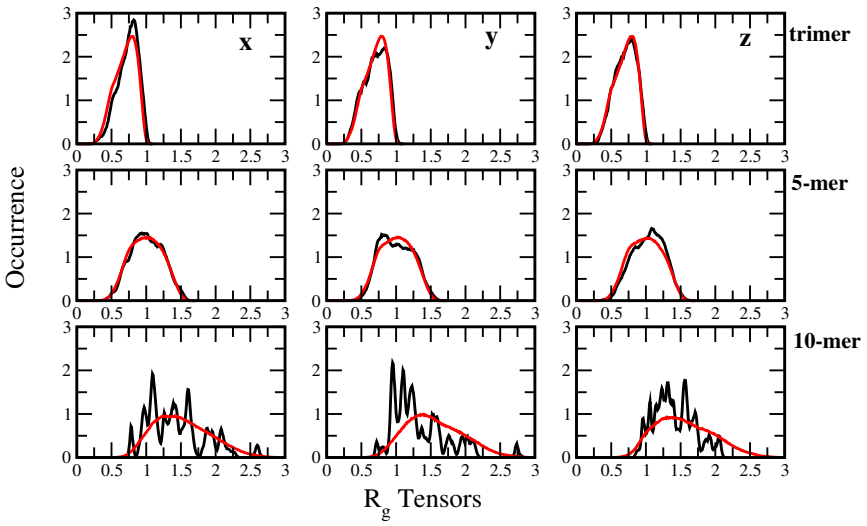

FIGURE 6.10: Distribution of the components of R_g (see Equation (6.2)) when the torsional CBDB potential was incorporated in the CG simulation. Black and red lines corresponds to the atomistic and CG respectively. (a) 3-mer, (b) 5-mer and (c) 10-mer systems.

was significantly off. In these simulation, 1-4 interactions were switched off. Thus, the resemblance of local structural (RDFs), was not able to produce the resemblance in the global structure. Upon incorporating the 1-4 interactions as the non-bonded interactions, we observe the similar behavior. R_g distributions were still off, though for the 3-mer system, there was an improvement in the distribution, but it did not match with the atomistic ones. Now, we imposed 1-4 interaction with the bonded part (the torsional potential). In doing so, we find that there is a significant improvement in the distribution of R_g for 3-mer and 5-mer melt. For 10-mer, the CG R_g distribution captures the maximum probable atomistic distributions. Similar observations are also observed for the distribution of end-to-end distance. Apart from the distribution of overall R_g, its component parallel to x, y and z axis for the CG simulation (with the inclusion of dihedral potential) were computed and they are in agreement with the atomistic simulations.

In this chapter, we found that out of the four dihedrals, three of them were flat in the angle between -60 to +60 and had a very small energy barrier. These dihedrals were thus not considered. Only the dihedral potential CBDB, which showed a distinct behavior was considered in the CG simulations. With the inclusion of this dihedral potential in the CG simulation, we found the distribution of R_g to improve significantly. Thus, this study highlighted the importance of torsional potential for the simulation of polymer melts. Taking this notion further, we have extended the study of these systems in terms of *scalability* in the next chapter. We investigate how the polymeric melt properties behave when the potentials obtained from the smaller systems are used to simulate the higher molecular weights melts.

Chapter 7

Scalability of length scale of coarse-grained potentials for polymers

7.1 Introduction:

In the preceding chapter, we had highlighted the need to include the torsion potential for the coarse-grained (CG) simulation of polymer melts. The potentials were generated using the iterative Boltzmann inversion methodology. In this chapter we extend the study by posing a simple question – are the CG potentials *scalable*?.

In this chapter, we have employed IBI methodology for determining intra and inter bead potentials. In this method, the CG effective potentials between beads are iteratively refined such that the bonded (bonds, angles) and non-bonded (pair correlation) distributions obtained from CG simulations match the respective atomistic distribution. The bonded and non-bonded potentials between CG beads are obtained directly by the Boltzmann inversion of the corresponding distributions from the atomistic simulation. These potentials are used as the initial guess for the CG simulations and further refined iteratively. Although more computational intensive, the structure based CG models have the advantage of keeping some chemical details compared to generic CG models such as simple bead spring or lattice models, where the link to the specific atomistic systems is missing. [207]

In IBI methodology, the effective CG potentials are developed at a specific state point and thus transferability of same CG potentials to a different state points, e.g., temperature, topology, composition and chemical environment are questionable. The transferability of

CG potentials under different thermodynamic conditions for polymers was studied by Carbone et al. [196] and Qian et al. [195] They found that for polystyrene, polyamide melt and liquid ethylbenzene CG potentials were transferable over a various range of temperature and pressure. The CG potentials for the polystyrene was temperature independent only within a certain temperature range while that for the polyamide was transferable over temperature and pressure and glass transition and compressibility modulus were both well reproduced. For liquid ethylbenzene there was instead the need of the modification by a temperature factor of $\sqrt{T/T_0}$ (T_0 is the temperature at which the CG potentials were developed and T is the working temperature). Dalgicdir et al. [85] has studied the transferability of CG model for diphenylalanine peptide in two different chemical environments. They showed that one single CG model can reproduce conformations of diphenylalanine dipeptides in both the bulk and interface (cyclohexane/water) and the partitioning in hydrophobic/hydrophilic medium.

Despite the clear advantages of using structural coarse-grained models in simulating polymer melts or solutions, there is still the drawback of the need to preliminary simulate the system at atomistic level. The atomistic simulations are indeed needed to obtain the pair distributions used in the IBI procedure. The polymer molecular weight to be used in these atomistic simulations is chosen so that the atomistic model behaves as a polymer melt. For example for polystyrene an accepted value is 10 monomers, but a proper systematic study on the effect that this choice has on the performances on the corresponding IBI potentials has not been reported so far. Therefore, in this wok we have derived polycarbonte (PC) CG potentials (bonded and non-bonded) using the IBI method for various chain lengths. We used these potentials to model CG melts of different molecular weights comparing the structural (radius of gyration and end-to-end distance) and dynamical properties (mean square displacement and autocorrelation function) with the atomistic systems and the polymer scaling laws. The *scalability* of the CG IBI potentials were checked by the simulating CG 50-mer and 100-mer PC melt. We have found that the structural properties were in the accepted range of scaling laws. For the first time we have demonstrated the dependence of end-to-end distance relaxation coefficients as the function of molecular weights. We have also predicted that the dynamics of 50-mer and 100-mer CG PC melt is faster by three order of magnitudes than its atomistic counter part.

7.2 Atomistic simulation details

All atomistic molecular dynamics (MD) simulations of PC melt were performed for three different chain lengths: 3-mer, 5-mer and 10-mer. The force field parameters and

simulations details for PC melt system were adapted from Chakraborty et al. [206] All bonds were constrained during the MD using LINCS [119] algorithm. The reaction field [115] method was used for computing the electrostatic interactions beyond the cut-off (1.2 nm) with dielectric constant of 3.5. The systems were simulated at 480 K and 1 Bar. Berendsen thermostat with 0.1 ps coupling time constant and Berendsen barostat with coupling time constant of 1.5 ps were used. [122] The simulations were performed using Gromacs 4.0.7. [130] 80 chains of energy minimized 3-mer were packed in a simulation cell and was simulated for 90 ns. The density obtained from the last 5 ns of 90 ns trajectory was 1061 ± 4.2 kg m^{-3}. 100 chains of 5-mer and 50 chains of 10-mer were also packed and simulated for 100 ns and 80 ns, respectively. Their respective densities (from the last 5 ns of the trajectories) were 1086 ± 2.8 and 1102 ± 2.5 kg m^{-3} (see Section 7.4). As the densities got equilibrated (see Figure 7.1(a) for density and Figure 7.1(b) for potential energy), these trajectories can be used to derive the CG potentials by using the IBI method. These trajectories also serve as a reference (target distributions) for the CG simulations. As the polymer relaxation takes

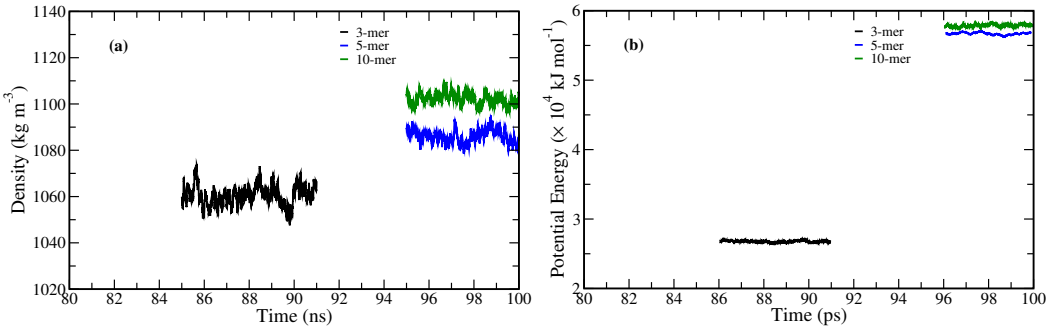

FIGURE 7.1: Density (a) and potential energy (b) as a function of simulation time from the last 5 ns of the atomistic trajectories of 3-mer, 5-mer and 10-mer system.

longer time then the density relaxation, the 5-mer system were simulated for 4.6 μs. Also as the relaxation time increases with the chain length (molecular weight), a slightly different strategy was used to equilibrate the 10-mer system. A simulated annealing (SA) simulation was carried out for 200 ns with the cooling and heating rate of 0.01 K ps^{-1} and 0.006 K ps^{-1}, respectively. The 200^{th} ns snapshot at 480 K, was the input for further 500 ns isothermal-isobaric (NPT) simulation. The 500^{th} ns snapshot served as the initial configuration for the next stage of SA simulation. This cycle of simulations (SA followed by NPT and then SA simulations) was performed for seven times. At the seventh cycle, NPT simulation was carried for 2.3 µs. The 90 ns, 4.6 µs and 2.3 µs trajectories were used for the structural and dynamical analysis for 3-mer, 5-mer and 10-mer systems, respectively.

7.3 Development of CG potentials

7.3.1 Mapping scheme

Generally, one describes the criteria of the mapping of polymers into beads by considering the properties one wants to reflect at the coarser level. We have employed 4:1 mapping scheme for PC, where a monomer is represented by four beads (similar to that in chapter 6). The mapping scheme for the PC (3-mer) is shown in the Figure 7.2. The coordinate for each bead is represented at the center of mass of atoms comprising them. There are five different types of bead viz., A, B, C, D and E, which corresponds to isopropyl, phenylene, carbonate, isopropylidene and phenyl subunits, respectively. This mapping

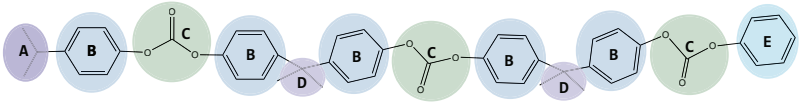

FIGURE 7.2: The mapping scheme of PC (3-mer) is shown. Each CG bead was represented at the center of mass of the comprising atoms. This 4:1 mapping consisted of 5 different beads (A, B, C, D and E).

scheme generated sharp probability distributions for the bonded beads for 3-mer PC melt system (shown in Figure 6.3 for bonded interactions and Figure 6.4 for non-bonded interactions).

7.3.2 Atomistic target distributions

We have converted the atomistic trajectories of 3-mer (last 20 ns), 5-mer (last 30 ns) and 10-mer (last 30 ns) to mapped CG bead trajectories. The bonded distributions and non-bonded radial distribution functions (RDF) were generated from these mapped CG trajectories. The potential of mean force (Equation (2.29)) from these reference distributions were used as the guess potentials ($V_0(r)$) for the CG simulations. These distributions also act as the target distributions ($g^{target}(r)$) for the process of refinement of CG potentials.

7.3.3 CG potentials

The CG potentials for 3-mer, 5-mer and 10-mer PC melt were obtained by the IBI methodology. [69, 78, 90–93] In this method the CG potentials are improved in successive iterations. The effective potentials were updated using Equation (2.31). The IBI methodology was applied to both bonded and non-bonded distributions. The refinement

of each of CG potentials continued till the convergence was less than 0.3% of the target functions (see Equation (2.30), $f_{merit} < 0.003$). [93]

The CG model of PC must produce the same bonded distributions and non-bonded RDFs as that of the reference all atomistic simulations. The distribution of bonded (bonds and angles) and non-bonded RDFs of atomistic and CG trajectories for 3-mer system are plotted in Figures 6.3(a) and 6.3(b). Figure 6.3 shows comparison for the distribution of bonded (bonds and angles) interaction, while the RDF comparisons are shown in Figure 6.4. Similar distributions were obtained for 5-mer and 10-mer potentials (data not shown). Since ABCB, BCBD and DBCE dihedrals distribution resulted flat with very low energy barrier between +60° to -60° (see Figure 6.3(c)), they were not included in the CG potentials and only the CBDB dihedral which had distinct structure was considered. The tabulated interaction potentials were used for the bonds, angles, dihedrals and the non-bonded interactions. The refinement of CG potentials were carried out using the VOTCA toolkit [132] and the simulations were performed with Gromacs-4.6.3 [130].

7.4 CG simulations

Using the three CG potentials developed from 3-mer, 5-mer and 10-mer systems, simulations of higher molecular weight polymers were also performed. The details of all the simulated systems are tabulated in Section 7.4. For the smaller systems (3-mer,

Table 7.1: Details of the atomistic and CG systems. It also lists the density of each systems. These densities were maintained for the CG simulations.

System	No. of Chains	No. of Atoms	No. of CG beads	Density[a]	Molecular Wt.
3-mer	80	8080	960	1045	764.87
5-mer	100	16700	2000	1086	1273.45
10-mer	50	16600	2000	1100	2544.88
50-mer	80	-	16000	1103	12716.32
100-mer	128	-	51200	1103	25430.63

[a] kg m^{-3}

5-mer and 10-mer) we have trajectories from atomistic as well as CG simulations. The atomistic simulations are limited to the short length and time scale, thus 50-mer and 100-mer were only simulated with the CG beads and potentials. The CG potentials developed from the atomistic 3-mer, atomistic 5-mer and atomistic 10-mer systems are referred here as CG 3-mer potentials, CG 5-mer potentials and CG 10-mer potentials, respectively. The CG 3-mer system was simulated with CG 3-mer potentials. The CG 5-mer system was simulated with the CG 3-mer and CG 5-mer potentials, separately. The CG 10-mer system were simulated with CG 3-mer potentials, CG 5-mer potentials

and CG 10-mer potentials. The 50-mer and 100-mer were simulated with CG 3-mer, CG 5-mer and CG 10-mer potentials. The CG 3-mer systems were simulated for 1 µs, while CG 5-mer, 10-mer, 50-mer and 100-mer were simulated for 10 µs. These trajectories were used to analyze the structural and dynamical properties.

7.5 Results and discussions

7.5.1 Structural properties

7.5.1.1 End-to-end distance and radius of gyration:

The distributions of end-to-end distance (R) and radius of gyration (R_g) obtained from both atomistic and CG simulations are reported in Figure 7.3. It appears that for the

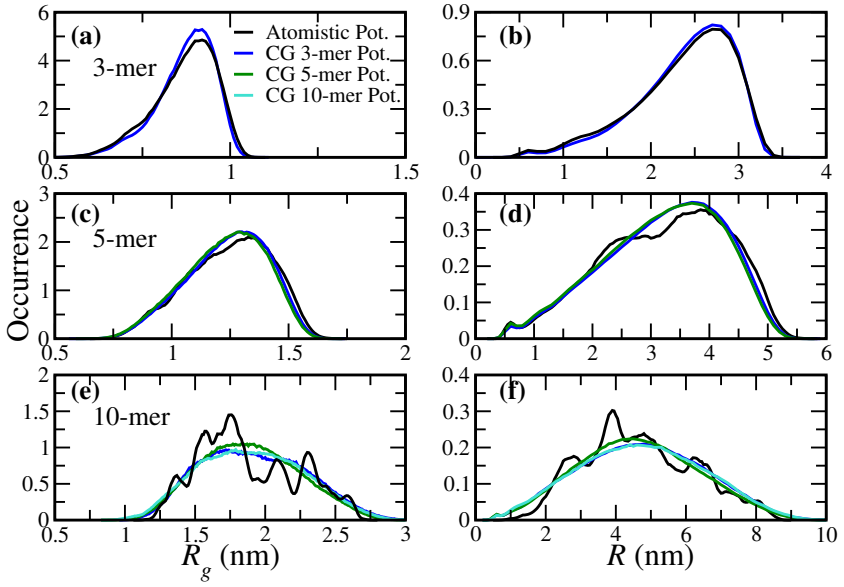

FIGURE 7.3: Distribution of R_g (left panel) and R (right panel) of 3-mer (a, b), 5-mer (c, d) and 10-mer (e, f) systems.

molecular weights corresponding to 3-mer, 5-mer and 10-mer systems the distributions are well matched irrespective of the CG potential used. We, then, used the CG 3-mer potentials, CG 5-mer potentials and CG 10-mer potentials to simulate the PC melt of 50-mer and 100-mer systems (see Section 7.4). As the chain length is very long, it is difficult to equilibrate such systems atomistically, thus we have simulated these systems only with the CG potentials. We have compared the distributions of R and R_g as obtained from CG 3-mer, CG 5-mer and CG 10-mer potentials and plotted them in Figure 7.4. For 50-mer system, the distribution of R and R_g from different CG potentials are similar, but for 100-mer the CG 3-mer potential has wider distribution. It seems

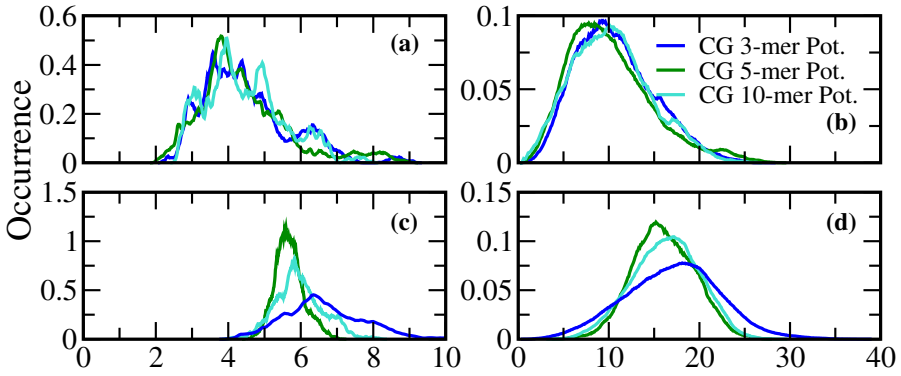

FIGURE 7.4: Distribution of R_g (left panel) and R (right panel) of 50-mer (a, b) and 100-mer (c, d) systems.

that since this potential is obtained from 3-mer system, it is small enough (in length) to account the long ranged interactions. This missing interaction, probably, contributes to the wider distributions. The computation of R_g takes into account the position all the beads. Thus the effect in its distribution is more pronounced than R which considers only the end beads. Figure 7.5 reports the average values of R and R_g as a function of the chain monomer numbers. Fitting these curves with an power law function (see Equation (7.1)), the theoretical scaling coefficients were obtained (see Table 7.2).

$$\begin{aligned} R &\propto N^{\nu} \\ R_g &\propto N^{\lambda} \end{aligned} \tag{7.1}$$

where N is the number of monomers, ν and λ, respectively, are the scaling coefficients for R and R_g. The scaling coefficient for the end-to-end distance for systems simulated

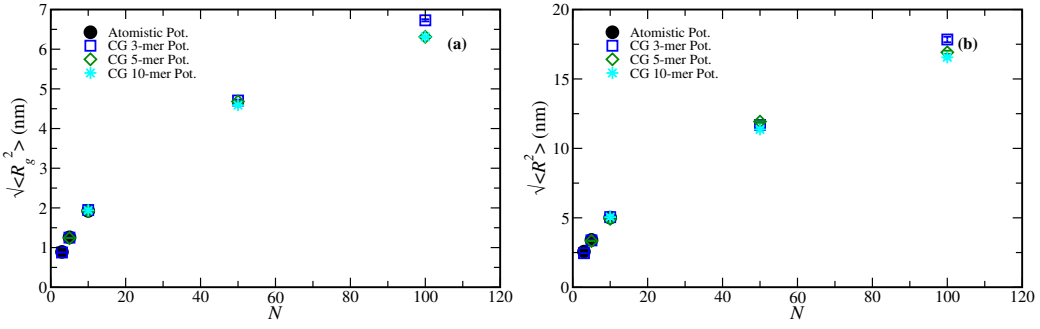

FIGURE 7.5: The root mean square radius of gyration (a) and root mean square end-to-end distance (b) for 3-mer, 5-mer, 10-mer, 50-mer and 100-mer systems.

with different potentials are almost same, while there was a slight variation in the coefficient obtained for R_g (see Table 7.2). The large value obtained from the atomistic simulations can be ascribed to the fact that only chains upto 10 monomers were used in the fitting procedure. Among the experimental values available for PC, the ratio between polymer end-to-end distance and molecular weight (M) lies within 0.864 - 1.384

TABLE 7.2: The scaling coefficients, ν and λ respectively, for R and R_g using Equation (7.1).

Potentials	ν	λ
Atomistic Pot.	0.556 ± 0.004	0.638 ± 0.045
CG 3-mer Pot.	0.556 ± 0.018	0.576 ± 0.175
CG 5-mer Pot.	0.544 ± 0.007	0.546 ± 0.103
CG 10-mer Pot.	0.513 ± 0.005	0.517 ± 0.019

$\mathring{A}^2\ mol\ g^{-1}$. [208, 209] Table 7.3 reports the calculated values for all our simulations. Apart for the 3-mer systems (which consists of just three monomers per chain), all the

TABLE 7.3: $\frac{\langle R^2\rangle}{M}(\mathring{A}^2\ mol\ g^{-1})$ for the studied systems.

System	Atomistic Pot.	CG 3-mer Pot.	CG 5-mer Pot.	CG 10-mer Pot
3-mer	0.861 ± 0.363	0.786 ± 0.308	-	-
5-mer	0.914 ± 0.501	0.895 ± 0.489	0.871 ± 0.483	-
10-mer	0.989 ± 0.644	1.003 ± 0.676	0.955 ± 0.644	1.003 ± 0.683
50-mer	-	1.074 ± 0.792	1.119 ± 1.029	1.009± 0.823
100-mer	-	1.252 ± 0.722	1.112 ± 0.610	1.078 ± 0.483
Expt. [208, 209]	0.864 - 1.384			

tabulated values fall within this range for PC. The mean square end-to-end distance ($\langle R^2\rangle$) and mean square radius of gyration ($\langle R_g^2\rangle$) for the studied systems are tabulated in Tables 7.4 and 7.5. The values for 5-mer and 10-mer are within the limits reported by León et al. [188] The chain dimensions are often expressed in terms of the Flory's characteristic ratio, C_N, which is given as Equation (7.2). We have computed C_N for all the systems. Results for C_N are plotted in Figure 7.6 showing that all the CG potentials reproduce the expected behavior.

TABLE 7.4: Mean Squared End-to-End Distance, $\langle R^2\rangle$, (nm^2)

System	Atomistic Pot.	CG 3-mer Pot.	CG 5-mer Pot.	CG 10-mer Pot.
3-mer	6.558 ± 2.769	6.015 ± 2.354	-	-
5-mer	11.638 ± 6.384	11.403 ± 6.228	11.090 ± 6.153	-
10-mer	25.157 ± 16.386	25.518 ± 17.207	24.307 ± 16.394	25.525 ± 17.383
50-mer	-	136.563 ± 100.702	142.270 ± 130.827	128.276 ± 104.671
100-mer	-	318.318 ± 183.696	286.237 ± 155.146	274.005± 122.865

TABLE 7.5: Mean Squared Radius of Gyration, $\langle R_g^2\rangle$, (nm^2)

System	Atomistic Pot.	CG 3-mer Pot.	CG 5-mer Pot.	CG 10-mer Pot.
3-mer	0.793 ± 0.147	0.768 ± 0.140	-	-
5-mer	1.586 ± 0.439	1.565 ± 0.419	1.535 ± 0. 415	-
10-mer	3.702 ± 1.380	3.787 ± 1.403	3.683 ± 1.344	3.757 ± 1.438
50-mer	-	22.148 ± 10.459	21.921 ± 13.881	21.072 ± 10.905
100-mer	-	45.269 ± 15.217	39.832 ± 10.596	34.909 ± 7.627

$$C_N = \frac{\langle R^2 \rangle}{\sum n_i l_i^2}, \tag{7.2}$$

where n_i is the number of backbone bonds with bond length l_i of type i. From these

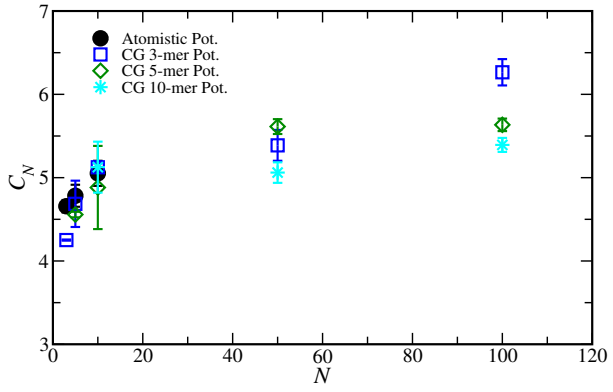

FIGURE 7.6: Plots for the Flory's characteristic ratio, C_N. C_N was computed for 3-mer, 5-mer, 10-mer, 50-mer and 100-mer systems.

results one can conclude that atomistic simulations of short oligomers can be used to develop the CG potential. For PC the shortest chain length turns out to be 5. Thus, in terms of structural properties the IBI potentials are *scaleable*. We, then, investigated the dynamical properties for smaller and higher molecular weights from different CG IBI potentials and compared to the atomistic simulations, wherever available.

7.5.2 Dynamical properties

7.5.2.1 Chain relaxation:

To understand the chain relaxation we calculated time autocorrelation for end-to-end vector and end-to-end distance for all the systems. The autocorrelation, $C(t)$ for any property $f(\tau)$ is given by the following expression:

$$C(t) = \frac{\langle f(\tau_o) f(\tau_o + t) \rangle - \langle f \rangle^2}{\langle f^2 \rangle - \langle f \rangle^2} \tag{7.3}$$

For end-to-end vector correlation, $f = \vec{R}$ while for end-to-end distance correlation $f = \sqrt{\vec{R} \cdot \vec{R}}$. Since the average end-to-end vector $\langle \vec{R} \rangle = 0$ for an isotropic collection of chain, [19] Equation (7.3) reduces to

$$C(t) = \frac{\langle \vec{R}(\tau_o) \cdot \vec{R}(\tau_o + t) \rangle}{\langle \vec{R}^2 \rangle} \tag{7.4}$$

In our simulations, $C(t)$ were computed from the last 50 ns, 4.0 µs and 2.3 µs for the atomistic 3-mer, 5-mer and 10-mer systems, respectively. While for the CG systems, last 500 ns was used for the CG 3-mer system and 1 µs for the CG 5-mer and 10-mer systems and last 5 µs for CG 50-mer and 100-mer systems. For the computation of $C(t)$, every snapshot of the trajectories were considered as time origin (τ_o). Equations (7.3) and (7.4) were used to compute R and $\vec{R}$ autocorrelation, respectively. As expected the dynamics of the atomistic model is slower than the CG ones. For the latter models, the decay of $C(t)$ to zero (decorrelation) is highly dependent upon the degree of coarse-graining and the polymer being investigated.

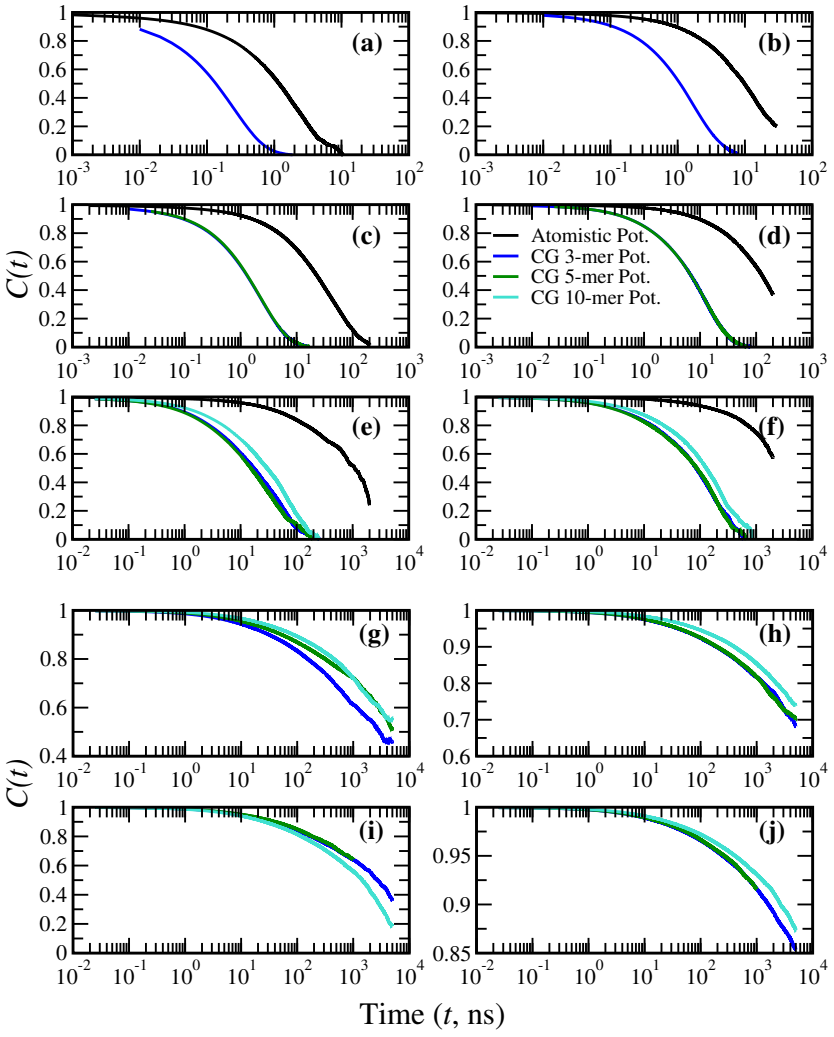

FIGURE 7.7: The autocorrelation function, $C(t)$, of end-to-end distance ($R = \sqrt{\vec{R} \cdot \vec{R}}$, left panel) given by Equation (7.3) and end-to-end vector ($\vec{R}$, right panel) given by Equation (7.4). (a, b), (c, d), (e, f), (g, h) and (i, j) represents 3-mer, 5-mer, 10-mer, 50-mer and 100-mer systems, respectively.

To quantify the different dynamics of the polymers chains, the autocorrelation functions were fitted to a stretched exponential (Kohlrausch-Williams-Watts (KWW)) function

[210] the form:

$$C(t) \;=\; exp\left[-\left(\frac{t}{\tau_{KWW}}\right)^{\beta}\right], \tag{7.5}$$

where τ_{KWW} is the KWW relaxation time, β is the stretch exponent which takes into account the deviation from the ideal Debye behavior. The relaxation times ($\tau_{\vec{R}\ or\ R}$) were calculated as the time integral of the KWW curves with the following expression:

$$\tau_{\vec{R}\ or\ \sqrt{\vec{R}\cdot\vec{R}}} \;=\; \frac{\tau_{KWW}}{\beta}\Gamma\left(\frac{1}{\beta}\right), \tag{7.6}$$

where $\Gamma\,()$ is the gamma function. [87, 211] The relaxation times for R and $\vec{R}$ for all the studied systems are plotted in Figures 7.8(a) and 7.8(b), respectively. It can be noticed that all three CG IBI potentials provide similar relaxation times. The variation of relaxation times with the chain length were fitted by a power law, $\tau_{\vec{R}\ or\ R} \;\propto\; N^{\alpha}$. The fitting was performed for the smaller chain length data points (till 10-mer) and extrapolated to 100-mer. The power law dependence (i.e., values of scaling coefficient α) is tabulated in Table 7.6. We find that the vector relaxation coefficient for 50-mer and 100-mer CG PC melt, follows the extrapolated values, while for the scalar relaxation it is sightly off.

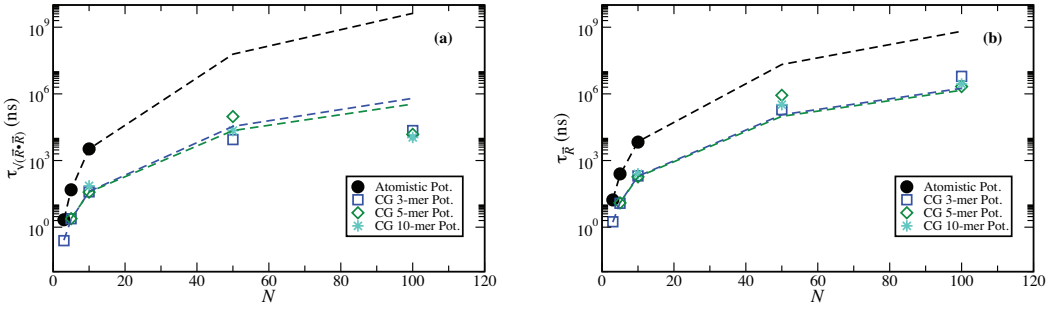

FIGURE 7.8: Relaxation times for the studied systems. It was computed by fitting the plots of the Figure 7.7 to the stretched KWW exponential (Equation (7.5)) and then using Equation (7.6). (a) and (b) respectively, represents the relaxation time for the end-to-end distance and the end-to-end vector. The dotted lines are the power law ($\tau_{\vec{R}\ or\ R} \;\propto\; N^{\alpha}$) fit for the smaller chain lengths.

TABLE 7.6: The power law dependence of the relaxation times. $\tau_{\vec{R}\ or\ R}$ as a function of chain length, N, for atomistic and CG potentials (see Fig. 8 of main paper) were fit to Eq. $\tau_{\vec{R}\ or\ R} \;\propto\; N^{\alpha}$. α for scalar and vector for different potentials are tabulate here.

Potentials	α (R)	α $(\vec{R})$
Atomistic Pot.	6.10	4.99
CG 3-mer Pot.	4.19	3.95
CG 5-mer Pot.	3.96	3.90

7.5.2.2 Translational dynamics:

The translational dynamics of the polymers were studied by computing mean square displacement (MSD) for the center of mass of each chain. The center of mass MSD is defined as $\langle (R_{CM}(t) - R_{CM}(0))^2 \rangle$, where $R_{CM}(0)$ and $R_{CM}(t)$ are the positions of the center of mass of polymer chains at origin and at time t. For the atomistic and CG trajectories, the last 50 ns and 500 ns, respectively, were used for the computation of MSDs. 50 ns atomistic trajectories were split in five equal parts (10 ns each). The MSDs were computed for each of these 10 ns trajectories and then average plot was obtained from these five MSD plots. Similar, strategy was employed for the CG systems, where 500 ns trajectories were split in five equal parts (100 ns each). An average MSD plot was obtained from the five MSD plots. From the linear part of the MSD curves, the self-diffusion coefficient, D, was computed using the Einstein relation: $D = \lim_{t\to\infty} \frac{MSD}{6t}$. Average D was computed from four different sections of the average MSD plots (linear parts) and are tabulated in Table 7.7.

TABLE 7.7: Self Diffusion Coefficient of atomistic ($D^{AA} \times 10^{-5}$ (cm^2 s^{-1})) and CG ($D^{CG} \times 10^{-5}$ (cm^2 s^{-1})) systems of 3-mer, 5-mer, 10-mer, 50-mer and 100-mer.

System	Atomistic Pot.	CG 3-mer Pot.	CG 5-mer Pot.	CG 10-mer Pot.
3-mer	1.987 ± 0.073	17.545 ± 0.674	-	-
5-mer	0.227 ± 0.104	3.682 ± 0.009	3.688 ± 0.003	-
10-mer	0.026 ± 0.001	0.659 ± 0.009	0.641 ± 0.04	0.403 ± 0.023
50-mer	-	0.045 ± 0.007	0.046 ± 0.007	0.032 ± 0.003
100-mer	-	0.015 ± 0.004	0.025 ± 0.002	0.018 ± 0.004

The diffusion coefficient for atomistic (D^{AA}) 3-mer, 5-mer and 10-mer systems are 1.987 ± 0.073, 0.227 ± 0.104 and 0.026 ± 0.001 × 10^{-5} cm^2 s^{-1}, respectively. The diffusion coefficient decreases drastically with the molecular weight (chain length). The reduced degrees of freedom and the softer effective CG potentials leads to the reduced effective friction coefficient between the CG beads compared to the all-atomistic description [75, 76] thus the diffusion coefficient for the CG systems (D^{CG}) are higher than the atomistic ones. We have also computed the diffusion coefficients for 50-mer and 100-mer CG systems. The diffusion coefficients of the 100-mer systems are smaller than the 50-mer systems. Although the CG diffusion coefficients cannot be quantitatively compared with the experimental data it is possible to rescale the dynamics to obtain the correct values. In order to map the time accurately between the atomistic and the coarse-grain length scale, the scaling parameter, S, can be computed as the ratio of the D^{CG} to D^{AA}. In this however, only the asymptotic long time regime is being compared. Assuming that the scaling factor can be applied to the whole time scale of the simulations, an alternative way to map the time is to match the MSD of the center mass of the chain. [75, 76, 84] The

scaling factor, S_{CG-AA}, obtained from matching the MSD curve of CG system on top of all atomistic system (refer Figure 7.9) is tabulated in Table 7.8. The scaled CG MSD and the atomistic MSDs are reported in Figure 7.9. The figure shows perfect matching. S_{CG-AA} for CG 5-mer and 10-mer potentials are similar. Thus, using only one set (CG 3-mer pot.), S_{CG-AA} was extrapolated using power law ($S_{CG-AA} \propto N^k$) for 50-mer and 100-mer CG PC melt systems (see Figure 7.10). The extrapolated values are tabulated in Table 7.8. The values suggest that the CG dynamics for high molecular weight (in our case 50-mer and 100-mer melt) are three orders of magnitude faster than the atomistic simulations. The scaling exponent obtained was close to 2 (see Figure 7.10). The MSD scaling factor scales quadratically to the molecular weight of polymers. These scaling coefficients (S_{CG-AA}) were also used to scale the end-to-end distance and end-to-end vector autocorrelation obtained from the CG simulations of 3-mer, 5-mer and 10-mer systems (see Figure 7.11) showing a remarkable matching also in this case.

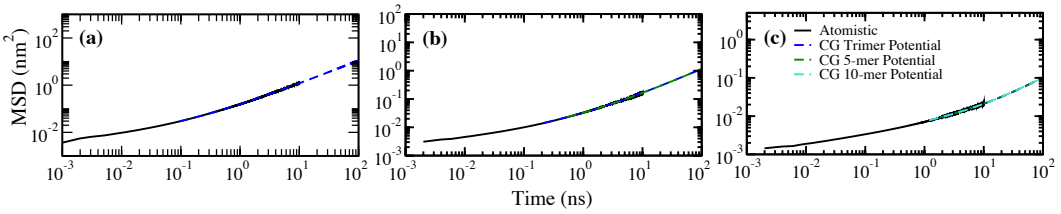

FIGURE 7.9: Scaled MSD of the center of mass of chains for the atomistic and it corresponding scaled CG systems. The CG MSDs were scaled by the factor as tabulated in Table 7.8. (a), (b) and (c) represents 3-mer, 5-mer, 10-mer, 50-mer and 100-mer systems, respectively.

TABLE 7.8: Scaling of CG dynamics. MSD of CG systems was scaled by $S_{CG-AA} = MSD^{AA}/MSD^{CG}$, such that it overlaps with the all atomistic MSDs (see Figure 7.9). The scaling coefficient for 50-mer and 100-mer systems were obtained by fitting the 3-mer, 5-mer and 10-mer data (see Figure 7.10). CG 10-mer Pot. has only one data point, so was not considered for power law scaling.

System	Atomistic Pot.	CG 3-mer Pot.	CG 5-mer Pot.	CG 10-mer Pot.
3-mer	1.0	9.3	-	-
5-mer	1.0	21.8	21.5	-
10-mer	1.0	72.5	72.0	47.5
50-mer	-	1125.4		-
100-mer	-	3674.9		-

7.6 Conclusion

We have systematically investigated the *scalability* of structure based CG IBI potentials derived from short oligomers of polycarbonate. These potentials were derived from the

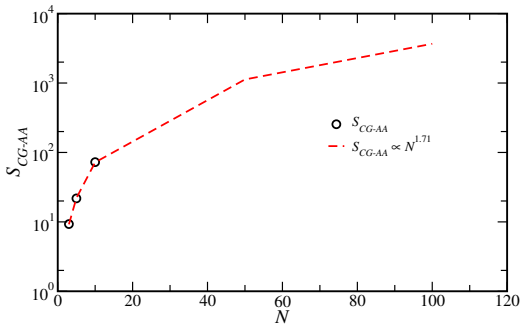

FIGURE 7.10: The MSD scaling factors (S_{CG-AA}) for the studied systems. Power law expression $S_{CG-AA} \propto N^k$ was fitted to 3-mer, 5-mer and 10-mer data points (shown by red dashed lines). S_{CG-AA} for 50-mer and 100-mer systems were anticipated and are tabulated in Table 7.8.

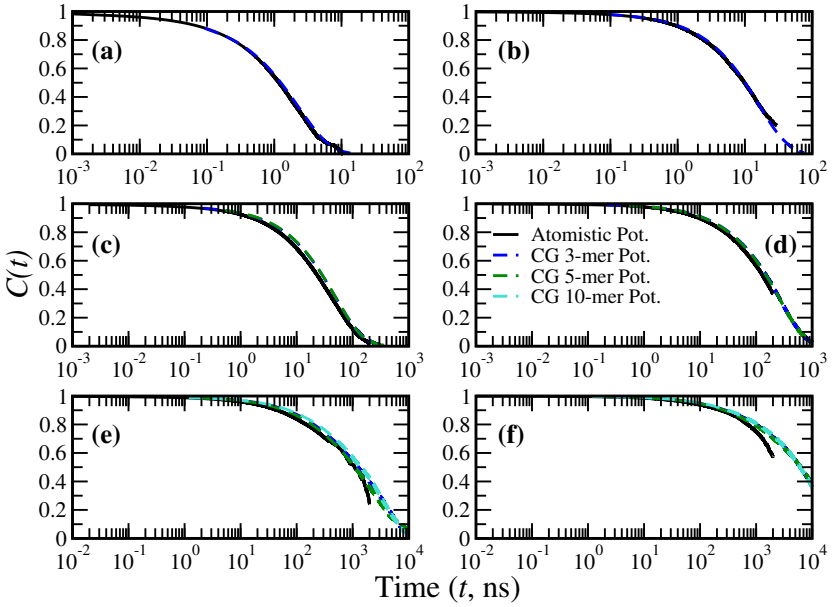

FIGURE 7.11: The scaled autocorrelation function, $C(t)$, of the end-to-end distance (left panel) and end-to-end vector (right panel). The CG plots are scaled according the scaling factor tabulated in Table 7.8. (a, b), (c, d), (e, f), (g, h) and (i, j) represents 3-mer, 5-mer, 10-mer, 50-mer and 100-mer systems, respectively.

atomistic melt systems of 3-mer, 5-mer and 10-mer PC chains. With these potentials, the CG models of PC melt for 3-mer, 5-mer, 10-mer, 50-mer and 100-mer were simulated for longer time. We investigated the structural and dynamical properties of these systems. The ratio of molecular weights of various chain lengths to its radius of gyration were in the range of the reported experimental value. Also the mean square end-to-end distance and mean square radius of gyration of 5-mer and 10-mer PC melt were within the limits reported by León et al. [188] We find that the distributions of end-to-end distances and radii of gyration for all the molecular weights were well matched irrespective of which CG IBI potential was used. The radii of gyration distribution for 100-mer with CG 3-mer potential had wider distribution than CG 5-mer and CG 10-mer potentials. The scaling

coefficient for the end-to-end distance for systems simulated with different potentials were almost same. This suggests that the CG IBI potentials derived from the oligomers (from 5-mer and above) can be used to obtain the structural properties of the higher oligomers or polymers. As the CG IBI potentials were derived by softening the energy landscape and the relaxation of the polymer chains can also be attained. As expected we found that the relaxation time of the polymer chains in melt increases with its chain length. We find that the relaxation of the PC melt by the CG potentials followed the power law dependence. The vector relaxation which shows how the orientational space memory is lost, for 50-mer and 100-mer PC chains followed the anticipated values, while the scalar relaxation were slightly off. The scaling coefficients obtained by overlapping the MSD curve of CG simulations over the atomistic ones also scales the autocorrelation function. This shows that these scaling coefficients may also be used to other dynamical properties. The overlapping of the CG MSD curves over the atomistic MSD curves maps the sub-diffusive region in addition to the asymptotic long time region. We also deduced the quadratic dependence of the MSD scaling factor as a function of polymer chain length. Thus, we find the structural and the dynamical properties of the higher weight oligomers or polymers can be obtained from the CG potentials derived from the low molecular weights.

Chapter 8

Conclusion

In this thesis we have presented the investigations on various soft matter systems using computer simulations. Soft matter in these studies were polymers, lipid bilayers, and surfactant molecules. We discussed the simulation of non-ionic surfactants and lipid bilayers in presence of polymer – polyethylenimine. The emphases were on the structural and dynamical properties of polymer and perturbation on the soft matter because of the incorporation of polymer in the surfactant matrix and lipid membranes. The polymer solvation, polymer–surfactant, and polymer-lipid membranes systems were studied using the atomistic molecular dynamics simulations. We have also studied the polymer melt where polymer is surrounded with itself. In this case, we employed coarse-grained simulation technique to understand the structural and dynamical behavior of polymers. Coarse-grained simulation enables us to scale the length and time scales limited by the atomistic simulations. Here we have shown that the CG potentials derived from the lower length scale atomistic simulations can be transferred to the longer CG polymer chain.

Polyethylenimine being a potent non-viral gene delivery vector, it transverses carrying the cargo from the exterior of the human body to the target cells inside the human body. In this course of action, the obvious change in the chemical environment for PEI-drug complex is the pH. When the complex is internalized into the cell, it moves from the neutral environment of the extracellular space, to the acidic pH of the endosome. As the complex encounters a cell, the endocytosis process kicks in. It engulfs the complexes in a little cell membrane which is pinched off inside the cell. The solution inside these endosomes are acidic. PEI being cationic in nature expands its polymeric network, resulting enclosed drug to fall apart from the network. This is turn generates sufficient osmotic pressure to burst open the endosomes, releasing the content into the cell interior, where it is free to make its way to the nucleus. In the later process, PEI again encounters

a change in pH from acidic in endosomes to neural in the cytoplasm. Thus, the chemical environment – pH forms an pivotal aspect of this thesis.

PEI is represented in two protonation states viz., unprotonated and protonated which corresponds to basic and acidic environment, respectively. In protonated case all the amine moieties are protonated while unprotonated do not have such protonation. As PEI comes across acidic and basic pH, the solvation of PEI which plays a crucial role in governing the polymer conformations, is explored in chapter 3. The structural and dynamical properties of PEI in different protonation states in presence of explicit water are investigated in this chapter. We learned that PEI chain elongates on increasing the protonation level, which is inferred from the increase in radius of gyration and end-to-end distances. On increasing the protonation level, i.e., moving from un to alternate to all protonated system, there is a steady increase in the electrostatic interactions. This causes repulsion among the monomeric units and to minimize the interactions, PEI chain elongates. The all protonated PEI has a dominant *trans* conformations in the dihedrals. This elongation can be related to the expansion of polymeric network in the acidic endosomes, which results in the release of cargo. We also found that the all protonated PEI has a ordered solvation shells. The solvation shells possess slow and fast relaxing water molecules. The water molecules of first solvation shell of the protonated system (as compared to unprotonated system) experience higher attractive attractions towards the chain with strong H-bonding network, which retard its dynamics. The water molecules of the first solvation shell of unprotonated system diffuse slowly than that of the all protonated system. The motion of these water molecules for all protonated PEI system is along the chain. In case of unprotonated chain the water molecules move along the chain and also jump to spatially neighboring solvation (not the nearest neighbors) shells of nearby N-atom.

In chapter 4, we focussed on the structure and dynamics of PEI in un and all protonated states in presence of non-ionic surfactants in aqueous solution. Experimentally, NMR and optical microscopy showed that the hexagonal mesophase formed by the surfactant molecules gets disrupted with the introduction of PEI in high pH. [100] The simulation investigations also highlights the similar behavior where we find that the hydrophobic and dipolar interactions causes the unprotonated PEI to aggregate with surfactant molecules. This aggregation disturbs the hexagonal mesophase. While the protonated PEI is being surrounded by ordered solvation shell, interact less with the surfactants and cannot cause such disruptions.

PEI while delivering its genetic content, interacts with cell membranes which are basically composed of phospholipids. The perturbation effect on the lipid bilayers in presence of PEI at high and low pH are researched in chapter 5. We embedded PEI in hydrophilic

and hydrophobic regions. PEIs mostly settled at the interface (formed by lipid head groups and water). While a small hydrophilic pore was formed in the bilayer when the protonated PEI was positioned spanning from the aqueous layer on the one side to the aqueous layer on the other side through the bilayer. The multiple cationic centers in the PEI chains facilitates the formation of such pore which allows to ballistically diffuse the water molecules though it. This disruptions is in consistent with the experimental studies by Helander et al. on Gram-negative bacteria. [40] Disruptions of the bilayer also resulted in the orientation change in the phospholipids molecules. This new insight is valuable in having a clear idea on the effect of concentration of PEI and eventually to design a better vector.

In the last part of the thesis (chapters 6 and 7) we used the coarse-grain (CG) methodologies to simulate Bisphenol-A-polycarbonate melt. With a CG model typically several atoms were grouped into one particle, while the interaction properties of the new particle were developed by the iterative Boltzmann inversion (IBI) methodology. By grouping atoms together, coarse graining reduces the degrees of freedom and, therefore, the computational cost. In chapter 6, we highlighted the importance on the inclusion of torsional potential, developed by IBI method, in the CG simulations. The atomistic polymer melt structure is mapped onto the coarse configuration by grouping few atoms as a bead. We find that the structural properties viz., polymer end-to-end distance and radius of gyration from the coarse-grain did not match the atomistic simulations. On inclusion of the dihedral potential, which had a distinct structure, these structural properties matches very well. Taking this notion further, we investigated the *scalability* of CG potentials generated using the IBI technique from the oligomers to the higher molecular weight polymers in chapter 7. We have systematically studied by generating the IBI potentials from 3-mer, 5-mer, and 10-mer melt systems and then used these potentials to simulate 50-mer and 100-mer polycarbonate melts. The distributions of end-to-end distance and radius of gyration for smaller chain lengths well matched irrespective of which CG IBI potential was used. Also, the polymer law of scaling for the end-to-end distance for systems simulated with different potentials were almost same. This suggests that the CG IBI potentials derived from the oligomers (from 5-mer and above) can be used to obtain the structural properties of the higher oligomers or polymers. The potential energy surface of the CG models are softened because of the reduced degrees of freedom. This can also help to relax the polymer chains faster. The relaxation time of the polymer chains in melts increases with the molecular weights. The vector relaxation which shows how the orientational space memory is lost, for 50-mer and 100-mer PC chains followed the anticipated values, while the scalar relaxation were slightly off. The scaling coefficients obtained by overlapping the MSD curve of CG simulations over the atomistic ones also scales the autocorrelation function. This shows that these scaling

coefficients may also be used to other dynamical properties. The overlapping of the CG MSD curves over the atomistic MSD curves maps the sub-diffusive region in addition to the asymptotic long time region. We also deduced the quadratic dependence of the MSD scaling factor as a function of polymer chain length. Thus, we find the structural and the dynamical properties of the higher weight oligomers or polymers can be obtained from the CG potentials derived from the low molecular weights.

Overall, this thesis presented an account of the computer simulation studies using the multiscale simulation approach on soft matter systems. The CG molecular dynamics simulation strategies were employed to explore the structural and dynamical properties of polymer systems in melt state. The information to the coarser level was transferred from the atomistic simulations. This multiscale coupling was through the bead-bead potential (CG potential). The CG potentials developed from the 5-mer polycarbonate melt systems were able to produce the properties of the higher molecular weights. On the atomistic scale, at high pH PEI disrupts the hexagonal mesophase formed by the non-ionic surfactant molecules. This observation was in relevance with the experiments. At low pH, PEI has the tendency to rupture the lipid bilayer systems. These observations on soft matter systems had provided an in-depth understanding of their structure and functions.

Bibliography

[1] Richard A. L. Jones. *Introduction and overview*, pages 1–2. Oxford University Press, 2002. ISBN 978-0198505891.

[2] J. N. Israelachvili. *Thermodynamic and Statistical Aspects of Intermolecular Forces*, chapter 2, pages 23–51. Elsevier Science, 2011. ISBN 978-0-12-375182-9.

[3] L. S. Hirst. *Fundamentals of Soft Matter Science*. Taylor & Francis, 2012. ISBN 9781439827758. URL `https://books.google.co.in/books?id=RqmmGjjmzZsC`.

[4] Gompper G. and Schick M. *Soft Matter: Volume 1 - Polymer Melts and Mixtures*, chapter An Introduction to Soft Matter, pages 1–16. Wiley, 2006.

[5] Thomas A. Witten. Insights from soft condensed matter. *Reviews of Modern Physics*, 71(2):S367–S373, 03 1999. URL `http://link.aps.org/doi/10.1103/RevModPhys.71.S367`.

[6] Ian W. Hamley. *Introduction*, pages 1–37. John Wiley & Sons, Ltd, 2007. ISBN 9780470517338. doi: 10.1002/9780470517338.ch1. URL `http://dx.doi.org/10.1002/9780470517338.ch1`.

[7] Jacob Israelachvili and Richard Pashley. The hydrophobic interaction is long range, decaying exponentially with distance. *Nature*, 300(5890):341–342, 11 1982. URL `http://dx.doi.org/10.1038/300341a0`.

[8] Richard A. L. Jones. *Supramolecular self-assembly in soft condensed matter*, pages 136–158. Oxford University Press, 2002. ISBN 978-0198505891.

[9] Ian W. Hamley. *Polymers*, pages 39–110. John Wiley & Sons, Ltd, 2007. ISBN 9780470517338. doi: 10.1002/9780470517338.ch2. URL `http://dx.doi.org/10.1002/9780470517338.ch2`.

[10] T. A. Witten and P. A. Pincus. *Structured Fluids: Polymers, Colloids, Surfactants*. Oxford University Press, 2004. ISBN 9780198526889.

[11] Ian W. Hamley. *Colloids*, pages 111–159. John Wiley & Sons, Ltd, 2007. ISBN 9780470517338. doi: 10.1002/9780470517338.ch3. URL http://dx.doi.org/10.1002/9780470517338.ch3.

[12] Y.S. Lee. *Self-Assembly and Nanotechnology: A Force Balance Approach*. Wiley, 2008. ISBN 9780470292518. URL https://books.google.co.in/books?id=hGRtW2jzkzEC.

[13] Henry S. Frank and Marjorie W. Evans. Free volume and entropy in condensed systems iii. entropy in binary liquid mixtures; partial molal entropy in dilute solutions; structure and thermodynamics in aqueous electrolytes. *The Journal of Chemical Physics*, 13(11):507–532, 1945. doi: http://dx.doi.org/10.1063/1.1723985. URL http://scitation.aip.org/content/aip/journal/jcp/13/11/10.1063/1.1723985.

[14] Kozo Shinoda. "iceberg" formation and solubility. *The Journal of Physical Chemistry*, 81(13):1300–1302, 06 1977. doi: 10.1021/j100528a016. URL http://dx.doi.org/10.1021/j100528a016.

[15] L. Magnus Bergström. *Thermodynamics of Self-Assembly*, chapter 11, pages 289–314. InTech, 2011. ISBN 978-953-307-980-6. doi: 10.5772/13711. URL http://dx.doi.org/10.5772/13711.

[16] Noel T. Southall, Ken A. Dill, and A. D. J. Haymet. A view of the hydrophobic effect. *The Journal of Physical Chemistry B*, 106(3):521–533, 01 2002. doi: 10.1021/jp015514e. URL http://dx.doi.org/10.1021/jp015514e.

[17] T. Yamaguchi, T. Matsuoka, and S. Koda. Mode-coupling study on the dynamics of hydrophobic hydration ii: Aqueous solutions of benzene and rare gases. *Physical Chemistry Chemical Physics*, 8(6):737–745, 2006. doi: 10.1039/B514196F. URL http://dx.doi.org/10.1039/B514196F.

[18] Ian W. Hamley. *Biological Soft Matter*, pages 275–311. John Wiley & Sons, Ltd, 2007. ISBN 9780470517338. doi: 10.1002/9780470517338.ch6. URL http://dx.doi.org/10.1002/9780470517338.ch6.

[19] Ralph H. Colby Michael Rubinstein. *Polymer Physics*. OUP Oxford, 2003. ISBN 978-0198520597.

[20] Sante Di Gioia and Massimo Conese. Polyethylenimine-mediated gene delivery to the lung and therapeutic applications. *Drug design, development and therapy*, 2:163–188, 2008. URL http://www.ncbi.nlm.nih.gov/pmc/articles/PMC2761186/.

[21] Chong-Su Cho. Design and development of degradable polyethylenimines for delivery of dna and small interfering rna: An updated review. *ISRN Materials Science*, 2012:24, 2012. URL http://dx.doi.org/10.5402/2012/798247%]798247.

[22] J W Wiseman, C A Goddard, D McLelland, and W H Colledge. A comparison of linear and branched polyethylenimine (pei) with dcchol//dope liposomes for gene delivery to epithelial cells in vitro and in vivo. *Gene Therapy*, 10(19):1654–1662, print 0000. URL http://dx.doi.org/10.1038/sj.gt.3302050.

[23] Takeo Saegusa, Hiroharu Ikeda, and Hiroyasu Fujii. Crystalline polyethylenimine. *Macromolecules*, 5(1):108, 1972. doi: 10.1021/ma60025a029. URL http://pubs.acs.org/doi/abs/10.1021/ma60025a029.

[24] O Boussif, F Lezoualc'h, M A Zanta, M D Mergny, D Scherman, B Demeneix, and J P Behr. A versatile vector for gene and oligonucleotide transfer into cells in culture and in vivo: polyethylenimine. *Proceedings of the National Academy of Sciences of the United States of America*, 92(16):7297, 1995. URL http://www.pnas.org/content/92/16/7297.abstract.

[25] D Goula, C Benoist, S Mantero, G Merlo, G Levi, and B A Demeneix. Polyethylenimine-based intravenous delivery of transgenes to mouse lung. *Gene Ther.*, 5:1291, 1998. URL http://www.nature.com/gt/journal/v5/n9/abs/3300717a.html.

[26] W.T. Godbey, Michael A. Barry, Peter Saggau, Kenneth K. Wu, and Antonios G. Mikos. Poly(ethylenimine)-mediated transfection: A new paradigm for gene delivery. *J. Biomed. Mater. Res.*, 51(3):321, 2000. ISSN 1097-4636. doi: 10.1002/1097-4636(20000905)51:3¡321::AID-JBM5¿3.0.CO;2-R. URL http://dx.doi.org/10.1002/1097-4636(20000905)51:3<321::AID-JBM5>3.0.CO;2-R.

[27] Lionel Wightman, Ralf Kircheis, Vanessa Rössler, Sebastian Carotta, Regina Ruzicka, Malgorzata Kursa, and Ernst Wagner. Different behavior of branched and linear polyethylenimine for gene delivery in vitro and in vivo. *J. Gene Med.*, 3 (4):362, 2001. ISSN 1521-2254. doi: 10.1002/jgm.187. URL http://dx.doi.org/10.1002/jgm.187.

[28] Mini Thomas and Alexander M. Klibanov. Enhancing polyethylenimine's delivery of plasmid dna into mammalian cells. *Proceedings of the National Academy of Sciences of the United States of America*, 99(23):14640, 2002. doi: 10.1073/pnas.192581499. URL http://www.pnas.org/content/99/23/14640.abstract.

[29] S Li and L Huang. Nonviral gene therapy: promises and challenges. *Gene Ther.*, 7:31, 2000.

[30] Akin Akinc, Mini Thomas, Alexander M. Klibanov, and Robert Langer. Exploring polyethylenimine-mediated dna transfection and the proton sponge hypothesis. *J. Gene Med.*, 7(5):657, 2005. ISSN 1521-2254. doi: 10.1002/jgm.696. URL http://dx.doi.org/10.1002/jgm.696.

[31] David Brown, Julian H. R. Clarke, Motoi Okuda, and Takao Yamazaki. The preparation of polymer melt samples for computer simulation studies. *The Journal of Chemical Physics*, 100(8):6011–6018, 1994. URL http://scitation.aip.org/content/aip/journal/jcp/100/8/10.1063/1.467111.

[32] Hossein Eslami, Florian MÜller-Plathe, and Sylvio Canuto. *Solvation In Polymers*, volume 6, pages 279–320. Springer Netherlands, 2008. ISBN 978-1-4020-8270-2. doi: 10.1007/978-1-4020-8270-2–“˙”11. URL http://dx.doi.org/10.1007/978-1-4020-8270-2_11.

[33] Qing Ji and Xiaozhen Yang. Detailed structures and mechanism of polymer solvation. *J. Phys. Chem. B*, 110(45):22719, 2012/09/12 2006. doi: 10.1021/jp0643101. URL http://dx.doi.org/10.1021/jp0643101.

[34] Árpád Szenczi, József Kardos, György A. Medgyesi, and Péter Závodszky. The effect of solvent environment on the conformation and stability of human polyclonal igg in solution. *Biologicals*, 34(1):5, 3 2006. URL http://www.sciencedirect.com/science/article/pii/S1045105605000606.

[35] Samir Kumar Pal and Ahmed H. Zewail. Dynamics of water in biological recognition. *Chemical Reviews*, 104(4):2099, 2012/09/15 2004. doi: 10.1021/cr020689l. URL http://dx.doi.org/10.1021/cr020689l.

[36] Y K Cheng and Peter J. Rossky. Surface topography dependence of biomolecular hydrophobic hydration. *Nature*, 392(6677):696, 04 1998. URL http://dx.doi.org/10.1038/33653.

[37] Xavier Daura, Alan E. Mark, and Wilfred F. van Gunsteren. Peptide folding simulations: no solvent required? *Comput. Phys. Commun.*, 123(1–3):97, 12 1999. URL http://www.sciencedirect.com/science/article/pii/S0010465599002611.

[38] Del Lucent, V. Vishal, and Vijay S. Pande. Protein folding under confinement: A role for solvent. *Proceedings of the National Academy of Sciences of the United States of America*, 104(25):10430, 06 2007. URL http://www.pnas.org/content/104/25/10430.abstract.

[39] J. C. T. Kwak. *Polymer-Surfactant Systems*. Taylor & Francis, 1998. ISBN 9780824702328. URL https://books.google.co.in/books?id=l5XjVjmViw4C.

[40] IIkka M. Helander, Hanna-Leena Alakomi, Kyösti Latva-Kala, and Pertti Koski. Polyethyleneimine is an effective permeabilizer of gram-negative bacteria. *Microbiology*, 143(10):3193–3199, 1997. doi: 10.1099/00221287-143-10-3193. URL http://mic.sgmjournals.org/content/143/10/3193.abstract.

[41] Almut Mecke, István J. Majoros, Anil K. Patri, James R. Baker, Mark M. Banaszak Holl, and Bradford G. Orr. Lipid bilayer disruption by polycationic polymers: The roles of size and chemical functional group. *Langmuir*, 21(23):10348–10354, 2012/08/29 2005. doi: 10.1021/la050629l. URL http://dx.doi.org/10.1021/la050629l.

[42] Anna Åkesson, Tania K. Lind, Robert Barker, Arwel Hughes, and Marité Cárdenas. Unraveling dendrimer translocation across cell membrane mimics. *Langmuir*, 28 (36):13025–13033, 2012. doi: 10.1021/la3027144. URL http://pubs.acs.org/doi/abs/10.1021/la3027144.

[43] Mariusz Kepczynski, Dorota Jamróz, Magdalena Wytrwal, Jan Bednar, Ewa Rzad, and Maria Nowakowska. Interactions of a hydrophobically modified polycation with zwitterionic lipid membranes. *Langmuir*, 28(1):676–688, 2012/08/29 2011. doi: 10.1021/la203748q. URL http://dx.doi.org/10.1021/la203748q.

[44] Martin Sikor, Juan Sabin, Amir Keyvanloo, Matthias F. Schneider, Jenifer L. Thewalt, Arthur E. Bailey, and Barbara J. Frisken. Interaction of a charged polymer with zwitterionic lipid vesicles. *Langmuir*, 26(6):4095–4102, 2012/08/29 2010. doi: 10.1021/la902831n. URL http://dx.doi.org/10.1021/la902831n.

[45] Seungpyo Hong, Pascale R. Leroueil, Elizabeth K. Janus, Jennifer L. Peters, Mary-Margaret Kober, Mohammad T. Islam, Bradford G. Orr, James R. Baker, and Mark M. Banaszak Holl. Interaction of polycationic polymers with supported lipid bilayers and cells: nanoscale hole formation and enhanced membrane permeability. *Bioconjugate Chemistry*, 17(3):728–734, 2006. doi: 10.1021/bc060077y. URL http://pubs.acs.org/doi/abs/10.1021/bc060077y. PMID: 16704211.

[46] Wolfgang H. Binder, Veronique Barragan, and Fredric M. Menger. Domains and rafts in lipid membranes. *Angewandte Chemie International Edition*, 42(47): 5802–5827, 2003. ISSN 1521-3773. doi: 10.1002/anie.200300586. URL http://dx.doi.org/10.1002/anie.200300586.

[47] Roland R. Netz and M. Schick. Pore formation and rupture in fluid bilayers. *Physical Review E*, 53:3875–3885, Apr 1996. doi: 10.1103/PhysRevE.53.3875. URL http://link.aps.org/doi/10.1103/PhysRevE.53.3875.

[48] Hari Leontiadou, Alan E. Mark, and Siewert J. Marrink. Molecular dynamics simulations of hydrophilic pores in lipid bilayers. *Biophysical Journal*, 86(4): 2156–2164, 04 2004. URL http://linkinghub.elsevier.com/retrieve/pii/S0006349504742757.

[49] Ralf W. Glaser, Sergei L. Leikin, Leonid V. Chernomordik, Vasili F. Pastushenko, and Artjom I. Sokirko. Reversible electrical breakdown of lipid bilayers: formation and evolution of pores. *Biochim. Biophys. Acta, Biomembr.*, 940(2): 275–287, 5 1988. URL http://www.sciencedirect.com/science/article/pii/0005273688902027.

[50] D. Peter Tieleman, Hari Leontiadou, Alan E. Mark, and Siewert-Jan Marrink. Simulation of pore formation in lipid bilayers by mechanical stress and electric fields. *Journal of the American Chemical Society*, 125(21):6382–6383, 2003. doi: 10.1021/ja029504i. URL http://pubs.acs.org/doi/abs/10.1021/ja029504i.

[51] Frantz Jean-François, Juan Elezgaray, Pascal Berson, Pierre Vacher, and Erick J. Dufourc. Pore formation induced by an antimicrobial peptide: Electrostatic effects. *Biophysical Journal*, 95(12):5748–5756, 12 2008. URL http://www.sciencedirect.com/science/article/pii/S0006349508819911.

[52] Ying Wang, Yanli Tang, Zhijun Zhou, Eunkyung Ji, Gabriel P. Lopez, Eva Y. Chi, Kirk S. Schanze, and David G. Whitten. Membrane perturbation activity of cationic phenylene ethynylene oligomers and polymers: Selectivity against model bacterial and mammalian membranes. *Langmuir*, 26(15):12509–12514, 2012/11/04 2010. doi: 10.1021/la102269y. URL http://dx.doi.org/10.1021/la102269y.

[53] K. Matsuzaki, S. Yoneyama, and K. Miyajima. Pore formation and translocation of melittin. *Biophysical Journal*, 73(2):831–838, 08 1997. URL http://linkinghub.elsevier.com/retrieve/pii/S0006349597781153.

[54] Yechiel Shai. Mechanism of the binding, insertion and destabilization of phospholipid bilayer membranes by -helical antimicrobial and cell non-selective membrane-lytic peptides. *Biochim. Biophys. Acta, Biomembr.*, 1462(1–2):55 – 70, 1999. ISSN 0005-2736. doi: 10.1016/S0005-2736(99)00200-X. URL http://www.sciencedirect.com/science/article/pii/S000527369900200X.

[55] Eric H. Hill, Kelly Stratton, David G. Whitten, and Deborah G. Evans. Molecular dynamics simulation study of the interaction of cationic biocides with lipid bilayers: Aggregation effects and bilayer damage. *Langmuir*, 28(42):14849–14854, 2012. doi: 10.1021/la303158c. URL http://pubs.acs.org/doi/abs/10.1021/la303158c.

[56] Yechiel Shai. Mode of action of membrane active antimicrobial peptides. *Pept. Sci.*, 66(4):236–248, 2002. URL http://dx.doi.org/10.1002/bip.10260.

[57] S. Paula, A. G. Volkov, A. N. Van Hoek, T. H. Haines, and D. W. Deamer. Permeation of protons, potassium ions, and small polar molecules through phospholipid bilayers as a function of membrane thickness. *Biophysical Journal*, 70 (1):339–348, 01 1996. URL http://linkinghub.elsevier.com/retrieve/pii/S0006349596795759.

[58] Hari Leontiadou, Alan E. Mark, and Siewert-Jan Marrink. Ion transport across transmembrane pores. *Biophysical Journal*, 92(12):4209–4215, 06 2007. URL http://linkinghub.elsevier.com/retrieve/pii/S0006349507712237.

[59] Kyle C. Smith, John C. Neu, and Wanda Krassowska. Model of creation and evolution of stable electropores for dna delivery. *Biophysical Journal*, 86(5): 2813–2826, 05 2004. URL http://linkinghub.elsevier.com/retrieve/pii/S0006349504743349.

[60] Raffaello Potestio, Christine Peter, and Kurt Kremer. Computer simulations of soft matter: Linking the scales. *Entropy*, 16(8):4199–4245, 2014. ISSN 1099-4300. doi: 10.3390/e16084199. URL http://www.mdpi.com/1099-4300/16/8/4199.

[61] Rolf Auhl, Ralf Everaers, Gary S. Grest, Kurt Kremer, and Steven J. Plimpton. Equilibration of long chain polymer melts in computer simulations. *The Journal of Chemical Physics*, 119(24):12718–12728, 2003. URL http://scitation.aip.org/content/aip/journal/jcp/119/24/10.1063/1.1628670.

[62] Guojie Zhang, Livia A. Moreira, Torsten Stuehn, Kostas Ch. Daoulas, and Kurt Kremer. Equilibration of high molecular weight polymer melts: A hierarchical strategy. *ACS Macro Letters*, 3(2):198–203, 2014/12/22 2014. doi: 10.1021/mz5000015. URL http://dx.doi.org/10.1021/mz5000015.

[63] Hossein Ali Karimi-Varzaneh, Nico F. A. van der Vegt, Florian Müller-Plathe, and Paola Carbone. How good are coarse-grained polymer models? a comparison for atactic polystyrene. *ChemPhysChem*, 13(15):3428–3439, 2012. ISSN 1439-7641. doi: 10.1002/cphc.201200111. URL http://dx.doi.org/10.1002/cphc.201200111.

[64] Paola Carbone and Carlos Avendaño. Coarse-grained methods for polymeric materials: enthalpy- and entropy-driven models. *Wiley Interdisciplinary Reviews: Computational Molecular Science*, 4(1):62–70, 2014. ISSN 1759-0884. doi: 10.1002/wcms.1149. URL http://dx.doi.org/10.1002/wcms.1149.

[65] Mohammad Rahimi, Hossein Ali Karimi-Varzaneh, Michael C. Böhm, Florian Müller-Plathe, Sebastian Pfaller, Gunnar Possart, and Paul Steinmann. Nonperiodic

stochastic boundary conditions for molecular dynamics simulations of materials embedded into a continuum mechanics domain. *The Journal of Chemical Physics*, 134(15):154108, 2011. doi: http://dx.doi.org/10.1063/1.3576122. URL http://scitation.aip.org/content/aip/journal/jcp/134/15/10.1063/1.3576122.

[66] Florian Müller-Plathe. Coarse-graining in polymer simulation: From the atomistic to the mesoscopic scale and back. *ChemPhysChem*, 3(9):754–769, 2002. doi: 10.1002/1439-7641(20020916)3:9¡754::AID-CPHC754¿3.0.CO;2-U. URL http://dx.doi.org/10.1002/1439-7641(20020916)3:9<754::AID-CPHC754>3.0.CO;2-U.

[67] W. Tschöp, K. Kremer, O. Hahn, J. Batoulis, and T. Bürger. Simulation of polymer melts. ii. from coarse-grained models back to atomistic description. *Acta Polymerica*, 49(2-3):75–79, 1998. doi: 10.1002/(SICI)1521-4044(199802)49:2/3¡75::AID-APOL75¿3.0.CO;2-5. URL http://dx.doi.org/10.1002/(SICI)1521-4044(199802)49:2/3<75::AID-APOL75>3.0.CO;2-5.

[68] Dirk Reith, Hendrik Meyer, and Florian Müller-Plathe. Mapping atomistic to coarse-grained polymer models using automatic simplex optimization to fit structural properties. *Macromolecules*, 34(7):2335–2345, 2014/03/03 2001. doi: 10.1021/ma001499k. URL http://dx.doi.org/10.1021/ma001499k.

[69] Dirk Reith, Mathias Pütz, and Florian Müller-Plathe. Deriving effective mesoscale potentials from atomistic simulations. *Journal of Computational Chemistry*, 24(13): 1624–1636, 2003. doi: 10.1002/jcc.10307. URL http://dx.doi.org/10.1002/jcc.10307.

[70] Teemu Murtola, Mikko Karttunen, and Ilpo Vattulainen. Systematic coarse graining from structure using internal states: application to phospholipid/cholesterol bilayer. *The Journal of Chemical Physics*, 131(5):055101, Aug 2009. doi: 10.1063/1.3167405.

[71] Emiliano Brini, Elena A. Algaer, Pritam Ganguly, Chunli Li, Francisco Rodriguez-Ropero, and Nico F. A. van der Vegt. Systematic coarse-graining methods for soft matter simulations - a review. *Soft Matter*, 9:2108–2119, 2013. doi: 10.1039/C2SM27201F. URL http://dx.doi.org/10.1039/C2SM27201F.

[72] Berk Hess, Salvador Leon, Nico van der Vegt, and Kurt Kremer. Long time atomistic polymer trajectories from coarse grained simulations: bisphenol-a polycarbonate. *Soft Matter*, 2:409–414, 2006. doi: 10.1039/B602076C. URL http://dx.doi.org/10.1039/B602076C.

[73] V. A. Harmandaris, N. P. Adhikari, N. F. A. van der Vegt, and K. Kremer. Hierarchical modeling of polystyrene: From atomistic to coarse-grained simulations.

Macromolecules, 39(19):6708–6719, 2014/05/06 2006. doi: 10.1021/ma0606399. URL http://dx.doi.org/10.1021/ma0606399.

[74] Qi Sun and Roland Faller. Systematic coarse-graining of a polymer blend: Polyisoprene and polystyrene. *Journal of Chemical Theory and Computation*, 2(3): 607–615, 2014/05/06 2006. doi: 10.1021/ct600065v. URL http://dx.doi.org/10.1021/ct600065v.

[75] Vagelis A. Harmandaris and Kurt Kremer. Predicting polymer dynamics at multiple length and time scales. *Soft Matter*, 5:3920–3926, 2009. doi: 10.1039/B905361A. URL http://dx.doi.org/10.1039/B905361A.

[76] Vagelis A. Harmandaris and Kurt Kremer. Dynamics of polystyrene melts through hierarchical multiscale simulations. *Macromolecules*, 42(3):791–802, 2014/05/07 2009. doi: 10.1021/ma8018624. URL http://dx.doi.org/10.1021/ma8018624.

[77] Christine Peter and Kurt Kremer. Multiscale simulation of soft matter systems. *Faraday Discussions*, 144:9–24, 2010. doi: 10.1039/B919800H. URL http://dx.doi.org/10.1039/B919800H.

[78] Olga Bezkorovaynaya, Alexander Lukyanov, Kurt Kremer, and Christine Peter. Multiscale simulation of small peptides: consistent conformational sampling in atomistic and coarse-grained models. *Journal of Computational Chemistry*, 33(9): 937–49, Apr 2012. doi: 10.1002/jcc.22915.

[79] Sudip Roy. Particle based multiscale simulation methods and applications. In *Chemical Modelling: Applications and Theory Volume 9*, volume 9, pages 92–134. The Royal Society of Chemistry, 2012. ISBN 978-1-84973-412-7. doi: 10.1039/9781849734790-00092. URL http://dx.doi.org/10.1039/9781849734790-00092.

[80] Souvik Chakraborty, Chandan Kumar Choudhury, and Sudip Roy. Morphology and dynamics of carbon nanotube in polycarbonate carbon nanotube composite from dissipative particle dynamics simulation. *Macromolecules*, 46(9):3631–3638, 2014/12/20 2013. doi: 10.1021/ma302425s. URL http://dx.doi.org/10.1021/ma302425s.

[81] Paola Carbone, Hossein Ali Karimi-Varzaneh, and Florian Muller-Plathe. Fine-graining without coarse-graining: an easy and fast way to equilibrate dense polymer melts. *Faraday Discussions*, 144:25–42, 2010. doi: 10.1039/B902363A. URL http://dx.doi.org/10.1039/B902363A.

[82] Nicodemo di Pasquale, Daniele Marchisio, and Paola Carbone. Mixing atoms and coarse-grained beads in modelling polymer melts. *The Journal of Chemical Physics*,

137(16):164111, 2012. doi: http://dx.doi.org/10.1063/1.4759504. URL http://scitation.aip.org/content/aip/journal/jcp/137/16/10.1063/1.4759504.

[83] Nicodemo Di Pasquale, Richard J. Gowers, and Paola Carbone. A multiple time step scheme for multiresolved models of macromolecules. *Journal of Computational Chemistry*, 35(16):1199–1207, 2014. ISSN 1096-987X. doi: 10.1002/jcc.23594. URL http://dx.doi.org/10.1002/jcc.23594.

[84] Dominik Fritz, Konstantin Koschke, Vagelis A. Harmandaris, Nico F. A. van der Vegt, and Kurt Kremer. Multiscale modeling of soft matter: scaling of dynamics. *Phys. Chem. Chem. Phys.*, 13:10412–10420, 2011. doi: 10.1039/C1CP20247B. URL http://dx.doi.org/10.1039/C1CP20247B.

[85] Cahit Dalgicdir, Ozge Sensoy, Christine Peter, and Mehmet Sayar. A transferable coarse-grained model for diphenylalanine: How to represent an environment driven conformational transition. *The Journal Chemical Physics*, 139(23):234115, 2013. doi: http://dx.doi.org/10.1063/1.4848675. URL http://scitation.aip.org/content/aip/journal/jcp/139/23/10.1063/1.4848675.

[86] Alessandra Villa, Nico F A van der Vegt, and Christine Peter. Self-assembling dipeptides: including solvent degrees of freedom in a coarse-grained model. *Physical Chemistry Chemical Physics*, 11(12):2068–2076, Mar 2009. ISSN 1463-9076 (Print); 1463-9076 (Linking). doi: 10.1039/b818146m.

[87] Giuseppe Milano and Florian Müller-Plathe. Mapping atomistic simulations to mesoscopic models: A systematic coarse-graining procedure for vinyl polymer chains. *The Journal of Physical Chemistry B*, 109(39):18609–18619, 2014/04/19 2005. doi: 10.1021/jp0523571. URL http://dx.doi.org/10.1021/jp0523571.

[88] Hossein Ali Karimi-Varzaneh, Florian Muller-Plathe, Sundaram Balasubramanian, and Paola Carbone. Studying long-time dynamics of imidazolium-based ionic liquids with a systematically coarse-grained model. *Physical Chemistry Chemical Physics*, 12:4714–4724, 2010. doi: 10.1039/B925780B. URL http://dx.doi.org/10.1039/B925780B.

[89] Biswaroop Mukherjee, Luigi Delle Site, Kurt Kremer, and Christine Peter. Derivation of coarse grained models for multiscale simulation of liquid crystalline phase transitions. *The Journal of Physical Chemistry B*, 116(29):8474–8484, 2014/12/22 2012. doi: 10.1021/jp212300d. URL http://dx.doi.org/10.1021/jp212300d.

[90] W. Tschöp, K. Kremer, J. Batoulis, T. Bürger, and O. Hahn. Simulation of polymer melts. i. coarse-graining procedure for polycarbonates. *Acta*

Polymerica, 49(2-3):61–74, 1998. ISSN 1521-4044. doi: 10.1002/(SICI)1521-4044(199802)49:2/3¡61::AID-APOL61¿3.0.CO;2-V. URL http://dx.doi.org/10.1002/(SICI)1521-4044(199802)49:2/3<61::AID-APOL61>3.0.CO;2-V.

[91] A. K. Soper. Empirical potential monte carlo simulation of fluid structure. *Chemical Physics*, 202(2–3):295–306, 1 1996. doi: http://dx.doi.org/10.1016/0301-0104(95)00357-6. URL http://www.sciencedirect.com/science/article/pii/0301010495003576.

[92] R.L. Henderson. A uniqueness theorem for fluid pair correlation functions. *Physics Letters A*, 49(3):197 – 198, 1974. ISSN 0375-9601. doi: http://dx.doi.org/10.1016/0375-9601(74)90847-0. URL http://www.sciencedirect.com/science/article/pii/0375960174908470.

[93] Beste Bayramoglu and Roland Faller. Coarse-grained modeling of polystyrene in various environments by iterative boltzmann inversion. *Macromolecules*, 45(22): 9205–9219, 2014/12/08 2012. doi: 10.1021/ma301280b. URL http://dx.doi.org/10.1021/ma301280b.

[94] Alexander P. Lyubartsev and Aatto Laaksonen. Calculation of effective interaction potentials from radial distribution functions: A reverse monte carlo approach. *Physical Review E*, 52:3730–3737, Oct 1995. doi: 10.1103/PhysRevE.52.3730. URL http://link.aps.org/doi/10.1103/PhysRevE.52.3730.

[95] Alexander Lyubartsev, Alexander Mirzoev, LiJun Chen, and Aatto Laaksonen. Systematic coarse-graining of molecular models by the newton inversion method. *Faraday Discussions*, 144:43–56, 2010. doi: 10.1039/B901511F. URL http://dx.doi.org/10.1039/B901511F.

[96] Sergei Izvekov and Gregory A. Voth. Multiscale coarse graining of liquid-state systems. *The Journal of Chemical Physics*, 123(13):134105, 2005. doi: http://dx.doi.org/10.1063/1.2038787. URL http://scitation.aip.org/content/aip/journal/jcp/123/13/10.1063/1.2038787.

[97] Sergei Izvekov and Gregory A. Voth. A multiscale coarse-graining method for biomolecular systems. *The Journal of Physical Chemistry B*, 109(7):2469–2473, 2014/12/22 2005. doi: 10.1021/jp044629q. URL http://dx.doi.org/10.1021/jp044629q.

[98] Subhadip Das, Vikesh Singh Baghel, Sudip Roy, and Rajnish Kumar. A molecular dynamics study of model si clathrate hydrates: the effect of guest size and guest-water interaction on decomposition kinetics. *Physical Chemistry Chemical Physics*,

17(14):9509–9518, 2015. doi: 10.1039/C5CP00678C. URL http://dx.doi.org/10.1039/C5CP00678C.

[99] Vikesh Singh Baghel, Rajnish Kumar, and Sudip Roy. Heat transfer calculations for decomposition of structure i methane hydrates by molecular dynamics simulation. *The Journal of Physical Chemistry C*, 117(23):12172–12182, 06 2013. doi: 10.1021/jp4023772. URL http://dx.doi.org/10.1021/jp4023772.

[100] Kamendra P. Sharma, Chandan Kumar Choudhury, Sonal Srivastava, H. Davis, P. R. Rajamohanan, Sudip Roy, and Guruswamy Kumaraswamy. Assembly of polyethyleneimine in the hexagonal mesophase of nonionic surfactant: Effect of ph and temperature. *J. Phys. Chem. B*, 115(29):9059, 06 2011. doi: 10.1021/jp202614x. URL http://pubs.acs.org/doi/abs/10.1021/jp202614x.

[101] Souvik Chakraborty and Sudip Roy. Structural, dynamical, and thermodynamical properties of carbon nanotube polycarbonate composites: A molecular dynamics study. *The Journal of Physical Chemistry B*, 116(10):3083–3091, 03 2012. doi: 10.1021/jp212220m. URL http://dx.doi.org/10.1021/jp212220m.

[102] Swagata Pahari, Chandan Kumar Choudhury, Prithvi Raj Pandey, Minal More, Arun Venkatnathan, and Sudip Roy. Molecular dynamics simulation of phosphoric acid doped monomer of polybenzimidazole: A potential component polymer electrolyte membrane of fuel cell. *The Journal of Physical Chemistry B*, 116(24): 7357–7366, 06 2012. doi: 10.1021/jp301117m. URL http://dx.doi.org/10.1021/jp301117m.

[103] Swagata Pahari and Sudip Roy. Evidence and characterization of dynamic heterogeneity in binary mixtures of phosphoric acid and benzimidazole. *The Journal of Chemical Physics*, 139(15):154701, 2013. doi: http://dx.doi.org/10.1063/1.4824767. URL http://scitation.aip.org/content/aip/journal/jcp/139/15/10.1063/1.4824767.

[104] Anil R. Mhashal and Sudip Roy. Effect of gold nanoparticle on structure and fluidity of lipid membrane. *PLoS ONE*, 9(12):e114152 EP –, 12 2014. URL http://dx.doi.org/10.1371%2Fjournal.pone.0114152.

[105] Prithvi Raj Pandey and Sudip Roy. Headgroup mediated water insertion into the dppc bilayer: A molecular dynamics study. *J. Phys. Chem. B*, 115(12):3155–3163, 2013/03/12 2011. doi: 10.1021/jp1090203. URL http://dx.doi.org/10.1021/jp1090203.

[106] Prithvi Raj Pandey and Sudip Roy. Early stages of unwinding of zwitterionic -helical homopolymeric peptides. *Chemical Physics Letters*, 514(4–6):330–335,

10 2011. doi: http://dx.doi.org/10.1016/j.cplett.2011.08.050. URL http://www.sciencedirect.com/science/article/pii/S0009261411010311.

[107] Prithvi Raj Pandey and Sudip Roy. Is it possible to change wettability of hydrophilic surface by changing its roughness? *The Journal of Physical Chemistry Letters*, 4 (21):3692–3697, 11 2013. doi: 10.1021/jz401946v. URL http://pubs.acs.org/doi/abs/10.1021/jz401946v.

[108] Prithvi Raj Pandey and Sudip Roy. Model atomistic protrusions favouring the ordering and retention of water. *Physical Chemistry Chemical Physics*, 16(30): 15856–15865, 2014.

[109] Sudip Roy, Dilyana Markova, Avneesh Kumar, Markus Klapper, and Florian Müller-Plathe. Morphology of phosphonic acid-functionalized block copolymers studied by dissipative particle dynamics. *Macromolecules*, 42(3):841–848, 02 2009. doi: 10.1021/ma802263t. URL http://dx.doi.org/10.1021/ma802263t.

[110] D. Frenkel and B. Smit. *Understanding Molecular Simulation: From Algorithms to Applications*. Academic Press. Academic Press, 2002. ISBN 9780122673511. URL https://books.google.de/books?id=XmyO2oRUg0cC.

[111] Loup Verlet. Computer "experiments" on classical fluids. i. thermodynamical properties of lennard-jones molecules. *Physical Review*, 159(1):98–103, 07 1967. URL http://link.aps.org/doi/10.1103/PhysRev.159.98.

[112] A.R. Leach. *Molecular Modelling: Principles and Applications*. Pearson Education. Prentice Hall, 2001. ISBN 9780582382107. URL https://books.google.co.in/books?id=kB7jsbV-uhkC.

[113] P. P. Ewald. Die berechnung optischer und elektrostatischer gitterpotentiale. *Annalen der Physik*, 369(3):253–287, 1921. doi: 10.1002/andp.19213690304. URL http://dx.doi.org/10.1002/andp.19213690304.

[114] Darrin York Tom Darden and Lee Pedersen. Particle mesh ewald: An nlog(n) method for ewald sums in large systems. *The Journal of Chemical Physics*, 98(12): 10089, 1993. doi: doi:10.1063/1.464397.

[115] Lars Onsager. Electric moments of molecules in liquids. *Journal of the American Chemical Society*, 58(8):1486–1493, 2014/05/10 1936. doi: 10.1021/ja01299a050. URL http://dx.doi.org/10.1021/ja01299a050.

[116] R. W Hockney, S. P Goel, and J. W Eastwood. Quiet high-resolution computer models of a plasma. *Journal of Computational Physics*, 14(2):148–158,

2 1974. doi: http://dx.doi.org/10.1016/0021-9991(74)90010-2. URL http://www.sciencedirect.com/science/article/pii/0021999174900102.

[117] William C. Swope, Hans C. Andersen, Peter H. Berens, and Kent R. Wilson. A computer simulation method for the calculation of equilibrium constants for the formation of physical clusters of molecules: Application to small water clusters. *The Journal of Chemical Physics*, 76(1):637–649, 1982. URL http://scitation.aip.org/content/aip/journal/jcp/76/1/10.1063/1.442716.

[118] D. Beeman. Some multistep methods for use in molecular dynamics calculations. *Journal of Computational Physics*, 20(2):130–139, 2 1976. doi: http://dx.doi.org/10.1016/0021-9991(76)90059-0. URL http://www.sciencedirect.com/science/article/pii/0021999176900590.

[119] Berk Hess. P-lincs: A parallel linear constraint solver for molecular simulation. *Journal of Chemical Theory and Computation*, 4(1):116–122, 2014/05/10 2007. doi: 10.1021/ct700200b. URL http://dx.doi.org/10.1021/ct700200b.

[120] Berk Hess, Henk Bekker, Herman J. C. Berendsen, and Johannes G. E. M. Fraaije. Lincs: A linear constraint solver for molecular simulations. *Journal of Computational Chemistry*, 18(12):1463–1472, 1997. ISSN 1096-987X. doi: 10.1002/(SICI)1096-987X(199709)18:12¡1463::AID-JCC4¿3.0.CO;2-H. URL http://dx.doi.org/10.1002/(SICI)1096-987X(199709)18:12<1463::AID-JCC4>3.0.CO;2-H.

[121] Jean-Paul Ryckaert, Giovanni Ciccotti, and Herman J. C Berendsen. Numerical integration of the cartesian equations of motion of a system with constraints: molecular dynamics of n-alkanes. *Journal of Computational Physics*, 23(3):327–341, 3 1977. doi: http://dx.doi.org/10.1016/0021-9991(77)90098-5. URL http://www.sciencedirect.com/science/article/pii/0021999177900985.

[122] H. J. C Berendsen, J. P. M Postma, W. F van Gunsteren, A DiNola, and J. R Haak. Molecular dynamics with coupling to an external bath. *The Journal of Chemical Physics*, 81(8):3684, 1984. doi: doi:10.1063/1.448118.

[123] Giovanni Bussi, Davide Donadio, and Michele Parrinello. Canonical sampling through velocity rescaling. *The Journal of Chemical Physics*, 126(1):014101, 2007. doi: doi:10.1063/1.2408420.

[124] Enrique de Miguel and George Jackson. The nature of the calculation of the pressure in molecular simulations of continuous models from volume perturbations. *The Journal of Chemical Physics*, 125(16):164109, 2006.

doi: http://dx.doi.org/10.1063/1.2363381. URL http://scitation.aip.org/content/aip/journal/jcp/125/16/10.1063/1.2363381.

[125] Hossein Ali Karimi-Varzaneh and Florian Müller-Plathe. Coarse-grained modeling for macromolecular chemistry. *Topics in Current Chemistry*, 307:295–321, 2012. doi: 10.1007/128˙2010˙122.

[126] Sergei Izvekov and Gregory A. Voth. Multiscale coarse graining of liquid-state systems. *The Journal of Chemical Physics*, 123(13):134105, 2005. doi: http://dx.doi.org/10.1063/1.2038787. URL http://scitation.aip.org/content/aip/journal/jcp/123/13/10.1063/1.2038787.

[127] W. G. Noid, Jhih-Wei Chu, Gary S. Ayton, and Gregory A. Voth. Multiscale coarse-graining and structural correlations: Connections to liquid-state theory. *The Journal of Physical Chemistry B*, 111(16):4116–4127, 2014/04/21 2007. doi: 10.1021/jp068549t. URL http://dx.doi.org/10.1021/jp068549t.

[128] VOTCA development team. *VOTCA User Manual version 1.2.3*. www.votca.org, August 2012.

[129] Gromacs. URL http://www.gromacs.org/.

[130] Berk Hess, Carsten Kutzner, David van der Spoel, and Erik Lindahl. Gromacs 4: Algorithms for highly efficient, load-balanced, and scalable molecular simulation. *Journal of Chemical Theory and Computation*, 4(3):435–447, 2008. doi: 10.1021/ct700301q. URL http://pubs.acs.org/doi/abs/10.1021/ct700301q.

[131] David Van Der Spoel, Erik Lindahl, Berk Hess, Gerrit Groenhof, Alan E. Mark, and Herman J. C. Berendsen. Gromacs: Fast, flexible, and free. *Journal of Computational Chemistry*, 26(16):1701, 2005. ISSN 1096-987X. doi: 10.1002/jcc.20291. URL http://dx.doi.org/10.1002/jcc.20291.

[132] Victor Rühle, Christoph Junghans, Alexander Lukyanov, Kurt Kremer, and Denis Andrienko. Versatile object-oriented toolkit for coarse-graining applications. *Journal of Chemical Theory and Computation*, 5(12):3211–3223, 2014/04/24 2009. doi: 10.1021/ct900369w. URL http://dx.doi.org/10.1021/ct900369w.

[133] D Jere, H L Jiang, R Arote, Y K Kim, Y J Choi, M H Cho, T Akaike, and C S Cho. Degradable polyethylenimines as dna and small interfering rna carriers. *Expert Opinion Drug Delivery*, 6(8):827–834, Aug 2009. ISSN 1744-7593 (Electronic); 1742-5247 (Linking). doi: 10.1517/17425240903029183.

[134] Guillaume Herlem and Boris Lakard. Ab initio study of the electronic and structural properties of the crystalline polyethyleneimine polymer. *The Journal of Chemical Physics*, 120:9376, 2004. doi: 10.1063/1.1701815.

[135] Jesse D. Ziebarth and Yongmei Wang. Understanding the protonation behavior of linear polyethylenimine in solutions through monte carlo simulations. *Biomacromolecules*, 11(1):29, 2010. doi: 10.1021/bm900842d. URL `http://pubs.acs.org/doi/abs/10.1021/bm900842d`. PMID: 19954222.

[136] Allison J. DePaul, Erik J. Thompson, Sarav S. Patel, Kristin Haldeman, and Eric J. Sorin. Equilibrium conformational dynamics in an rna tetraloop from massively parallel molecular dynamics. *Nucleic Acids Res.*, 38(14):4856, 2010. doi: 10.1093/nar/gkq134. URL `http://nar.oxfordjournals.org/content/38/14/4856.abstract`.

[137] Eric J. Sorin and Vijay S. Pande. Exploring the helix-coil transition via all-atom equilibrium ensemble simulations. *Biophysical Journal*, 88(4):2472, 2005. ISSN 0006-3495. doi: DOI: 10.1529/biophysj.104.051938. URL `http://www.sciencedirect.com/science/article/pii/S000634950573304X`.

[138] Michael W. Mahoney and William L. Jorgensen. A five-site model for liquid water and the reproduction of the density anomaly by rigid, nonpolarizable potential functions. *The Journal of Chemical Physics*, 112:8910, 2000. doi: 10.1063/1.481505. URL `http://dx.doi.org/10.1063/1.481505`.

[139] Junmei Wang, Piotr Cieplak, and Peter A. Kollman. How well does a restrained electrostatic potential (resp) model perform in calculating conformational energies of organic and biological molecules? *Journal of Computational Chemistry*, 21(12):1049, 2000. ISSN 1096-987X. doi: 10.1002/1096-987X(200009)21:12¡1049::AID-JCC3¿3.0.CO;2-F. URL `http://dx.doi.org/10.1002/1096-987X(200009)21:12<1049::AID-JCC3>3.0.CO;2-F`.

[140] Accelrys software inc, materials studio release notes, release 6.0, san diego: Accelrys software inc., 2011.

[141] Yozo Chatani, Takushi Kobatake, Hiroyuki Tadokoro, and Ryuichi Tanaka. Structural studies of poly(ethylenimine). 2. double-stranded helical chains in the anhydrate. *Macromolecules*, 15(1):170, 1982. doi: 10.1021/ma00229a034. URL `http://pubs.acs.org/doi/abs/10.1021/ma00229a034`.

[142] R. W. Impey, P. A. Madden, and I. R. McDonald. Hydration and mobility of ions in solution. *J. Phys. Chem.*, 87(25):5071, 1983. doi: 10.1021/j150643a008. URL `http://pubs.acs.org/doi/abs/10.1021/j150643a008`.

[143] S. Woutersen, U. Emmerichs, and H. J. Bakker. Femtosecond mid-ir pump-probe spectroscopy of liquid water: Evidence for a two-component structure.

Science, 278(5338):658, 1997. doi: 10.1126/science.278.5338.658. URL http://www.sciencemag.org/content/278/5338/658.abstract.

[144] Amerigo Beneduci. Which is the effective time scale of the fast debye relaxation process in water? *J. Mol. Liq.*, 138(1–3):55, 2008. ISSN 0167-7322. doi: 10.1016/j.molliq.2007.07.003. URL http://www.sciencedirect.com/science/article/pii/S0167732207001316.

[145] Vladimir I. Gaiduk and Derrick S. F. Crothers. Basic molecular mechanisms underlying complex permittivity of water and ice. *J. Phys. Chem. A*, 110(30):9361, 2006. doi: 10.1021/jp0680138. URL http://pubs.acs.org/doi/abs/10.1021/jp0680138. PMID: 16869684.

[146] Noam Agmon. Tetrahedral displacement: the molecular mechanism behind the debye relaxation in water. *J. Phys. Chem.*, 100(3):1072, 1996. doi: 10.1021/jp9516295. URL http://pubs.acs.org/doi/abs/10.1021/jp9516295.

[147] Alberto Striolo. The mechanism of water diffusion in narrow carbon nanotubes. *Nano Lett.*, 6(4):633, 2006. doi: 10.1021/nl052254u. URL http://pubs.acs.org/doi/abs/10.1021/nl052254u.

[148] J. H Wang. Self-diffusion and structure of liquid water. i. measurement of self-diffusion of liquid water with deuterium as tracer. *Journal of the American Chemical Society*, 73(2):510, 1951. doi: 10.1021/ja01146a002. URL http://pubs.acs.org/doi/abs/10.1021/ja01146a002.

[149] Jui Hsin Wang, Charles V. Robinson, and I. S. Edelman. Self-diffusion and structure of liquid water. iii. measurement of the self-diffusion of liquid water with h2, h3 and o18 as tracers1. *Journal of the American Chemical Society*, 75(2):466, 2012/09/10 1953. doi: 10.1021/ja01098a061. URL http://dx.doi.org/10.1021/ja01098a061.

[150] Muralidharan S. Sulatha and Upendra Natarajan. Origin of the difference in structural behavior of poly(acrylic acid) and poly(methacrylic acid) in aqueous solution discerned by explicit-solvent explicit-ion md simulations. *Industrial and Engineering Chemistry Research*, 50(21):11785, 2012/09/18 2011. doi: 10.1021/ie2014845. URL http://dx.doi.org/10.1021/ie2014845.

[151] Chunli Li, Jiawei Shen, Christine Peter, and Nico F. A. van der Vegt. A chemically accurate implicit-solvent coarse-grained model for polystyrenesulfonate solutions. *Macromolecules*, 45(5):2551, 2012. doi: 10.1021/ma202490h. URL http://pubs.acs.org/doi/abs/10.1021/ma202490h.

[152] Dirk Reith, Beate Muller, Florian Müller-Plathe, and Simone Wiegand. How does the chain extension of poly (acrylic acid) scale in aqueous solution? a combined study with light scattering and computer simulation. *The Journal of Chemical Physics*, 116(20):9100, 2002. doi: 10.1063/1.1471901. URL `http://link.aip.org/link/?JCP/116/9100/1`.

[153] J P Behr. The proton sponge: a trick to enter cells the viruses did not exploit. *Chimia*, 51(1-2):34, 1997. URL `http://www.ingentaconnect.com/content/scs/chimia/1997/00000051/F0020001/art00026`.

[154] Ilya Koltover, Tim Salditt, Joachim O. Rädler, and Cyrus R. Safinya. An inverted hexagonal phase of cationic liposome-dna complexes related to dna release and delivery. *Science*, 281(5373):78–81, 07 1998. URL `http://www.sciencemag.org/content/281/5373/78.abstract`.

[155] Joachim O. Rädler, Ilya Koltover, Tim Salditt, and Cyrus R. Safinya. Structure of dna-cationic liposome complexes: Dna intercalation in multilamellar membranes in distinct interhelical packing regimes. *Science*, 275(5301):810–814, 02 1997. URL `http://www.sciencemag.org/content/275/5301/810.abstract`.

[156] Job Ubbink, Adam Burbidge, and Raffaele Mezzenga. Food structure and functionality: a soft matter perspective. *Soft Matter*, 4(8):1569–1581, 2008. doi: 10.1039/B802183J. URL `http://dx.doi.org/10.1039/B802183J`.

[157] Raffaele Mezzenga, Peter Schurtenberger, Adam Burbidge, and Martin Michel. Understanding foods as soft materials. *Nat Mater*, 4(10):729–740, 10 2005. URL `http://dx.doi.org/10.1038/nmat1496`.

[158] In-Kyu Park, Kaushik Singha, Rohidas B. Arote, Yun-Jaie Choi, Won Jong Kim, and Chong-Su Cho. ph-responsive polymers as gene carriers. *Macromolecular Rapid Communications*, 31(13):1122–1133, 2010. doi: 10.1002/marc.200900867. URL `http://dx.doi.org/10.1002/marc.200900867`.

[159] Vijay A. Sethuraman, Kun Na, and You Han Bae. ph-responsive sulfonamide/pei system for tumor specific gene delivery: An in vitro study. *Biomacromolecules*, 7 (1):64–70, 01 2006. doi: 10.1021/bm0503571. URL `http://dx.doi.org/10.1021/bm0503571`.

[160] Stephanie Werth, Beata Urban-Klein, Lige Dai, Sabrina Höbel, Marius Grzelinski, Udo Bakowsky, Frank Czubayko, and Achim Aigner. A low molecular weight fraction of polyethylenimine (pei) displays increased transfection efficiency of dna and sirna in fresh or lyophilized complexes. *Journal of Controlled Release*, 112

(2):257–270, 5 2006. doi: http://dx.doi.org/10.1016/j.jconrel.2006.02.009. URL http://www.sciencedirect.com/science/article/pii/S0168365906000794.

[161] Beverley R. Twaites, Carolina de las Heras Alarcón, David Cunliffe, Matthieu Lavigne, Sivanand Pennadam, James R. Smith, Dariusz C. Górecki, and Cameron Alexander. Thermo and ph responsive polymers as gene delivery vectors: effect of polymer architecture on dna complexation in vitro. *Journal of Controlled Release*, 97(3):551–566, 7 2004. doi: http://dx.doi.org/10.1016/j.jconrel.2004.03.032. URL http://www.sciencedirect.com/science/article/pii/S0168365904001543.

[162] M. J. Frisch, G. W. Trucks, H. B. Schlegel, G. E. Scuseria, M. A. Robb, J. R. Cheeseman, G. Scalmani, V. Barone, B. Mennucci, G. A. Petersson, H. Nakatsuji, M. Caricato, X. Li, H. P. Hratchian, A. F. Izmaylov, J. Bloino, G. Zheng, J. L. Sonnenberg, M. Hada, M. Ehara, K. Toyota, R. Fukuda, J. Hasegawa, M. Ishida, T. Nakajima, Y. Honda, O. Kitao, H. Nakai, T. Vreven, J. A. Montgomery, Jr., J. E. Peralta, F. Ogliaro, M. Bearpark, J. J. Heyd, E. Brothers, K. N. Kudin, V. N. Staroverov, R. Kobayashi, J. Normand, K. Raghavachari, A. Rendell, J. C. Burant, S. S. Iyengar, J. Tomasi, M. Cossi, N. Rega, J. M. Millam, M. Klene, J. E. Knox, J. B. Cross, V. Bakken, C. Adamo, J. Jaramillo, R. Gomperts, R. E. Stratmann, O. Yazyev, A. J. Austin, R. Cammi, C. Pomelli, J. W. Ochterski, R. L. Martin, K. Morokuma, V. G. Zakrzewski, G. A. Voth, P. Salvador, J. J. Dannenberg, S. Dapprich, A. D. Daniels, Ö. Farkas, J. B. Foresman, J. V. Ortiz, J. Cioslowski, and D. J. Fox. Gaussian 09 Revision A.1. Gaussian Inc. Wallingford CT 2009.

[163] Curt M. Breneman and Kenneth B. Wiberg. Determining atom-centered monopoles from molecular electrostatic potentials. the need for high sampling density in formamide conformational analysis. *Journal of Computational Chemistry*, 11(3): 361–373, 1990. doi: 10.1002/jcc.540110311. URL http://dx.doi.org/10.1002/jcc.540110311.

[164] The PyMOL molecular graphics system, version 1.5.0.4 Schrödinger, LLC New York, 2010., August .

[165] Lucia Ya. Zakharova, Alsu R. Ibragimova, Farida G. Valeeva, Andrey V. Zakharov, Asiya R. Mustafina, Lyudmila A. Kudryavtseva, Harlampy E. Harlampidi, and Alexander I. Konovalov. Nanosized reactors based on polyethyleneimines: From microheterogeneous systems to immobilized catalysts. *Langmuir*, 23(6):3214–3224, 03 2007. doi: 10.1021/la0629633. URL http://dx.doi.org/10.1021/la0629633.

[166] Jordy Luten, Cornelus F. van Nostrum, Stefaan C. De Smedt, and Wim E. Hennink. Biodegradable polymers as non-viral carriers for plasmid dna delivery. *Journal of Controlled Release*, 126(2):97 – 110, 2008. ISSN 0168-3659. doi:

10.1016/j.jconrel.2007.10.028. URL http://www.sciencedirect.com/science/article/pii/S0168365907006220.

[167] Ladan Parhamifar, Anna K. Larsen, A. Christy Hunter, Thomas L. Andresen, and S. Moein Moghimi. Polycation cytotoxicity: a delicate matter for nucleic acid therapy-focus on polyethylenimine. *Soft Matter*, 6(17):4001–4009, 2010. doi: 10.1039/C000190B. URL http://dx.doi.org/10.1039/C000190B.

[168] Tarik Eren, Abhigyan Som, Jason R. Rennie, Christopher F. Nelson, Yelena Urgina, Klaus Nüsslein, E. Bryan Coughlin, and Gregory N. Tew. Antibacterial and hemolytic activities of quaternary pyridinium functionalized polynorbornenes. *Macromol. Chem. Phys.*, 209(5):516–524, 2008. ISSN 1521-3935. doi: 10.1002/macp.200700418. URL http://dx.doi.org/10.1002/macp.200700418.

[169] Liping Ding, Eva Y. Chi, Kirk S. Schanze, Gabriel P. Lopez, and David G. Whitten. Insight into the mechanism of antimicrobial conjugated polyelectrolytes: Lipid headgroup charge and membrane fluidity effects. *Langmuir*, 26(8):5544–5550, 2010. doi: 10.1021/la9038045. URL http://pubs.acs.org/doi/abs/10.1021/la9038045. PMID: 20000327.

[170] Liping Ding, Eva Y. Chi, Sireesha Chemburu, Eunkyung Ji, Kirk S. Schanze, Gabriel P. Lopez, and David G. Whitten. Insight into the mechanism of antimicrobial poly(phenylene ethynylene) polyelectrolytes: Interactions with phosphatidylglycerol lipid membranes langmuir 25th year: Molecular and macromolecular self-assemblies. *Langmuir*, 25(24):13742–13751, 2009. doi: 10.1021/la901457t. URL http://pubs.acs.org/doi/abs/10.1021/la901457t. PMID: 20560549.

[171] Jean Paul Behr. Synthetic gene-transfer vectors. *Accounts of Chemical Research*, 26(5):274–278, 1993. doi: 10.1021/ar00029a008. URL http://pubs.acs.org/doi/abs/10.1021/ar00029a008.

[172] Idit Kopatz, Jean-Serge Remy, and Jean-Paul Behr. A model for non-viral gene delivery: through syndecan adhesion molecules and powered by actin. *J. Gene. Med.*, 6(7):769–776, 2004. ISSN 1521-2254. doi: 10.1002/jgm.558. URL http://dx.doi.org/10.1002/jgm.558.

[173] Zhuojun Dai, Torben Gjetting, Maria A. Mattebjerg, Chi Wu, and Thomas L. Andresen. Elucidating the interplay between dna-condensing and free polycations in gene transfection through a mechanistic study of linear and branched pei. *Biomaterials*, 32(33):8626–8634, 11 2011. doi: http://dx.doi.org/10.1016/j.biomaterials.2011.07.044. URL http://www.sciencedirect.com/science/article/pii/S0142961211008271.

[174] Sabine Boeckle, Katharina von Gersdorff, Silke van der Piepen, Carsten Culmsee, Ernst Wagner, and Manfred Ogris. Purification of polyethylenimine polyplexes highlights the role of free polycations in gene transfer. *J. Gene. Med.*, 6(10):1102–1111, 2004. doi: 10.1002/jgm.598. URL `http://dx.doi.org/10.1002/jgm.598`.

[175] You-Yeon Won, Rahul Sharma, and Stephen F. Konieczny. Missing pieces in understanding the intracellular trafficking of polycation/dna complexes. *Journal of Controlled Release*, 139(2):88–93, 10 2009. doi: http://dx.doi.org/10.1016/j.jconrel.2009.06.031. URL `http://www.sciencedirect.com/science/article/pii/S0168365909004714`.

[176] Rikke V\ Benjaminsen, Maria A\ Mattebjerg, Jonas R\ Henriksen, S Moein\ Moghimi, and Thomas L\ Andresen. The possible " proton sponge" effect of polyethylenimine (pei) does not include change in lysosomal ph. *Mol. Ther.*, 21(1): 149–157, 01 2013. URL `http://dx.doi.org/10.1038/mt.2012.185`.

[177] S. W. I. Siu, R. Vácha, P. Jungwirth, and R. A. Böckmann. Biomolecular simulations of membranes: Physical properties from different force fields. *The Journal of Chemical Physics*, 128:125103, 2008.

[178] Andrey Filippov, Greger Orädd, and Göran Lindblom. Influence of cholesterol and water content on phospholipid lateral diffusion in bilayers. *Langmuir*, 19(16): 6397–6400, 2003. doi: 10.1021/la034222x. URL `http://pubs.acs.org/doi/abs/10.1021/la034222x`.

[179] Chandan Kumar Choudhury and Sudip Roy. Structural and dynamical properties of polyethylenimine in explicit water at different protonation states: A molecular dynamics study. *Soft Matter*, 9(7):2269–2281, 2013. URL `http://dx.doi.org/10.1039/C2SM26290H`.

[180] J.C. Mathai, S. Tristram-Nagle, J.F. Nagle, and M.L. Zeidel. Structural determinants of water permeability through the lipid membrane. *J. Gen. Physiol.*, 131(1): 69–76, 2008. doi: doi: 10.1085/jgp.200709848.

[181] Guillem Portella and Bert L. de Groot. Determinants of water permeability through nanoscopic hydrophilic channels. *Biophysical Journal*, 96(3):925–938, 2 2009. doi: http://dx.doi.org/10.1016/j.bpj.2008.09.059. URL `http://www.sciencedirect.com/science/article/pii/S0006349508004438`.

[182] Rolf Auhl, Ralf Everaers, Gary S. Grest, Kurt Kremer, and Steven J. Plimpton. Equilibration of long chain polymer melts in computer simulations. *The Journal of Chemical Physics*, 119(24):12718–12728, 2003. URL `http://scitation.aip.org/content/aip/journal/jcp/119/24/10.1063/1.1628670`.

[183] Sergei Izvekov and Gregory A Voth. Multiscale coarse graining of liquid-state systems. *The Journal of Chemical Physics*, 123(13):134105, Oct 2005. doi: 10.1063/1.2038787.

[184] Cameron F. Abrams and Kurt Kremer. Combined coarse-grained and atomistic simulation of liquid bisphenol apolycarbonate: Liquid packing and intramolecular structure. *Macromolecules*, 36(1):260–267, 2014/04/20 2003. doi: 10.1021/ma0213495. URL http://dx.doi.org/10.1021/ma0213495.

[185] Roland Faller, Heiko Schmitz, Oliver Biermann, and Florian Müller-Plathe. Automatic parameterization of force fields for liquids by simplex optimization. *Journal of Computational Chemistry*, 20(10):1009–1017, 1999. ISSN 1096-987X. doi: 10.1002/(SICI)1096-987X(19990730)20:10¡1009::AID-JCC3¿3.0.CO;2-C. URL http://dx.doi.org/10.1002/(SICI)1096-987X(19990730)20:10<1009::AID-JCC3>3.0.CO;2-C.

[186] Hendrik Meyer, Oliver Biermann, Roland Faller, Dirk Reith, and Florian Mller-Plathe. Coarse graining of nonbonded inter-particle potentials using automatic simplex optimization to fit structural properties. *The Journal of Chemical Physics*, 113(15):6264, 2000. doi: http://dx.doi.org/10.1063/1.1308542. URL http://scitation.aip.org/content/aip/journal/jcp/113/15/10.1063/1.1308542.

[187] Roland Faller and Dirk Reith. Properties of poly(isoprene): Model building in the melt and in solution. *Macromolecules*, 36(14):5406–5414, 2014/05/06 2003. doi: 10.1021/ma025877s. URL http://dx.doi.org/10.1021/ma025877s.

[188] S. León, N. van der Vegt, L. Delle Site, and K. Kremer. Bisphenol a polycarbonate: Entanglement analysis from coarse-grained md simulations. *Macromolecules*, 38 (19):8078–8092, 2014/05/06 2005. doi: 10.1021/ma050943m. URL http://dx.doi.org/10.1021/ma050943m.

[189] Séverine Queyroy, Sylvie Neyertz, David Brown, and Florian Müller-Plathe. Preparing relaxed systems of amorphous polymers by multiscale simulation: Application to cellulose. *Macromolecules*, 37(19):7338–7350, 2014/03/03 2004. doi: 10.1021/ma035821d. URL http://dx.doi.org/10.1021/ma035821d.

[190] Giuseppe Santangelo, Andrea Di Matteo, Florian Müller-Plathe, and Giuseppe Milano. From mesoscale back to atomistic models: A fast reverse-mapping procedure for vinyl polymer chains. *The Journal of Physical Chemistry B*, 111(11):2765–2773, 2014/05/07 2007. doi: 10.1021/jp066212l. URL http://dx.doi.org/10.1021/jp066212l.

[191] Giuseppe Milano, Sylvain Goudeau, and Florian Müller-Plathe. Multicentered gaussian-based potentials for coarse-grained polymer simulations: Linking atomistic and mesoscopic scales. *Journal of Polymer Science Part B: Polymer Physics*, 43 (8):871–885, 2005. doi: 10.1002/polb.20380. URL `http://dx.doi.org/10.1002/polb.20380`.

[192] Qi Sun and Roland Faller. Systematic coarse-graining of atomistic models for simulation of polymeric systems. *Computers & Chemical Engineering*, 29(11–12):2380–2385, 10 2005. doi: http://dx.doi.org/10.1016/j.compchemeng.2005.05.026. URL `http://www.sciencedirect.com/science/article/pii/S0098135405001638`.

[193] Qi Sun and Roland Faller. Crossover from unentangled to entangled dynamics in a systematically coarse-grained polystyrene melt. *Macromolecules*, 39(2):812–820, 2014/05/06 2006. doi: 10.1021/ma0514774. URL `http://dx.doi.org/10.1021/ma0514774`.

[194] Vagelis A. Harmandaris, Dirk Reith, Nico F. A. van der Vegt, and Kurt Kremer. Comparison between coarse-graining models for polymer systems: Two mapping schemes for polystyrene. *Macromolecular Chemistry and Physics*, 208(19-20):2109–2120, 2007. doi: 10.1002/macp.200700245. URL `http://dx.doi.org/10.1002/macp.200700245`.

[195] Hu-Jun Qian, Paola Carbone, Xiaoyu Chen, Hossein Ali Karimi-Varzaneh, Chee Chin Liew, and Florian Müller-Plathe. Temperature-transferable coarse-grained potentials for ethylbenzene, polystyrene, and their mixtures. *Macromolecules*, 41(24):9919–9929, 2014/03/03 2008. doi: 10.1021/ma801910r. URL `http://dx.doi.org/10.1021/ma801910r`.

[196] Paola Carbone, Hossein Ali Karimi Varzaneh, Xiaoyu Chen, and Florian Müller-Plathe. Transferability of coarse-grained force fields: the polymer case. *The Journal of Chemical Physics*, 128(6):064904, Feb 2008. doi: 10.1063/1.2829409.

[197] Hossein Ali Karimi-Varzaneh, Nico F. A. van der Vegt, Florian Müller-Plathe, and Paola Carbone. How good are coarse-grained polymer models? a comparison for atactic polystyrene. *ChemPhysChem*, 13(15):3428–3439, 2012. doi: 10.1002/cphc.201200111. URL `http://dx.doi.org/10.1002/cphc.201200111`.

[198] Anupriya Agrawal, Dipak Aryal, Dvora Perahia, Ting Ge, and Gary S. Grest. Coarse-graining atactic polystyrene and its analogues. *Macromolecules*, 2014/05/07 2014. doi: 10.1021/ma500319v. URL `http://dx.doi.org/10.1021/ma500319v`.

[199] Henry S Ashbaugh, Harshit A Patel, Sanat K Kumar, and Shekhar Garde. Mesoscale model of polymer melt structure: self-consistent mapping of molecular correlations

to coarse-grained potentials. *The Journal of Chemical Physics*, 122(10):104908, Mar 2005. doi: 10.1063/1.1861455.

[200] Hossein Ali Karimi-Varzaneh, Paola Carbone, and Florian Müller-Plathe. Fast dynamics in coarse-grained polymer models: the effect of the hydrogen bonds. *The Journal of Chemical Physics*, 129(15):154904, Oct 2008. doi: 10.1063/1.2993111.

[201] Hossein Eslami, Hossein Ali Karimi-Varzaneh, and Florian Müller-Plathe. Coarse-grained computer simulation of nanoconfined polyamide-6,6. *Macromolecules*, 44 (8):3117–3128, 2014/04/21 2011. doi: 10.1021/ma102320v. URL `http://dx.doi.org/10.1021/ma102320v`.

[202] Biswaroop Mukherjee, Luigi Delle Site, Kurt Kremer, and Christine Peter. Derivation of coarse grained models for multiscale simulation of liquid crystalline phase transitions. *The Journal of Physical Chemistry B*, 116(29):8474–8484, 2014/05/07 2012. doi: 10.1021/jp212300d. URL `http://dx.doi.org/10.1021/jp212300d`.

[203] K R Hadley and C McCabe. A simulation study of the self-assembly of coarse-grained skin lipids. *Soft Matter*, 8(17):4802–4814, May 2012. doi: 10.1039/C2SM07204A.

[204] Yong-Lei Wang, Alexander Lyubartsev, Zhong-Yuan Lu, and Aatto Laaksonen. Multiscale coarse-grained simulations of ionic liquids: comparison of three approaches to derive effective potentials. *Physical Chemistry Chemical Physics*, 15 (20):7701–12, May 2013. doi: 10.1039/c3cp44108c.

[205] Xuejin Li, Dazhi Kou, Shuling Rao, and Haojun Liang. Developing a coarse-grained force field for the diblock copolymer poly(styrene-b-butadiene) from atomistic simulation. *The Journal of Chemical Physics*, 124(20):204909, 2006. doi: http://dx.doi.org/10.1063/1.2200694. URL `http://scitation.aip.org/content/aip/journal/jcp/124/20/10.1063/1.2200694`.

[206] Souvik Chakraborty and Sudip Roy. Structural, dynamical, and thermodynamical properties of carbon nanotube polycarbonate composites: A molecular dynamics study. *The Journal of Physical Chemistry B*, 116(10):3083–3091, 2014/04/24 2012. doi: 10.1021/jp212220m. URL `http://dx.doi.org/10.1021/jp212220m`.

[207] Kurt Kremer and Gary S. Grest. Dynamics of entangled linear polymer melts: a moleculardynamics simulation. *The Journal of Chemical Physics*, 92(8):5057–5086, 1990. doi: http://dx.doi.org/10.1063/1.458541.

[208] JamesE. Mark, L. J. Fetters, D. J. Lohse, and R. H. Colby. *Chain Dimensions and Entanglement Spacings*, pages 447–454. Springer New York, 2007. ISBN 978-0-387-31235-4. URL `http://dx.doi.org/10.1007/978-0-387-69002-5_25`.

[209] L. J. Fetters, D. J. Lohse, D. Richter, T. A. Witten, and A. Zirkel. Connection between polymer molecular weight, density, chain dimensions, and melt viscoelastic properties. *Macromolecules*, 27(17):4639–4647, 2014/11/26 1994. doi: 10.1021/ma00095a001. URL http://dx.doi.org/10.1021/ma00095a001.

[210] Graham Williams and David C. Watts. Non-symmetrical dielectric relaxation behaviour arising from a simple empirical decay function. *Transactions of the Faraday Society*, 66(0):80–85, 1970. doi: 10.1039/TF9706600080. URL http://dx.doi.org/10.1039/TF9706600080.

[211] Anastassia N. Rissanou and Vagelis Harmandaris. Dynamics of various polymer-graphene interfacial systems through atomistic molecular dynamics simulations. *Soft Matter*, 10(16):2876–2888, 2014. doi: 10.1039/C3SM52688G. URL http://dx.doi.org/10.1039/C3SM52688G.

Publications

a) Assembly of Polyethyleneimine in the hexagonal mesophase of nonionic surfactant: Effect of pH and temperature, K. P. Sharma, **C. K. Choudhury**, S. Srivastava, H. Davis, P. R. Rajamohanan, S. Roy, and G. Kumaraswamy*, J. Phys. Chem. B, 115 (29), 9059 - 9069 (2011).

b) Molecular dynamics simulation of Phosphoric acid doped monomer of Polybenzimidazole: a potential component polymer electrolyte membrane of fuel cell, S. Pahari, **C. K. Choudhury**, P. R. Pandey, M. More, A. Venkatnathan, and S. Roy*, J. Phys. Chem. B, 116 (24), 7357 - 7366 (2012).

c) Morphology and dynamics of carbon nanotube in polycarbonate carbon nanotube composite from dissipative particle dynamics simulation, S. Chakraborty, **C. K. Choudhury**, and S. Roy*, Macromolecules, 46 (9), 3631 - 3638 (2013).

d) Structural and dynamical properties of Polyethylenimine in explicit water at different protonation states: a molecular dynamics Study, **C. K. Choudhury**, and S. Roy*, Soft Matter, 9 (7), 2269 - 2281 (2013).

e) Characterization of conformation and interaction of gene delivery vector Polyethylenimine with phospholipid bilayer at different protonation state, **C. K. Choudhury***, A. Kumar, and S. Roy, Biomacromolecules, 14 (10), 3759 - 3768 (2013).

f) Compact polar moieties induce lipid-water systems to form discontinuous reverse micellar phase, M. Kumar, N. G. Patil, **C. K. Choudhury**, S. Roy, A. V. Ambade, and G. Kumaraswamy*, Soft Matter, (2015) (Accepted Manuscript, DOI: 10.1039/C5SM00854A).